LEVEL

THE UNIVERSITY OF KANSAS CENTER FOR RESEARCH, INC.

2291 Irving Hill Drive—Campus West
Lawrence, Kansas 66045

79 11 05 167

BACKSCATTER MEASUREMENTS
OF SEA ICE WITH A
HELICOPTER-BORNE
SCATTEROMETER

J.S. Patel
R.G. Onstott
C.V. Delker

R.K. Moore, Principal Investigator

Remote Sensing Laboratory
Center for Research, Inc.
The University of Kansas
Lawrence, Kansas 66045

RSL Technical Report
RSL TR 331-13

July 1979

Supported by:

REPORT DOCUMENTATION PAGE		READ INSTRUCTIONS BEFORE COMPLETING FORM
1. REPORT NUMBER	2. GOVT ACCESSION NO.	3. RECIPIENT'S CATALOG NUMBER
4. TITLE (and Subtitle) Backscatter Measurements of Sea Ice with a Helicopter-Borne Scatterometer		5. TYPE OF REPORT & PERIOD COVERED
		6. PERFORMING ORG. REPORT NUMBER RSL-TR-331-13
7. AUTHOR(s) J.S. Patel, R.G. Onstott, C.V. Delker, R.K. Moore		8. CONTRACT OR GRANT NUMBER(s) N00014-76-C-1105
9. PERFORMING ORGANIZATION NAME AND ADDRESS Remote Sensing Laboratory The Center for Research, Inc. The University of Kansas, Lawrence, Ks. 66045		10. PROGRAM ELEMENT, PROJECT, TASK AREA & WORK UNIT NUMBERS
11. CONTROLLING OFFICE NAME AND ADDRESS Office of Naval Research Arlington, Va. 22217		12. REPORT DATE Jul 1979 13. NUMBER OF PAGES 129
14. MONITORING AGENCY NAME & ADDRESS(if different from Controlling Office) Technical rept.		15. SECURITY CLASS. (of this report)
		15a. DECLASSIFICATION/DOWNGRADING SCHEDULE
16. DISTRIBUTION STATEMENT (of this Report) for public release and sale; its distribution is unlimited.		
17. DISTRIBUTION STATEMENT (of the abstract entered in Block 20, if different from Report)		
18. SUPPLEMENTARY NOTES		
19. KEY WORDS (Continue on reverse side if necessary and identify by block number)		

20. ABSTRACT (Continue on reverse side if necessary and identify by block number)

The purpose of this paper is to describe the design and development of the University of Kansas helicopter-borne scatterometer system, HELOSCAT. The experiments performed to measure the radar backscatter from sea ice with this system along with the results are also described.

In April and May of 1978 radar backscatter measurements were made with the University of Kansas helicopter-borne scatterometer, HELOSCAT. A Bell Model 205 helicopter, used for this experiment, was based at the Naval Arctic

DD FORM 1473 1 JAN 73   EDITION OF 1 NOV 65 IS OBSOLETE
 S/N 0102-014-6601

Research Laboratories, Pt. Barrow, Alaska. Backscatter measurements were made at 1-2 GHz and 8-18 GHz frequencies, HH-polarization, and three incidence angles (20°, 40° and 60°). Different types of ice ranging from thin ice to multiyear ice were observed; however, most data were collected from thick first-year and multiyear ice. A comparison of 1-2 GHz results for thick first-year and multiyear ice shows that the σ^0 values for multiyear ice at 60° are slightly lower than the value for thick first-year ice. The 8-18 GHz results show that the backscatter from multiyear ice at these frequencies is higher than the backscatter return from thick first-year ice by at least 3-4 dB. The frequency response of backscatter return is an upward sloping straight line on a dB-vs-frequency plot. For the multiyear ice, only the 60° data was found usable; the data at 20° and 40° were determined to be erroneous because of a malfunctioning frequency counter.

In March 1979 another HELOSCAT experiment was performed as a part of the Canadian SURSAT (Surveillance Satellite) program. Backscatter measurements were made at 8-18 GHz frequencies and HH-polarization. A preliminary analysis of the thick first-year sites observed during this experiment has been done. The scattering coefficient (σ^0) versus incidence angle (θ) curves for these sites follow a downward sloping trend as expected. This result further confirms the suspicion that the anomalous results obtained for part of the spring 1978 experiment data were indeed due to the malfunctioning frequency counter. The σ^0 values obtained from this experiment are generally 3-4 dB lower than the σ^0 values obtained for thick first-year ice from earlier experiments (spring 1977, 1978). The reason for this can be explained by the fact that the temperatures during this experiment were at least 25° C lower than the temperatures during the earlier experiments.

Accession For		
NTIS GRA&I		☑
DDC TAB		☐
Unannounced		
Justification		
By		
Distribution/		
Availability Codes		
Dist	Avail and/or special	
A		

ABSTRACT

The purpose of this paper is to describe the design and development of the University of Kansas helicopter-borne scatterometer system, HELOSCAT. The experiments performed to measure the radar backscatter from sea ice with this system along with the results are also described.

In April and May of 1978 radar backscatter measurements were made with the University of Kansas helicopter-borne scatterometer, HELOSCAT. A Bell Model 205 helicopter, used for this experiment, was based at the Naval Arctic Research Laboratories, Pt. Barrow, Alaska. Backscatter measurements were made at 1-2 GHz and 8-18 GHz frequencies, HH-polarization, and three incidence angles ($20°$, $40°$ and $60°$). Different types of ice ranging from thin ice to multiyear ice were observed; however, most data were collected from thick first-year and multiyear ice. A comparison of 1-2 GHz results for thick first-year and multiyear ice shows that the $\sigma°$ values for multiyear ice at $60°$ are slightly lower than the value for thick first-year ice. The 8-18 GHz results show that the backscatter from multiyear ice at these frequencies is higher than the backscatter return from thick first-year ice by at least 3-4 dB. The frequency response of backscatter return is an upward sloping straight line on a dB-vs-frequency plot. For the multiyear ice, only the $60°$ data was found usable; the data at $20°$ and $40°$ were determined to be erroneous because of a malfunctioning frequency counter.

In March 1979 another HELOSCAT experiment was performed as a part of the Canadian SURSAT (Surveillance Satellite) program. Backscatter measurements were made at 8-18 GHz frequencies and HH-polarization. A preliminary analysis of the thick first-year sites observed

iii

during this experiment has been done. The scattering coefficient (σ^o) versus incidence angle (θ) curves for these sites follow a downward sloping trend as expected. This result further confirms the suspicion that the anomalous results obtained for part of the spring 1978 experiment data were indeed due to the malfunctioning frequency counter. The σ^o values obtained from this experiment are generally 3-4 dB lower than the σ^o values obtained for thick first-year ice from earlier experiments (spring 1977, 1978). The reason for this can be explained by the fact that the temperatures during this experiment were at least 25° C lower than the temperatures during the earlier experiments.

TABLE OF CONTENTS

LIST OF FIGURES

LIST OF FIGURES (continued)

LIST OF FIGURES (continued)

LIST OF TABLES

1.0 INTRODUCTION

1.1 Remote Sensing

The term "remote sensing" as used by engineers and scientists means the study of distant objects using instruments. Microwave remote sensors have become established all-weather remote sensing instruments because of their unique ability to penetrate through clouds and rain. There are two kinds of microwave sensors: active and passive. Radars are active microwave sensors; two main categories of radar, imaging and non-imaging radars, may be identified.

An important type of non-imaging radar is a scatterometer. "A radar scatterometer is a device that measures the scattering properties of the region observed. Any radar that makes an accurate measurement of the strength of the observed signal is therefore a scatterometer." [12] In contrast to an imaging radar, which provides information about the terrain at only one incidence angle, a multiangle scatterometer provides more detailed information about any one point on the surface illuminated by the scatterometer beam. Consequently, multiangle scatterometers enable discrimination between different points on a terrain. Terrain roughness and characteristics are described by the parameter, scattering coefficient, σ^o, and scatterometers enable an absolute measurement of this parameter. Thus, multiangle, multifrequency, and multipolarization scatterometers enable one to discriminate between terrains of differing roughness and formation. Their primary use, however, is research aimed at optimizing imaging-radar parameters.

1.2 Remote Sensing of Sea Ice

A very large portion of the earth is covered with water, and during the winter season sea ice covers approximately 12 percent of the Earth's

waters, which is also equivalent to about 7 percent of the earth's total surface during this period. Considering the fact that the oceans and seas are an important means of providing food and transportation for all nations, it is not an exaggeration to state that the application of remote sensing techniques to the investigation of sea ice is very important indeed. Moreover, sea ice covers such a large area that it is very expensive and time-consuming to investigate its properties (roughness, thickness, etc.) by surface methods, or visually from aircraft. It is also essential that this information be available on a regular and frequent basis if it is to be used effectively. Remote sensing measurements employing microwave radars make this possible. These sensors are also capable of operating in areas like the Arctic, where weather conditions are extremely perilous and unpredictable; thus, microwave radars are very effective all-weather remote sensors.

The study of sea ice is of great importance because knowledge of ice extent and movement is important, both economically and strategically. Sea ice conditions have a major effect on countries like Canada, the Soviet Union, and Finland. They are important, but to a lesser extent, to the United States, Denmark, Norway, Sweden, Japan, and Iceland. The ice cover in the Arctic Ocean and associated areas is very important to potential naval operations involving the United States and the Soviet Union.

Commercially, the mapping of the sea ice by radar has enabled the extension of shipping seasons in the Great Lakes area. This development by the National Aeronautics and Space Administration, Lewis Research Center, has been taken over by operational agencies. The

investigation of sea ice is also important because of the recent increase in off-shore drilling for oil off the coasts of Alaska and Canada.

The Arctic and Antarctic Research Institute in Leningrad has been involved in mapping of sea ice for navigational, fishing, and research purposes since the late 1960's. These maps are prepared to 10-day intervals during summer and on a monthly basis during the winter. [20]

The unique ability of imaging radars to map sea ice regions in all-weather conditions was first recognized in the early 1960's. Scientists at the United States Army Cold Regions Research and Engineering Laboratories (CRREL) were the first to map sea ice in the Arctic region. A side-looking airborne radar (SLAR), AN/APQ-56 was used for this purpose. Anderson (1966) showed that SLAR imagery can be used to differentiate between different ice types, and thus it is able to map the sea ice in the Arctic regions. Some of the other studies dealing with radar observation of sea ice are Rouse (1969), Johnson and Farmer (1971), Glushkov and Komorov (1971), Ketchum and Tooma (1973), Parashar et al. (1977), Dunbar (1975), Dunbar and Weeks (1976), Loshchilov, Masanov and Serebrennikov (1977), Gray et al. (1977), Ketchum (1977), Onstott (1977). The majority of these studies have been done at 2 cm and 3 cm wavelengths; however, there have been a few studies at 25 cm wavelength. Some of these studies and results are described briefly in the following section.

1.3 Previous Radar Studies of Sea Ice

In May 1967 a joint experiment was conducted by the National Aeronautics and Space Administration (NASA), the Naval Oceanographic

Office, U.S. Army CRREL, The Arctic Institute of North America, and the University of Kansas employing a single frequency, single polarization radar at 2.25 cm wavelength. Analysis of the experiment data by Rouse (1969) showed that a scatterometer operating at this frequency was indeed capable of discriminating different ice types. At the 13.3 GHz frequency, multiyear ice gave stronger returns (higher σ^o) than first-year ice.

In 1969 a Philco-Ford AN/DPD-2 16.5 GHz SLAR was used to map sea ice in the Arctic regions. This radar system operated at 16.5 GHz. Johnson and Farmer (1971) used the SLAR images obtained to show that this imagery could be used to detect ice age, ice drift, surface topography, fractures, and pressure characteristics.

In April 1970 a mission was jointly undertaken by NASA, the Naval Oceanographic Office, and the University of Kansas off the coast of Alaska near Pt. Barrow, Alaska. [16] An all-polarization 400 MHz scatterometer, a 13.3 GHz vertical-polarization scatterometer, and a 16.5 GHz multi-polarized radar imager were employed in this mission. The results of this scatterometer experiment showed that, at 13.3 GHz, multiyear ice (> 180 cm thick) gives strongest returns, whereas at 400 MHz open water and first-year ice give strongest returns. Analysis showed that the higher frequency of 13.3 GHz was more suitable for discrimination of ice types. The images obtained by the 16.5 GHz radar imager were used to identify different ice types, and the categorization thus obtained was consistent with that obtained from the scatterometer data. The experiment also showed that at 400 MHz cross-polarization provides better discrimination capabilities than like-polarization.

Since the 13.3 GHz was single polarized, nothing could be determined regarding polarization effects at this frequency, but indications were that the cross-polarized returns for the 16.5 GHz imager discriminated ice types better than the like-polarized returns.

The Soviets have been using a side-looking airborne radar (TOROS) for the purpose of mapping sea ice and lake ice since the late 1960's. Loshchilov (1978) of the Arctic and Antarctic Research Institute in Leningrad, has shown that the imagery obtained by the TOROS system can be used successfully to determine ice condition and drifts. The TOROS system is horizontally polarized and is capable of looking at ranges from 20-40 km on each side of the aircraft. This system is used operationally to map ice regions on a regular basis. Preliminary maps are made on-board and sent to the hydro-meteorological centers and ships by facsimile. From the images they are able to detect different types of ice, ranging from new ice to multiyear ice; they can also determine the concentration and age from these images.

During the winter and spring of 1975-1976 ice measurements were made with a 13.3 GHz multi-polarized scatterometer off the east coast of Canada. The data obtained during these flights was analyzed by L. Gray, J. Cihlar, S. Parashar, and R. Worsfold (1977), of Canada Center for Remote Sensing in Ottawa, Canada, and Center for Cold Ocean Resources Engineering, St. John's, Canada. In this experiment, shorefast ice with varying degrees of surface roughness and snow cover, and floating ice of several different thicknesses were observed. The analysis of the data showed that the scattering coefficient at any incidence angle, for shorefast ice in this environment, varied by as much as 20 dB for HH-polarization and by 25 dB for HV-polarization.

For the thin ice the variation was of the order of 10 dB for both polarizations. These large variations in σ^o make it difficult to distinguish between the different types of ice on the basis of the backscatter parameter σ^o. However, it was concluded that radar imagery obtained by a radar operating at an incidence angle less than 60° would produce graytones that would enable reasonable discrimination of the different ice types. This imaging radar would require a large dynamic range (30-35 dB) and an incidence angle range of 10° to 60°.

In 1975 as a part of the AIDJEX and Beaufort Sea experiments, active microwave sensors were used for investigating the properties of sea ice. A 13.3 GHz scatterometer with multi-polarization capabilities was one of the sensors. The data collected during this experiment were analyzed by A.L. Gray, R.O. Ramseier, and W.J. Campbell (1977). The scattering coefficient σ^o was typically 8-10 dB higher for the multiyear ice than for first-year ice with like-polarization. For cross-polarized signals the multiyear ice σ^o was typically 15-18 dB higher than that of first-year ice. The results of this experiment showed that, in the environment studied, there is a strong correlation between magnitude of the scattering coefficient and major ice types; and old ice gives significantly higher returns than young ice and first-year ice. It was also observed that for mapping (imaging) of sea ice the important radar parameters, besides incidence angles, frequency and polarization, are spatial resolution, swath width, spatial averaging, backscatter to gray scale gain characteristics and dynamic range. The general conclusion was that a side-looking airborne radar operating at 2-3 cms wavelength and at incidence angles less than

80° would be able to obtain imagery on which gray tones would enable discrimination of different ice types.

Ketchum and Tooma (1968) analyzed the ice imagery obtained by side-looking airborne radars operating at four different frequencies: X-band, L-band, C-band, and P-band. They concluded that the images obtained at X-band were much better in enabling discrimination of ice types than the images obtained at the other three frequencies. However, they observed that there was no significant difference between the horizontal and vertical polarizations of the X-band imagery. It was believed that the strong backscatter returns for multiyear ice were due to the formation of a recrystallized snow layer between the top snow layer and the ice. No such recrystallized layer exists in first-year ice or young ice.

1.4 Recent University of Kansas Experiments

Multiangle, multi-polarization, and multi-frequency scatterometer studies provide a wealth of information about the target or terrain illuminated by the scatterometer, but correlation of aircraft data with point surface data is different. The University of Kansas' ground-based transportable scatterometer (TRAMAS) is an FM-CW scatterometer that sweeps from 1-2 GHz and 8.5-17.5 GHz. It can operate over an incidence angle range of 10° to 80°, and has multi-polarization capabilities. In the spring of 1977 this scatterometer was used in an ice measurement experiment on the shorefast sea ice near Pt. Barrow, Alaska. The results of this experiment showed for 1-2 GHz frequencies that thick first-year and multiyear ice cannot be distinguished at incidence angles between 10° and 70°. However, at these frequencies

it was possible to distinguish undeformed sea ice from lake ice and pressure-ridges. At the higher frequencies between 8.0 GHz and 18.0 GHz, it was possible to discriminate between thick first-year ice, multiyear ice, and lake ice. This experiment also showed that cross-polarization enabled better discrimination of the different ice types than like polarization [15].

In April and early May 1978 an experiment was conducted by the University of Kansas to investigate the properties of sea ice using the ground-based scatterometer TRAMAS mentioned above, and a helicopter-borne scatterometer system HELOSCAT. The HELOSCAT system uses a Bell Model 205 helicopter for an aerial platform. The antennas are side-mounted externally on the helicopter. This experiment was performed using the Naval Arctic Research Laboratories in Pt. Barrow, Alaska as the ground base. Different types of sea ice ranging from thin ice to multiyear ice were observed during this experiment; however, most data was collected from thick first-year and multiyear ice. Besides backscatter measurements, surface-truth measurements were also made at several sites.

The results of this experiment show that at L-band (1-2 GHz) the radar cross-section values obtained are in reasonable agreement with the results obtained by other experimenters during previous experiments. The HH return obtained is on the average 2-3 dB lower than that for surface-based VV measurements. The L-band results for the multiyear ice at the two lower incidence angles of 20° and 40° are extremely low, and apparently in error; however, the 60°-incidence-angle results appear to be good. The reason for the erroneous 20° and 40° incidence

angle results is believed to have been a malfunctioning frequency counter. A comparison of L-band results for thick first-year ice and multiyear ice shows that the σ^o values for multiyear ice at 60° are lower than the values for thick first-year ice. The Ku-X-band results show that the backscatter from multiyear ice at these frequencies is higher than the backscatter return from thick first-year ice by 3-4 dB. Only the 60° incidence angle results were compared because of the error in the two lower-incidence-angle data sets. The frequency-response curves follow an almost-linear (in dB) and upward sloping trend. This is in conformity with results obtained by earlier experimenters.

In march 1979 another HELOSCAT experiment was performed as a part of the Canadian SURSAT (Surveillance Satellite) program. Backscatter measurements were made at the Ku-X-band (8.0-18.0 GHz) frequencies and HH-polarization. Results obtained from a preliminary analysis of the thick first-year ice sites observed show that the radar cross-section (σ^o) versus incidence angle (θ) curves follow a downward sloping trend as one would expect. The general level of the curves is 3-4 dB lower than the spring-1977 and spring-1978 experiments, but this can be explained by the fact that the temperatures during the experiment were at least 25° C lower than the temperatures during the earlier experiments.

The purpose of this presentation is to describe the HELOSCAT experiment of spring 1978. First, the system is described in detail, and then the data analysis techniques and results of the experiment are described. Preliminary results obtained from the backscatter data collected during the March 1979 HELOSCAT experiment, are also described

briefly. These HELOSCAT experiments were meant to be a link in the chain of efforts being made to determine the optimum radar parameters for the mapping of sea ice with side-looking airborne radar systems.

2.0 HELOSCAT - THEORY AND SYSTEM DESCRIPTION

2.1 Radar Theory

A radar scatterometer is a device that measures the signal returned by the scatterers in the area illuminated by its beam. The scatterometer measures the composite signal scattered by the individual elements of the target. A radar scatterometer allows more quantitative and detailed observation of radar scattering behavior than an uncalibrated radar imager. Measurements by non-imaging scatterometers are mainly used to determine optimum radar parameters for radar imagers, and this is the goal of the scatterometer measurements of sea ice at the Universite of Kansas.

The power of the scattered signal returned by an area-extensive target is given by

$$W_r = \frac{W_t \, G_t \, G_r \, \lambda^2 \sigma^0 \, A_{ill}}{(4\pi)^3 \, R^4}$$

where

W_r = power received

W_t = power transmitted

λ = microwave wavelength

σ^0 = mean radar differential backscatter cross-section

G_t = gain of transmitting antenna

G_r = gain of receiving antenna

R = range to target

A_{ill} = area of illuminated cell

In the next few pages, the procedure and computational techniques used to determine the differential radar cross-section from the measured return power are described. The analysis technique uses an internal calibration and an extrenal calibration, as stated in Table 1. Internal calibration is done by injecting a sample of the transmitted signal into the receiver after it passes through a delay line, and for external calibration a Luneberg lens is used as a target of known cross-section.

Scattering of a radar signal from ground targets may be modelled fairly accurately by assuming that the locations of the scatterers within the illuminated cell are sufficiently random so that each one may be treated independently. This assumption enables one to obtain the total returned power from a resolution cell by adding each of the power components without any regard for phase [13]. This may be expressed in equation form as:

$$W_r = \frac{\lambda^2}{(4\pi)^3} \sum_{i=1}^{N} \frac{W_{ti} \, G_{ti} \, G_{ri} \, \sigma_i}{(R_i)^4}$$

when there are N scatterers within the resolution cell. Note that the antenna gain, illuminating power and target distance is different for each of the scattering components.

The backscatter return power, W_{rt}, from a target at a distance, R_t, is given by:

$$W_{rt} = \frac{W_{tt} \, G_t \, G_r \, \lambda^2}{(4\pi)^3 \, R_t^4} \, \sigma_t$$

where
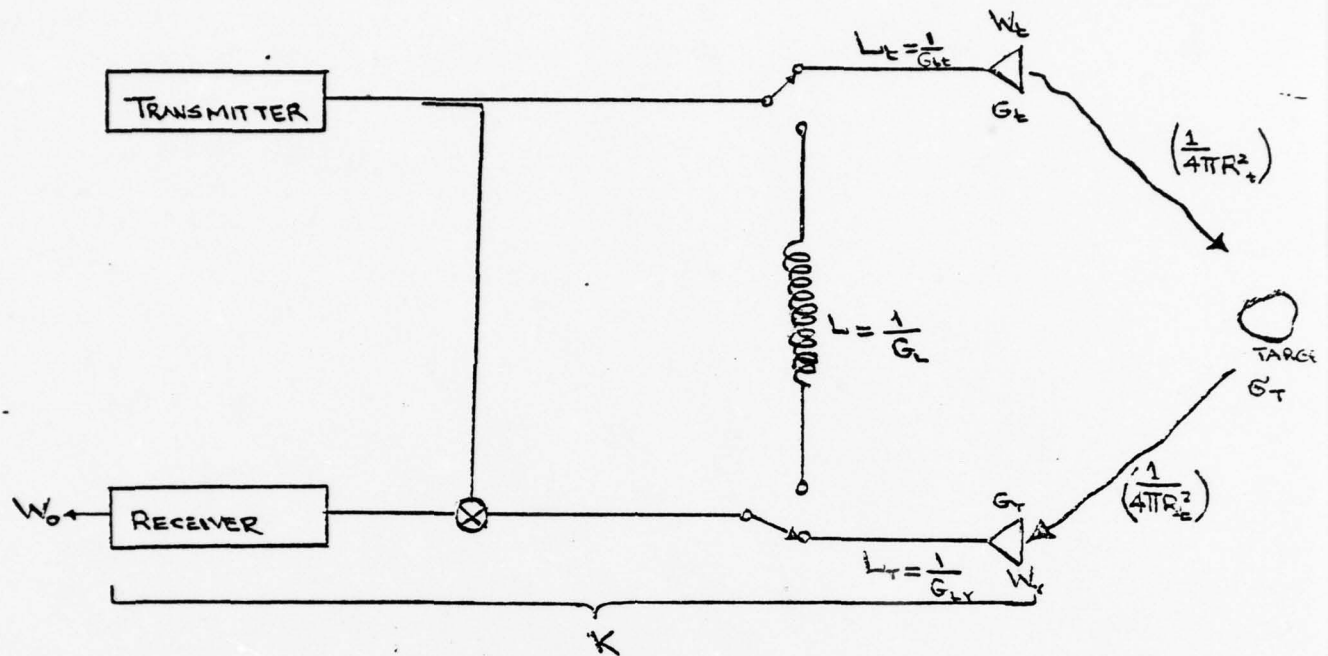
FIGURE 2.1

Simple Microwave Scatterometer

W_{tt} = power transmitted to target

G_t = maximum gain of transmitting antenna

G_r = maximum gain of receiving antenna

R_t = distance to target

σ_t = radar cross-section of the target

But

$$\sigma_t = \int \sigma^o \, g_t \, g_r \, dA$$

where:

dA = a differential element of ground area

σ^o = differential scattering cross-section (per unit area)

g_t = gain of transmit antenna within area dA

g_r = gain of receive antenna within area dA.

$$\therefore \; W_{rt} = \frac{W_{tt} \, G_t \, G_r \, \lambda^2}{(4\pi)^3 \, R_t^4} \int \sigma^o \, g_t \, g_r \, dA$$

Define:

$$M_t = \frac{W_{rt}}{W_{tt}} = \frac{G_t \, G_r \, \lambda^2}{(4\pi)^3 \, R_t^4} \int \sigma^o \, g_t \, g_r \, dA \tag{1}$$

If the power returned from the ground target is measured using square law detection, the power received at the receiving antenna, W_{rt}, is related to the measured power, W_{ot}, by:

$$W_{ot} = K_1 \, W_{rt}$$

where the proportionality constant K represents the gain in the receiver path when referring everything to the antennas:

$$W_{ot} = K_1 \, W_{rt} = K_1 \, M_t \, W_{tt}$$

$$\therefore \quad M_t = \frac{W_{ot}}{K_1 \, W_{tt}}$$

Immediately after a data reading, an internal delay line calibration is done. The power measured by the detector during this calibration will be:

$$W_{rDt} = W_{tt} L_t \frac{1}{L} L_r = W_{tt} L_t G_L L_r$$

where

L_t = loss between transmit antenna and delay line port

L_t = loss between receive antenna and delay line port

L = loss factor due to delay line cable

$G_L = \frac{1}{L}$

$$W_{oDt} = K_1 \, W_{rDt} = K_1 \, W_{tt} \, L_t \, G_L \, L_r$$

where

W_{oDt} = power measured during calibration while observing the target.

$$\therefore \quad W_{tt} = \frac{W_{oDt}}{K_1 \, L_t \, G_L \, L_r}$$

$$M_t = \frac{W_{ot}}{K_1 \, W_{tt}} = \frac{W_{ot} \, L_t \, G_L \, L_r}{W_{oDt}}$$

$$\therefore \quad M_t = \frac{W_{ot}}{W_{oDt}} \, L_t \, G_L \, L_r \qquad (2)$$

Note that the ratio, M_t, is independent of the conversion losses, but not of losses to the antennas.

The external calibration for the HELOSCAT system is done using a Luneberg lens reflector[*] placed at a distance, R_c, from the antennas. This distance, R_c, is the distance at which the antennas are focussed, i.e., the distance at which the product pattern of the antennas is a maximum. The return power from the lens as measured by the detector is W_{oL} and is given by:

$$W_{oL} = K_2 W_{rL}$$

where K_2 is the gain in the receiver path during calibration against the lens and when everything is referred to the antennas.

$$W_{rL} = \frac{W_{tL} G_t G_r \lambda^2}{(4\pi)^3 R_c^4} \sigma_L$$

$$\frac{W_{rL}}{W_{tL}} = \frac{G_t G_r \lambda^2}{(4\pi)^3 R_c^4} \sigma_L = M_L \tag{3}$$

where

---

[*]Serial No. 328, manufactured by Emerson and Cummings.

W_{rL} = return power from Luneberg lens

σ_L = radar cross-section of Luneberg lens

R_c = distance of lens from antennas

W_{tL} = power transmitted to lens

$$\therefore M_L = \frac{W_{oL}}{K_2 W_{tL}} \tag{4}$$

An internal calibration done at the end of the Luneberg lens external calibration yields the power received at the receiving antenna as:

$$W_{rDL} = W_{tL} L_t L_r G_L$$

$$W_{oDL} = K_2 W_{rDL}$$

$$= K_2 L_t L_r G_L W_{tL}$$

$$\therefore W_{tL} = \frac{W_{oDL}}{K_2 L_t L_r G_L}$$

Substituting for W_{tL} in equation (4) we get:

$$M_L = \frac{W_{oL} L_t L_r G_L}{W_{oDL}} \tag{5}$$

From equations (2) and (5) the ratio:

$$\frac{M_t}{M_L} = \frac{W_{ot}}{W_{oDt}} \cdot \frac{W_{oDL}}{W_{oL}} \tag{6}$$

and from equations (1) and (3) the ratio:

$$\frac{M_t}{M_L} = \frac{\int \sigma^o\, g_t\, g_r\, dA}{R_t^4} \cdot \frac{R_c^4}{\sigma_L} \tag{7}$$

Equating equations (6) and (7) we get:

$$\int \sigma^o \, g_t \, g_r \, dA \cdot \left(\frac{R_c}{R_t}\right)^4 \cdot \frac{1}{\sigma_L} = \frac{W_{ot}}{W_{oDt}} \cdot \frac{W_{oDL}}{W_{oL}}$$

$$\therefore \int \sigma^o \, g_t \, g_r \, dA = \frac{W_{ot}}{W_{oDt}} \cdot \frac{W_{oDL}}{W_{oL}} \cdot \sigma_L \cdot \left(\frac{R_t}{R_c}\right)^4 \qquad (8)$$

In equation (8) if we assume that the mean radar differential back-scatter cross-section σ^o is constant over the small strip of illuminated area dA, it may be removed from the integral so that now:

$$\int \sigma^o \, g_t \, g_r \, dA = \sigma^o \int g_t \, g_r \, dA$$

But:

$$\int g_t \, g_r \, dA = \text{effective area on the ground of the illuminated}$$
cell

$$\therefore \int g_t \, g_r \, dA = A_{ill}$$

Now equation (8) may be written as:

$$\sigma^o \, A_{ill} = \frac{W_{ot}}{W_{oDt}} \cdot \frac{W_{oDL}}{W_{oL}} \cdot \sigma_L \cdot \left(\frac{R_t}{R_c}\right)^4$$

$$\therefore \sigma^o = \frac{W_{ot}}{W_{oDt}} \cdot \frac{W_{oDL}}{W_{oL}} \cdot \frac{\sigma_L}{A_{ill}} \cdot \left(\frac{R_t}{R_c}\right)^4 \qquad (9)$$

This equation may be written in decibels as:

$$\sigma^o(dB) = W_{ot}(dB) - W_{oDt}(dB) + W_{oDL}(dB) - W_{oL}(dB) + \sigma_L(dB) -$$

$$10 \log_{10} A_{ill} + 40 \log_{10} R_t - 40 \log_{10} R_c \qquad (10)$$

In the above expression for the differential scattering coefficient, all terms except R_t (range to target) and A_{ill} (area of the resolution cell) are readily available. During the HELOSCAT experiment in Spring 1978, the range to target was calculated assuming that the helicopter maintained a constant altitude during data-taking. The range is related to altitude by:

$$R_t = \frac{h}{\cos\theta}$$

where

   h = altitude

   θ = angle of incidence

This can be seen from Figure 2.2.

The calculation of the illuminated area is very critical. Before the illuminated area can be computed it must be determined whether the radar is operating under beamwidth limiting conditions or filter limiting conditions. This provides the range resolution ΔR_F afforded by the radar system (see Figure 2.2). It can be seen that when the resolution cell is limited by the beamwidth, β:

$$\Delta R_F = hsec(\theta + \beta v/2) - hsec(\theta - \beta v/2)$$

$$\therefore \quad \Delta R_F = h[sec(\theta + \beta v/2) - sec(\theta - \beta v/2)] \qquad (11)$$

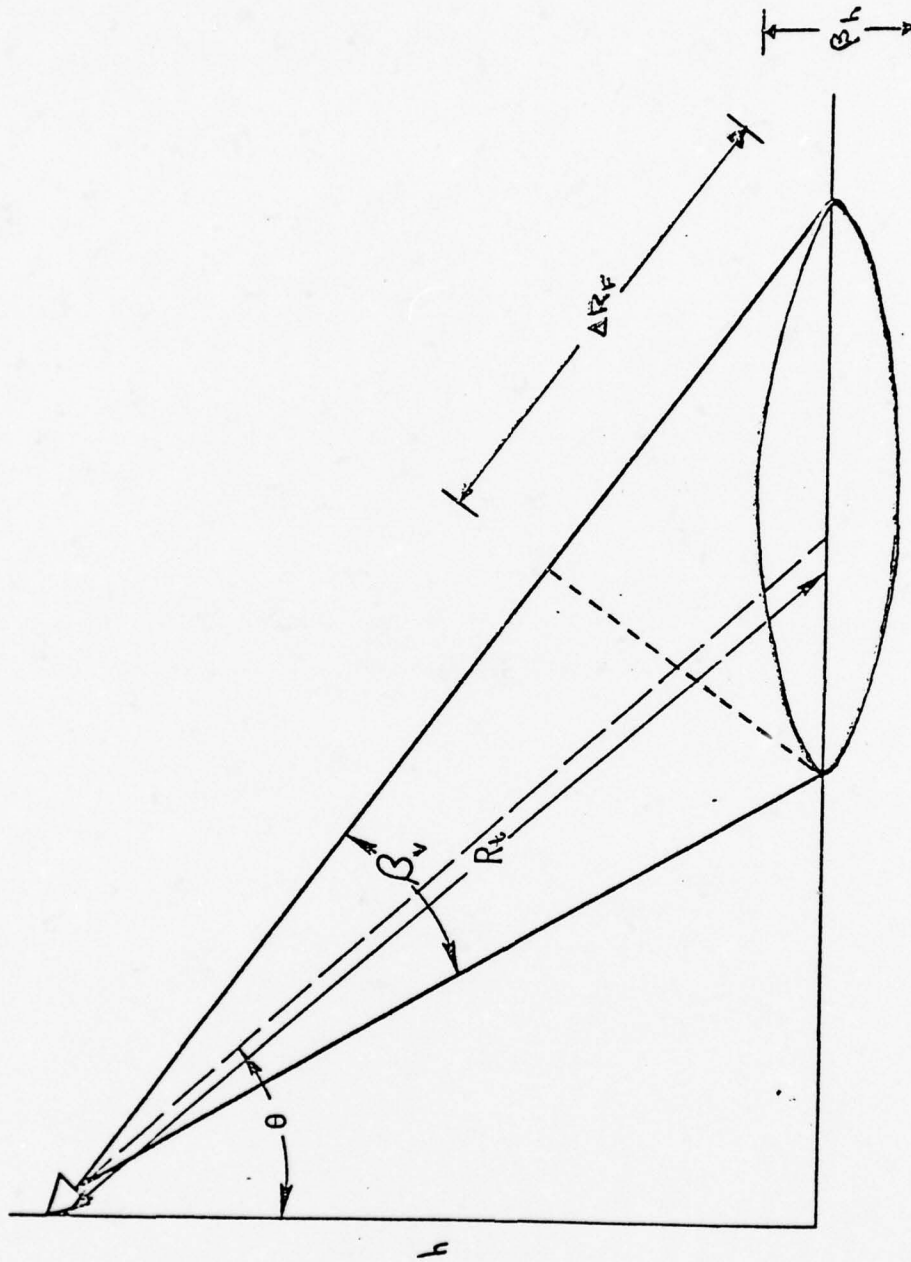When the radar system is operating under filter limiting conditions, the range resolution is given by:

FIGURE 2.2

Illustration of Parameters Used in Computing the Illuminated Area

$$\Delta R_F = R_t \frac{\Delta f_{if}}{f_{if}}$$

(12)

where

R_t = range to the target = $\frac{h}{\cos\theta}$

Δf_{if} = effective bandwidth of the IF bandpass filter

f_{if} = center frequency of the filter

The range resolution of the system under specific operating conditions also gives information about the number of independent samples that are obtainable. One quick and easy way of determining the number of independent samples obtained is outlined below briefly:

$$\Delta F_s = \frac{c}{2D}$$

where

ΔF_s = resolution bandwidth or the frequency separation between independent samples

c = speed of light

D = difference between the maximum and minimum distances from the antenna to the target in one cell.

The maximum value that D can have is equal to the range resolution ΔR_F of the radar system and at other times it may be less than the range resolution, depending upon whether the radar is filter-limited or beam-width-limited.

$$\Delta F_s = \frac{3 \times 10^8}{2D} = \frac{1.5 \times 10^8}{D} H_z = \frac{150}{D} \text{ MHz, where D is in meters}$$

ΔF_s is the frequency separation between independent samples; or, looked at another way, it is simply the bandwidth required to resolve the sample. The total number of independent samples obtained with each look of the radar may be calculated by:

$$N = \frac{\Delta F}{\Delta F_s}$$

where

ΔF = maximum RF frequency deviation

The number of independent samples N is a measure of the amount of averaging achieved because of frequency averaging. To overcome fading effects, a minimum of 50 independent samples is a good criterion to go by, since this reduces variation to $\pm$ 14 percent about the mean (about $\pm$ 1/2 dB). Unfortunately, this number cannot always be easily obtained.

2.2 Illuminated Area Calculation

Calculation of the illuminated area on the ground may be done in several different ways. The one used in the computation of σ^o values for the HELOSCAT system assumes that the radar imprint on the ice is of the form of a skewed ellipse. Referring to Figure 2.2, the semi-major and semi-minor axes a and b, respectively, are given by:

$$a = \frac{R_t}{2} \cos\theta[\tan(\theta + \beta v/2) - \tan(\theta - \beta v/2)]$$

$$b = R_t \tan \frac{\beta_H}{2}$$

where

R_t = range to target at center of beam

θ = incidence angle at center of beam

β_v = effective gain-product 3-dB beamwidth in elevation plane

β_H = effective gain-product 3-dB beamwidth in azimuth plane

Illuminated area is, therefore:

$$A_{ill} = \pi ab = \frac{\pi}{2} R_t^2 \tan \frac{\beta_H}{2} \cos\theta[\tan(\theta + \beta v/2) - \tan(\theta - \beta v/2)]$$

This expression applies when the radar system is operating under beam-width limited conditions. For the HELOSCAT experiment the system was operating under beamwidth-limiting conditions at all the incidence angles. Corrections in the incidence angle due to the roll of the helicopter, and variations in the 3 dB beamwidth must also be taken into account, and they are described in the section on antennas.

2.3 System Description

The HELOSCAT system at the University of Kansas shares the basic RF hardware components with the KU ground-based TRAMAS system. The HELOSCAT system is a CW frequency-modulated radar system that operates over 1-2 GHz and 8-18 GHz. The major design objectives kept in mind during the design and development of the system were:

(1) Availability of aerial platform, and its suitability for the experiment.

(2) Absolute measurement of σ^o.

(3) At least three discrete angles of incidence.

(4) Coverage of frequency:
   (a) SEASAT SAR frequency (1-2 GHz);
   (b) Over a continuous range 8-18 GHz

(5) Appropriate flying altitude to avoid any sensitivity problems.

(6) Rigidity of the antenna mount structure.

(7) Adequate frequency averaging without excessive loss of spectral resolution.

A block diagram of the HELOSCAT system is shown in Fig. 2.3. This system consists of the following main sub-systems or sections:

(a) Transmitter

(b) Antennas

(c) Receiver

TABLE 2.1

NOMINAL SYSTEM SPECIFICATIONS FOR HELI-BORNE SYSTEM (HELOSCAT)

|	Ku-X-Band	L-Band
Type	FM-CW	FM-CW
Frequency Range	8-18 GHz	1.5 GHz
Modulating Waveform	Triangular	Triangular
FM Sweep: Δf	1.0 GHz	800 MHz
Transmitter Power	14-19 dBm	19 dBm
Intermediate Frequency	50 kHz	50 kHz
IF Filter Bandwidth	13.5 kHz	13.5 kHz
Antennas		
Receive Type	46 cm. Reflector	91 cm. Reflector
Transmit Type	31 cm. Reflector	91 cm. Reflector
Feeds	Dual Ridge Horn	Log Periodic
Polarization Capabilities	HH	HH
Transmit Beamwidth	8.2° at 8.0 GHz 4.0° at 17.7 GHz	13.5°
Receive Beamwidth	5.3° at 8.0 GHz 2.3° at 17.8 GHz	9.5°
Incidence Angles Available	20°, 40°, and 60°	20°, 40°, and 60°
Calibration:		
Internal	Signal Injection (delay line)	Signal Injection (shorted delay line)
External	Luneberg Lens Reflector	Luneberg Lens Reflector
Operating Temperature Range	-50° C to +50° C	-50° C to +50° C
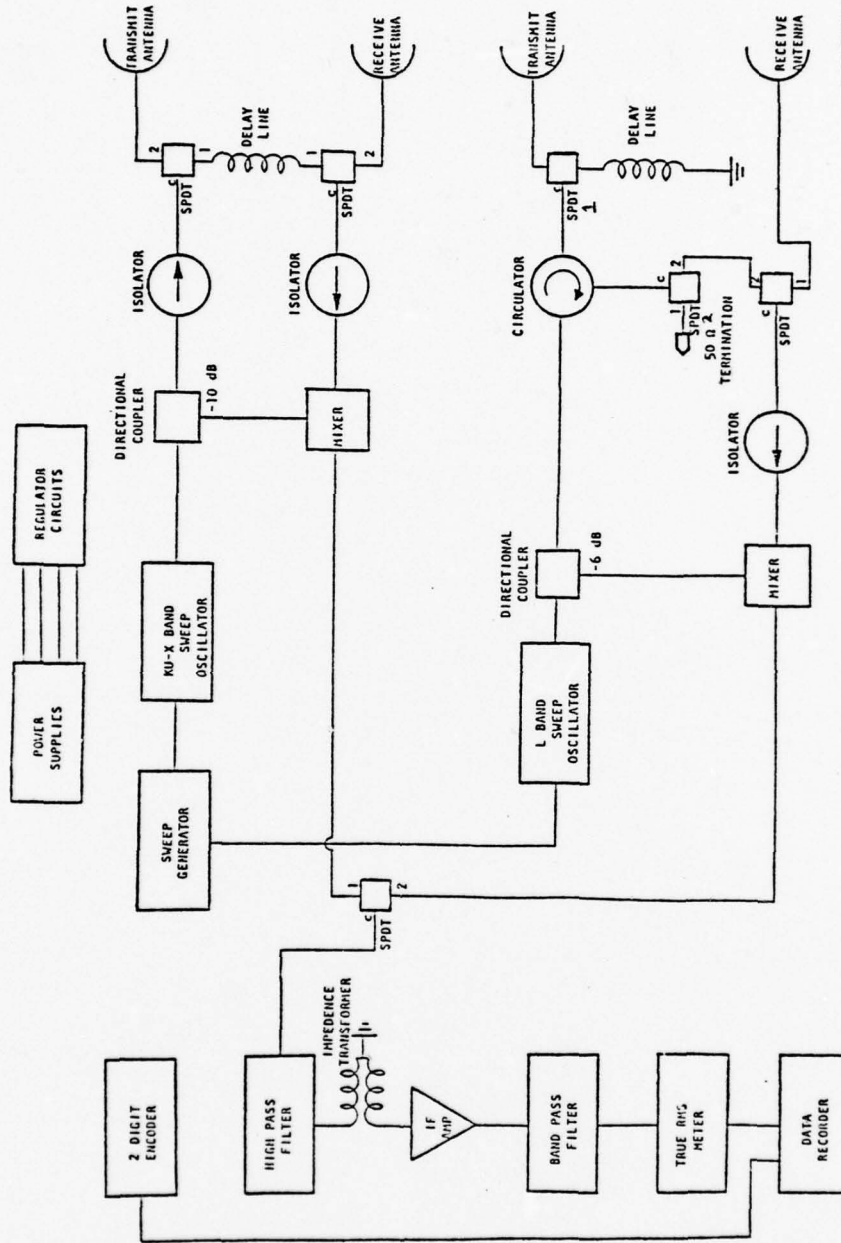
FIGURE 2.3 illustrates an RF block diagram

Each one of these subsystems will be discussed in the following sections of this chapter. Table 2.1 lists the nominal system specifications for the HELOSCAT system.

2.3.1 <u>Transmitter</u>. The transmitter section of the HELOSCAT system consists of two sweep-frequency oscillators, directional couplers, double balanced mixers, isolators and microwave switches.

The oscillators are frequency modulated by a triangular waveform generated by an INTERSIL 8038 AMDD function generator chip. It is very important that this modulating waveform be symmetrical. The frequency of this triangular waveform, F_M, determines the intermediate frequency and its amplitude determines the frequency deviation ΔF of the RF signal about the carrier frequency F_{if}. A simple but very important relationship between range, F_{if}, ΔF and F_M can be derived from the geometry in Figure 2.4. Using similar triangles

$$\frac{F_{if}}{\Delta F} = \frac{\frac{2R}{c}}{\frac{1}{2F_M}}$$

$$\frac{4RF_M}{c} = \frac{F_{if}}{\Delta F}$$

$$R = \frac{cF_{if}}{4\Delta FF_M} \underline{\hspace{3cm}}$$

(13)

where: R = range to target

F_{if} = intermediate frequency

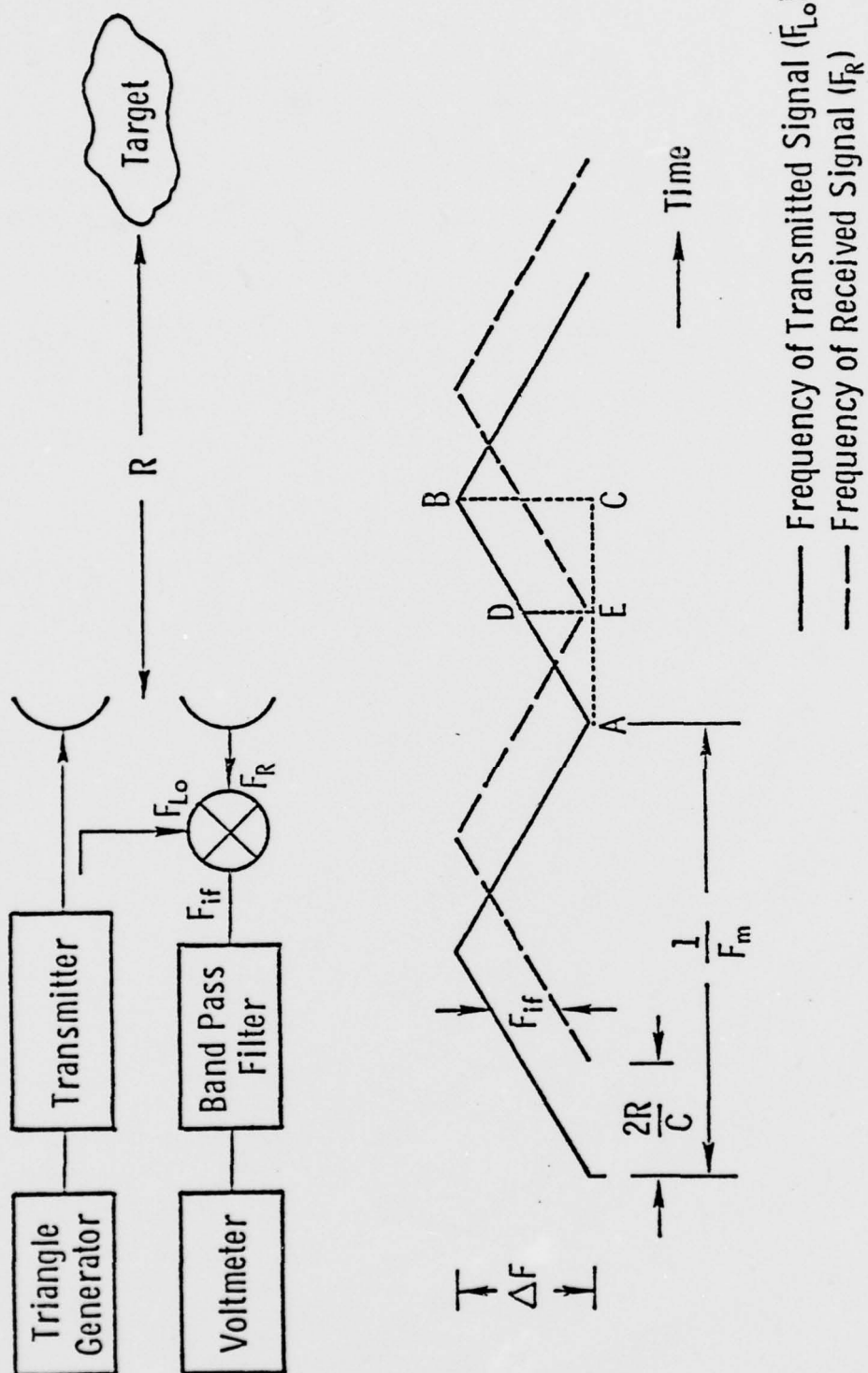ΔF = frequency deviation of the RF signal

Figure 2.4 illustrates a simplified FM-CW system

F_M = frequency of modulating waveform

c = velocity of light

Equation (13) shows that the range to the target R and the modulation frequency F_M are inversely related by the factor

$$\frac{cF_{if}}{4\Delta F}$$

For a specific radar system F_{if} is set by the center frequency of the IF filter in the receiver section. The sweep oscillators operate over the frequency ranges 1-2 GHz (L-Band) and 8.0-18.0 GHz (Ku-X-Band). The power from the oscillators is split by a -10 dB directional coupler for the Ku-X-Band frequencies and a -6 dB directional coupler for the L-Band to provide a local oscillator reference signal for the double balanced mixers.

In the Ku-X-Band system the transmitter power, after going through the directional coupler, is fed to the transmitting antenna via an isolator and a microwave SPDT switch. The isolator, which provides a minimum isolation of 12 dB and an insertion loss of 1.2 dB (typical), helps avoid any possible damage to the oscillator due to unwanted reflections. It also reduces noise in the system. The microwave SPDT switch provides switching between the transmit antenna and the delay line for purposes of internal calibration.

For the 1-2 GHz system a slightly different arrangement is used. The isolator is replaced by a circulator that connects to two microwave SPDT switches. One port of SPDT 2 switch is ended with a 50 Ω termination, so when the switch is in this position the circulator acts as an isolator. The system is in this configuration during the time
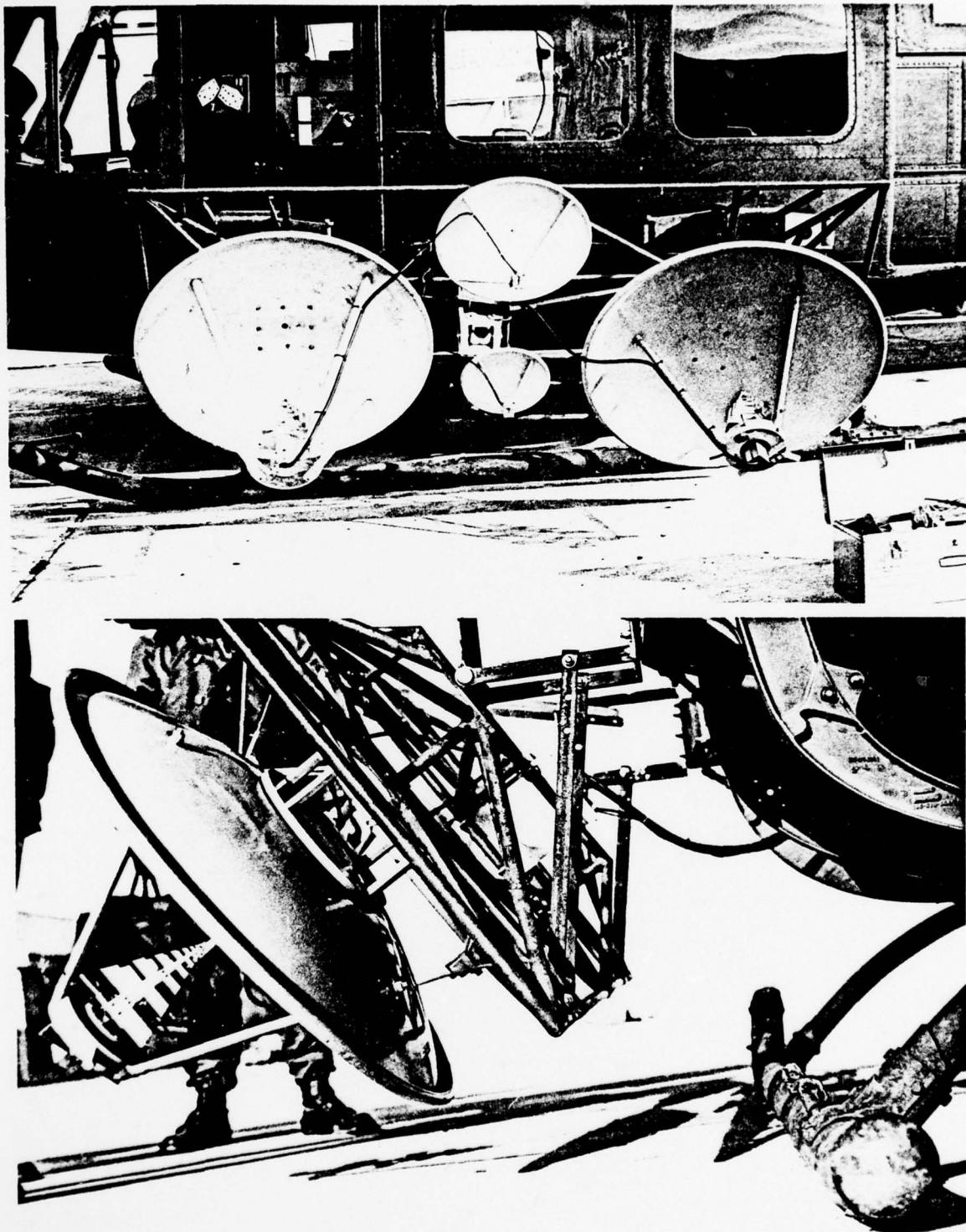
Figure 2.5
Antenna Structure Attached to the Bell Model 205 Helicopter Fuselage

when a target is being observed. During the calibration mode port 3 or the circulator is used as the output port, and so the signals from the antenna side of the circulator pass through the circulator and on to the mixer.

2.4 Antennas

The antennas on the HELOSCAT system are side-mounted externally on the helicopter. The four antennas are mounted on a rigid chromalloy structure which is attached to the Bell auxiliary kit (external stores rack) by means of angle-changing blocks. Chromalloy is a light but very strong alloy that is used extensively in aircraft structures. The two Bell auxiliary kits attach to the helicopter fuselage at the eight hardpoints provided on the helicopter (four forward and four aft). (See Figure 2.5). The two 3.0-foot L-Band parabolic dishes and the two smaller Ku-X-Band antennas are all mounted on this structure. A TV camera in the center of this structure is installed to enable monitoring of the targets within the antenna beams. This antenna mount allowed for three discrete look angles, namely 20°, 40° and 60°. Figure 2.6 shows another view of the antennas when mounted on the helicopter.

The antenna structure was supported on stands during the focussing and calibration processes. The antennas were focussed at a distance corresponding to the intermediate range, i.e., the range corresponding to approximately an incidence angle of 40° and an altitude of 100 feet. The focussing was done using thin washers in the backplates of the antennas.

2.4.1 Calculation of Effective Beamwidth. The L-band antenna dishes have log-periodic feeds, while the Ku-X-Band antennas have dual-
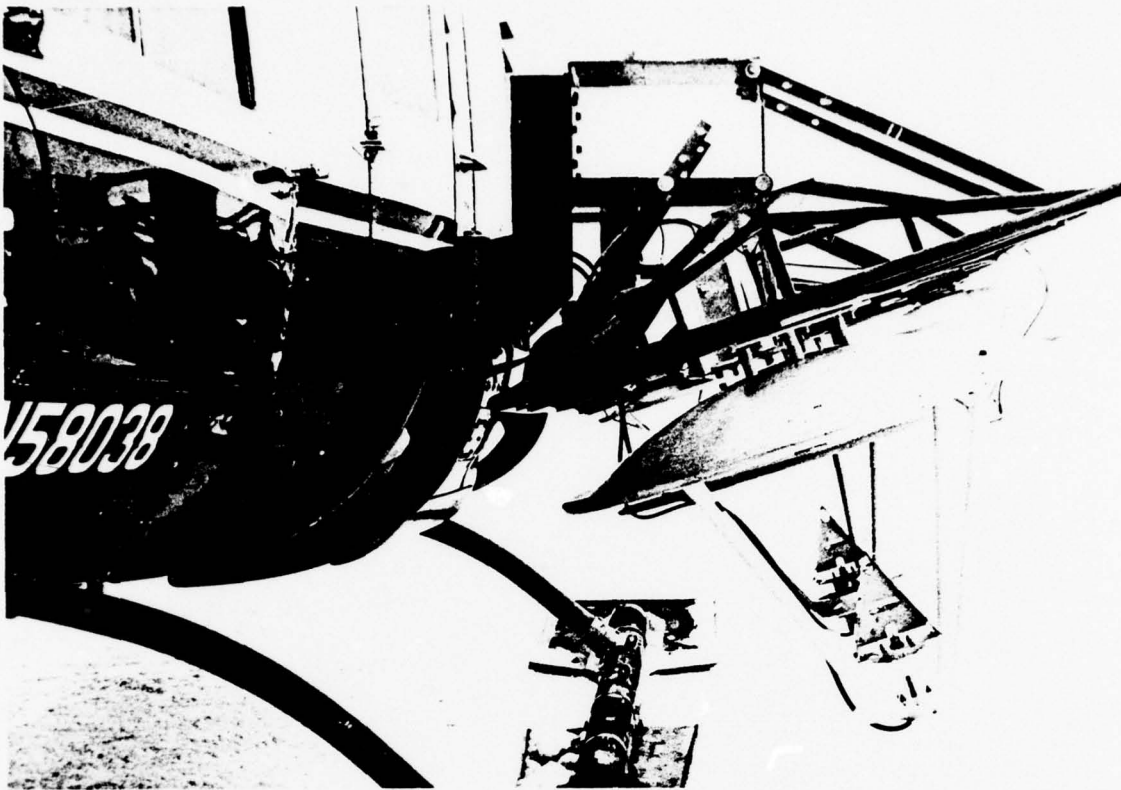
FIGURE 2.6
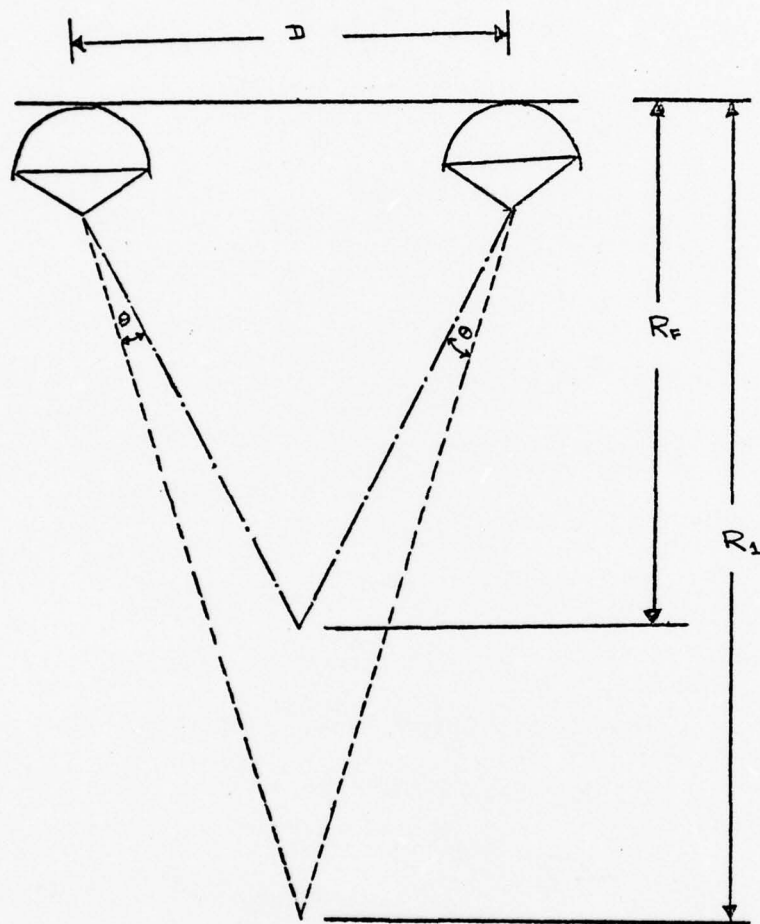A View of the HELOSCAT Antennas Mounted on the Helicopter

FIGURE 2.7

Illustration of the Antenna Pointing Error for the HELOSCAT System

ridge horn feeds. Antenna patterns for the individual antennas were obtained on the University of Kansas antenna range and the product patterns ($G_t.G_r$) and the product beamwidths were obtained by plotting out the product patterns. The 3 dB beamwidths obtained in this manner are the beamwidths suitable for the 40° incidence angle. The beamwidths at the 20° and 60° incidence angles are calculated by determining the shift in the peaks of the transmit and receive antenna patterns.

Referring to Figure 2.7, R_F is the range corresponding to the distance at which the antennas are focussed, i.e., the distance at which the receive and transmit antenna patterns overlap completely. R_1 is the range corresponding to an incidence angle other than the 40° at which the antennas are focussed. The shift in the peaks of the transmit and receive antenna patterns is given by the angle 2θ, and where

$$\theta = \tan^{-1} \frac{(D/2)}{R_F} - \tan^{-1} \frac{(D/2)}{R_1}$$

and 'D' is the separation of the two antennas. The maximum displacement of the peaks occurs at L-band and 60° incidence angle, and for the HELOSCAT system this was found to be 1.9°. The products ($G_t.G_r$) of the shifted patterns are plotted and the 3 dB product beamwidth is thus obtained. Antenna patterns are presented in Appendix B.

The illuminated area is calculated from this beamwidth as outlined in Section 2.2.

2.5 Receiver

The receiver section of the HELOSCAT system consists of a receiving antenna, an isolator, a mixer, a high-pass filter, an impedance transformer,

an IF amplifier, a band-pass filter and a true RMS meter. Refer to Figure 2.3.

The signal received by the receiving antenna passes through the isolator and is fed into the mixer. The isolator provides damping of any reflections caused by the mixer, connector, coaxial cable, and antenna feed mismatching. The mixer is provided with a local oscillator signal from the directional coupler in the transmitter section. The mixer output contains the difference and sum frequencies of the received and LO signals. It also contains the low-frequency, large-amplitude, intermodulation noise and antenna feed-through noise. The intermodulation noise is caused by the modulation of the local oscillator signal. The mixer output is fed into a high-pass filter which has a cut-off frequency of 35 kHz. This high-pass filter attenuates signals below 22 kHz by at least 40 dB, thereby ensuring that no low frequency components will reach the intermediate frequency amplifier and cause saturation. The frequency response curve for the high-pass filter is shown in Figure 2.8.

The high-pass-filtered signal is fed into the IF amplifier via a 1:10 impedance transformer. The impedance transformer transforms the output impedance of the high-pass filter from 50 ohms to 5000 ohms. The IF amplifier is an HP model 465A laboratory amplifier. It has an input impedance of 10 megohms shunted by <20pF, and a 50 ohm output impedance. The impedance transformer improves the signal-to-noise ratio. The IF amplifier provides a choice of gains of 20 dB or 40 dB over a continuous frequency range of 5 Hz to 1 MHz. Tests proved that the lower gain setting of 20 dB provided a more suitable system

sensitivity than the higher gain of 40 dB, and also provided a lower signal-to-noise ratio.

The amplified IF signal is then fed into the band-pass filter. The filter has a center frequency of 50 kHz and a 3 dB bandwidth of 13.5 kHz. The frequency response characteristics of this filter are shown in Figure 2.9. The width of the pass band ensures that most of the received signals from the target are retained while all other unimportant signal components are attenuated. The filtered signal of interest is fed into a true-RMS voltmeter that utilizes square-law detection. The absolute dBm reading is recorded on paper tape using a digital printer. The meter has autoranging capabilities and can measure signals from -7 dBm to +50 dBm.

2.6 Calibration

As shown in Section 2.1, the expression for calculating σ^o is

$$\sigma^o = \frac{W_{ot}}{W_{oDt}} \cdot \frac{W_{oDL}}{W_{oL}} \cdot \frac{\sigma_L}{A_{ill}} \cdot \left(\frac{R_t}{R_c} \right)^4 \tag{9}$$

where:

W_{ot} = power transmitted

R_t = range to target

R_c = distance to the lens during calibration

A_{ill} = area of illuminated cell

W_{oDt} = delay-line reading while observing target

W_{oDL} = delay-line reading while observing lens

W_{oL} = power returned from lens

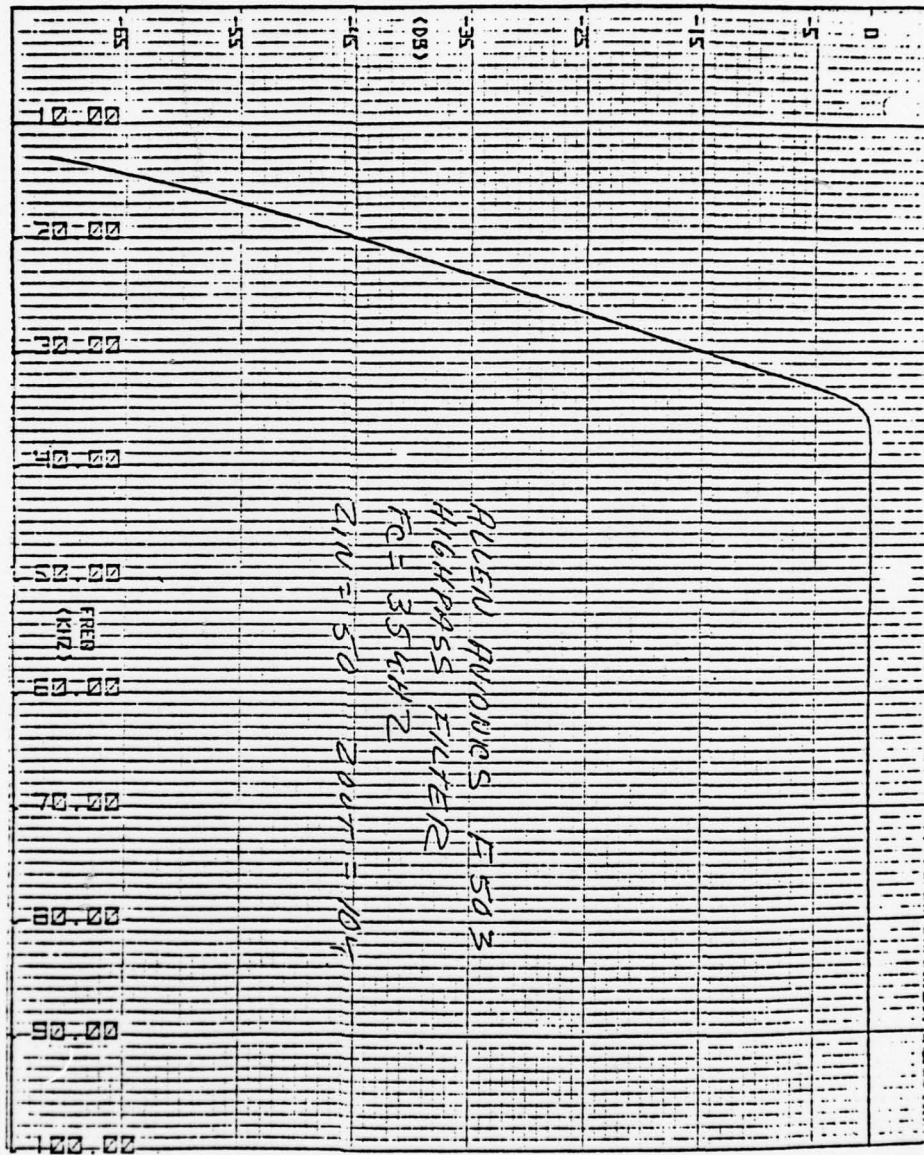σ_L = radar cross-section of the standard radar target.
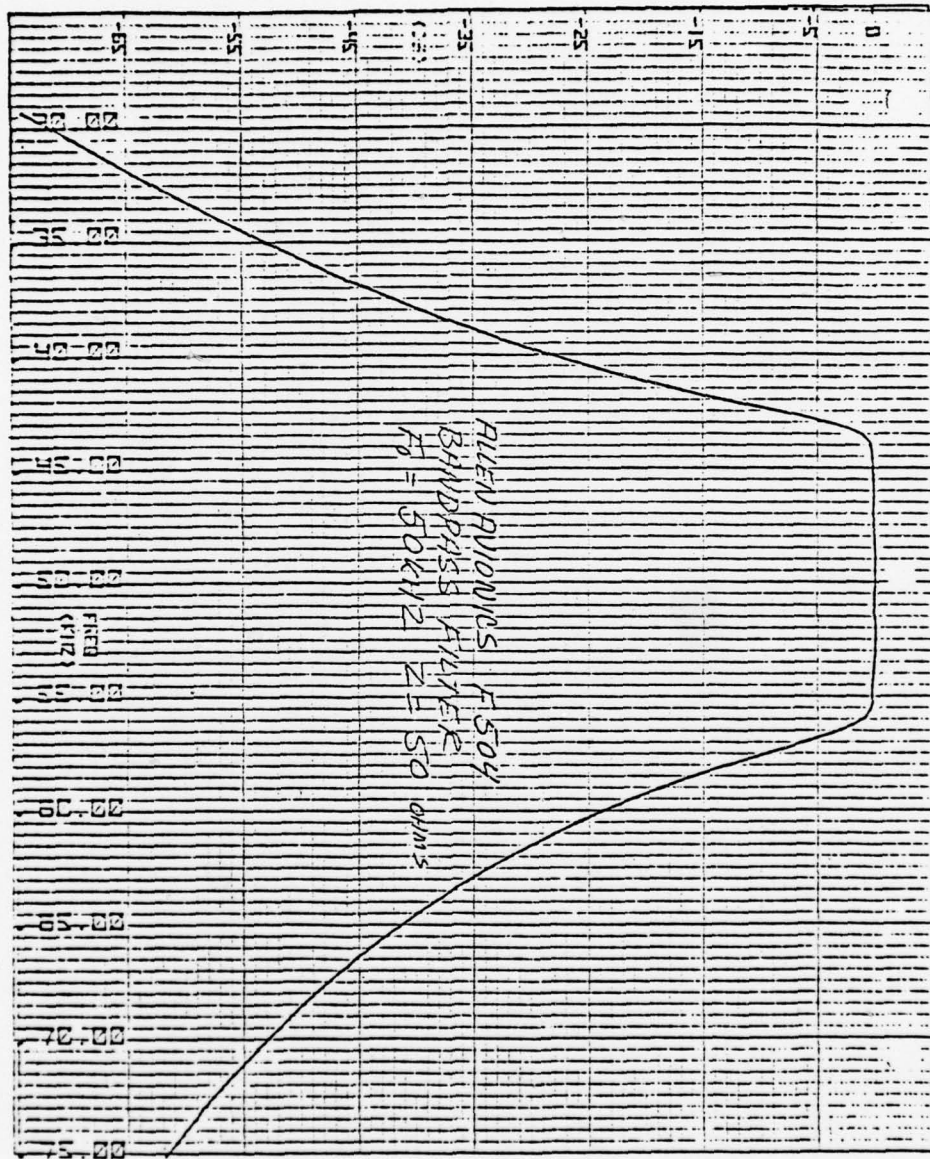
FIGURE 2.8

High-Pass Filter Characteristics

FIGURE 2.9

Band Pass Filter Characteristics

In the above equation the terms R_c, W_{oDt}, W_{oDL}, and W_{oL} are obtained from the calibration of the system. As a part of the Spring 1978 HELOSCAT experiment, system calibration was done before, during, and after the mission. Two types of calibration were used, an internal calibration and an external calibration. These calibrations compensate for any W_t and K_1 variations in the derivation of the σ^o expression discussed in Section 2.1. Figure 2.10 shows the HELOSCAT system during calibration.

The external calibration procedure for the HELOSCAT system involved using the Luneberg lens mounted on a stand. The antenna mount structure was placed on support stands about 2 feet high. The lens was placed at a distance corresponding to the intermediate range, i.e., the range at the 40° incidence angle. The antennas were focussed at this distance by adding or removing thin washers on the back plates of the antennas. At this distance the power returned from the lens in peaked by varying the FM rate. This was done for the 1 to 2 GHz frequency and the Ku-X-Band frequencies. At Ku-X-Band the lens was peaked at 9.0 GHz and it was assumed that this would hold good at the remaining Ku-X frequencies too. The power returned from the lens in this set-up gives W_{oL}. During the course of this calibration a delay-line reading, W_{oDL}, is also taken. This is obtained by injecting a sample of the transmitted signal through a delay line of known length and attenuation.

Similarly, the lens was peaked at the other two ranges corresponding to the 20° and 60° incidence angles. The optimum FM rates required for both the 1-2 GHz and 8.0-18.0 GHz system operation were recorded.
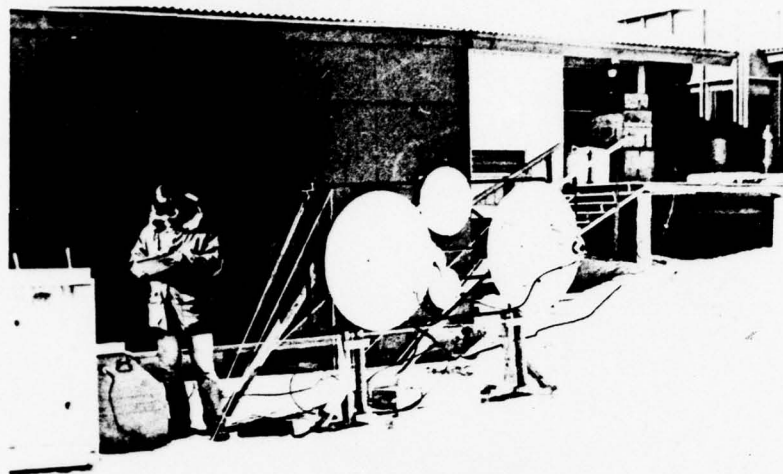
FIGURE 2.10

HELOSCAT System Calibration in the Arctic

These FM rates were the ones used during data-taking in the HELOSCAT experiment. It was noted that the FM rates thus obtained were not the same as those obtained from theoretical calculations using the equation

$$F_m = \frac{cF_{if}}{4\Delta fR} \tag{14}$$

A possible reason for this may be inherent radar characteristics not accounted for in the theoretical computation.

3.0 DESIGN AND DEVELOPMENT OF THE HELOSCAT SYSTEM

The design of the HELOSCAT system was undertaken with two primary considerations in mind, namely: (a) minimal modifications to the existing hardware of the ground-based scatterometer TRAMAS, (b) a practical and rigid antenna mount structure. Since the HELOSCAT system shares the ground-based TRAMAS system hardware, the scatterometer can be used for ground-based or helo-borne experiments without requiring much modification.

3.1 System Design and Development

3.1.1 System Sensitivity. The optimum flying altitude for the system was determined by calculating the achievable system sensitivity at several altitudes. Sensitivity for the scatterometer is given by the following equation which is the radar range equation modified for sensitivity calculations [12]

$$S = \frac{W_t G_t A_r \sigma^o A_{ill}}{(4\pi)^2 R^4 k T_o F B}$$

S = S/N ratio expressed in terms of input level

W_t = power transmitted

G_t = gain of transmitting antenna in the direction of target

A_r = effective area of receiving antenna

A_{ill} = area of illuminated cell on the ice

R = range to target

k = Boltzman's constant

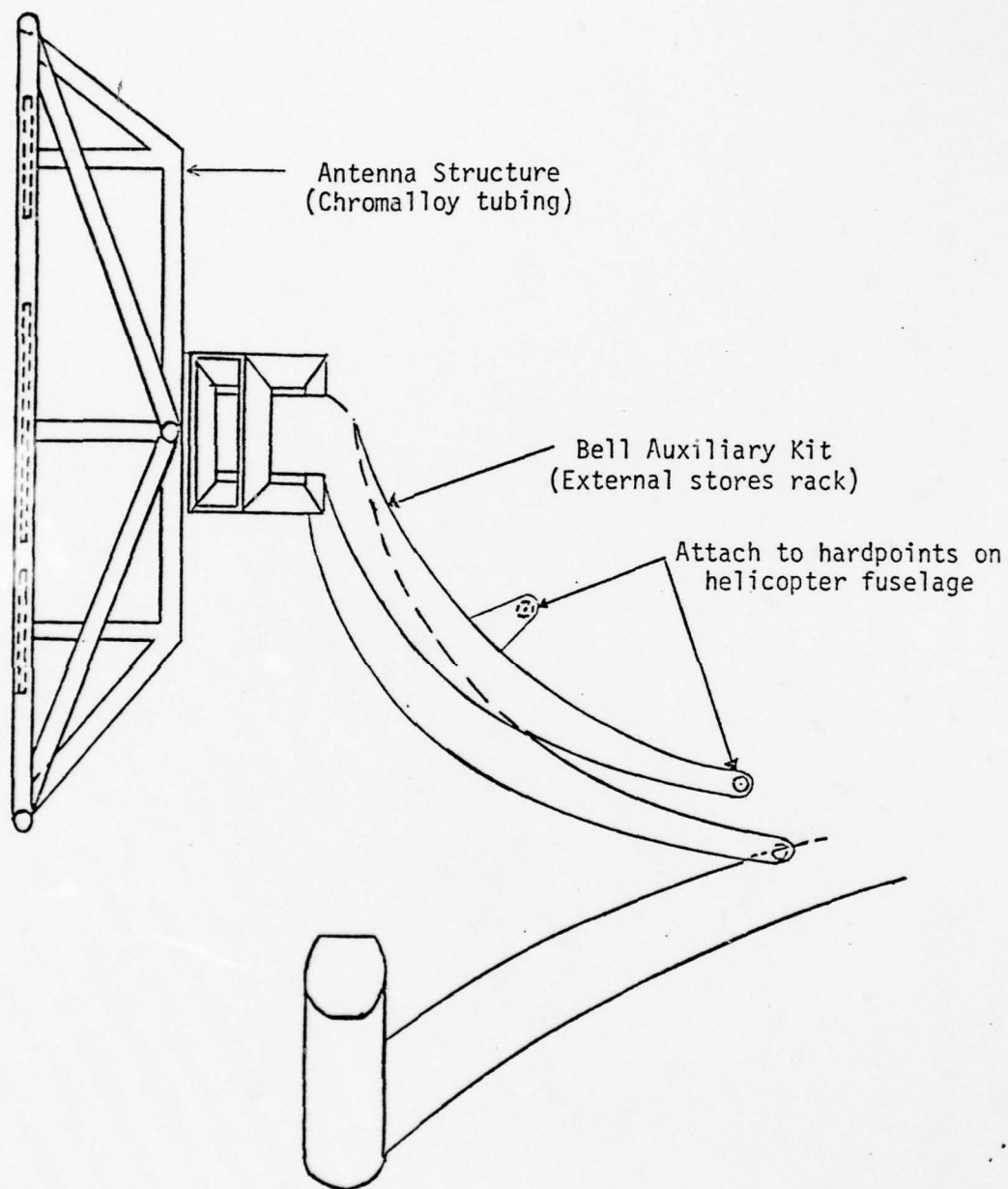T_o = noise temperature of receiver

F = noise figure of receiver

Antenna Structure
(Chromalloy tubing)

Bell Auxiliary Kit
(External stores rack)

Attach to hardpoints on
helicopter fuselage

FIGURE 3.1

Sketch of Antenna Structure Attached to the External Stores Rack

B = receiver bandwidth = IF bandwidth

σ^o = typical scattering coefficient for the type of target

$$ S = \frac{W_t G_t A_r \sigma^o A_{ill}}{(4\pi)^2 h^4 \sec^4_\theta\, kT_o FB} $$

where:

R = hsecθ

and h = flying altitude

θ = incidence angle

The results of this calculation showed that for the HELOSCAT system a signal to noise ratio of 50 dB was achievable at 1-2 GHz, while flying at an altitude of 100 feet.

3.1.2 <u>Incidence Angles and Polarization</u>. The range of angles of incidence for the HELOSCAT system was originally from 10° to 70°. However, due to the structural complexity involved in implementing this range of incidence angles, it was decided to have a capability of three discrete incidence angles, initially. The three angles chosen were 20°, 40°, and 60°. The 20° incidence angle was chosen because the SEASAT SAR (synthetic aperture radar) operated at 20° incidence angle. The polarization chosen was HH, to be the same as that of the SEASAT SAR.

3.2 <u>Antenna Mount Design and Development</u>

A Bell Model 205 helicopter was selected as the platform for the air-brone scatterometer experiment. The choise of this particular helicopter was influenced by the following factors:

(a) general availability of the helicopter type in both the
   Arctic region and around Lawrence, Kansas,

(b) a large enough size to be able to support a structure on
   which the two 3.0 ft. parabolic dishes could be mounted,

(c) operational capabilities like hovering ability, dependability,
   cold weather operation, etc.

After an extensive study of the various methods of attaching the
antenna mount to the helicopter it was decided to utilize an external
stores rack auxiliary kit (Bell Helicopter No. 205-706-013) to accom-
plish this. This auxiliary kit, shown in Figure 3.1 is used by the
U.S. Army for the purposes of carrying auxiliary fuel tanks, mounting
machine guns and for carrying missile pods. Two auxiliary kits were
used for attachment, one fore and one aft. These kits are mounted on
the hardpoints in the airframe of the helicopter. Each of these hard-
points can support 750 pounds maximum. Additional drawings and infor-
mation on the kits is presented in Appendix A.

The initial design of the antenna mount called for an automatic
remote-controlled angle-changing system. This design was to employ
an actuator for accomplishing this; however, because of the short amount
of time, the complexity, and the concern about proper actuator operation
in sub-zero weather, it was decided to proceed with a manual angle
changing antenna mount. The possibility of automating the angle
changing in the future was left open.

The structure on which the four antennas are mounted is made out
of 1.0 inch circular tubing of chromalloy. This truss-like structure
is about 96.0 inches in length, 40.0 inches high and 10.0 inches deep.
A sketch of the structure and the antenna mounting configuration is
shown in Figure 3.2. The four antennas, i.e., the two 3.0 foot parabolic
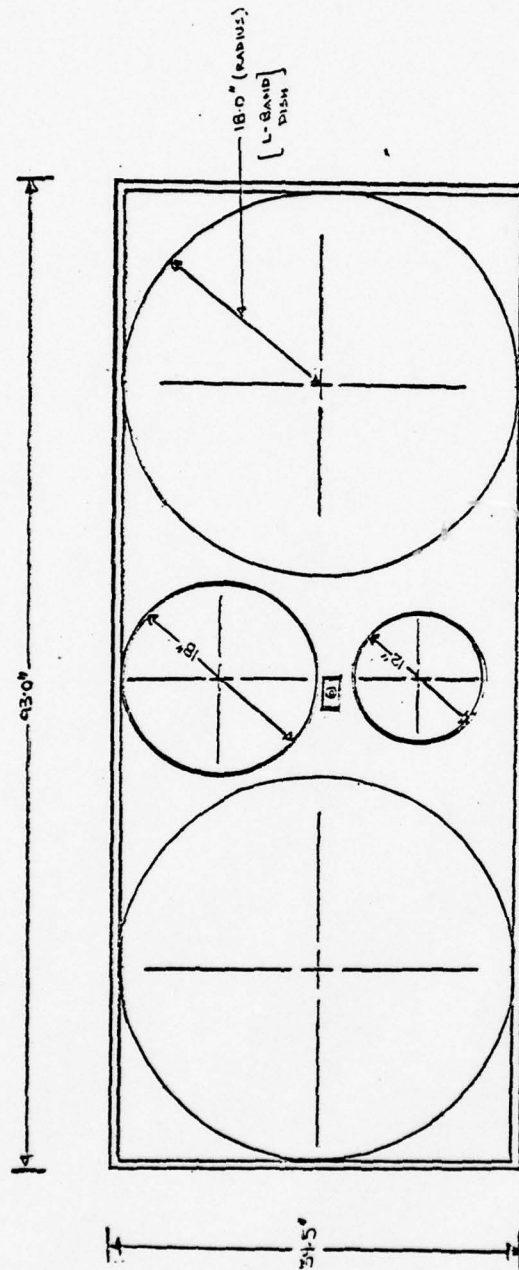
FIGURE 3.2

Front View of Antenna Mount Structure

dishes and the two smaller parabolic dishes are mounted on this structure with a TV camera in the center. The TV camera enabled the experimenters in the helicopter to see the target area within the beam of the antennas. The antennas were attached to the structure by means of flat aluminum plates and locking nuts and bolts. The antenna mount structure with all four antennas and the TV camera mounted on it weighs about 150 pounds.

The antenna structure is attached to the Bell auxiliary kits by the angle changing blocks. These blocks are made of 1030 steel. The eight 1/4-inch-wide steel straps shown in the photograph in Figure 3.3 are used to hold the structure rigid at the incidence angle set. The initial design of the extension blocks (angle changing) did not allow enough ground clearance for the large 3.0 foot dishes at the incidence angle of 20°; so adapter blocks had to be utilized to raise the structure to provide the necessary ground clearance at all the incidence angles.

The angles are changed by loosening and retightening of eight bolts and nuts on the steel straps. All the hardware used on the antenna mount was of aircraft quality to provide the necessary rigidity and reliability. Throughout the design and fabrication of the antenna mount, extreme care was taken to make it rigid and relatively free of low frequency vibrations, which are so common in helicopters. A stress analysis was performed on the structure and it was found to be adequately rigid and strong. The stress analysis computations and results are published in University of Kansas RSL TM 331-7.

FIGURE 3.3

Photograph Showing Steel Straps Holding Structure

4.0 SPRING 1978 HELOSCAT EXPERIMENT AND RESULTS

The HELOSCAT experiment was conducted in the first week of May 1978 from a ground base at the Naval Arctic Research Laboratories facility outside of Point Barrow, Alaska. In the following sections a brief description is presented of the site and experimental procedures used.

4.1 Site Description

The ice conditions along the coast near Point Barrow were somewhat chaotic at the time of the HELOSCAT experiment. Since collecting surface truth was a vital part of the experiment, it was essential that the ice sites studied be fairly smooth to allow helicopter landing safely; unfortunately, relatively smooth ice was at least 20-30 miles off the coast. Identification of first-year ice was not very difficult because of its relatively smooth surface. However, locating multiyear ice sites within 30 miles or so off the coast was a little difficult because these sites were usually surrounded by large expanses of rough, thick first-year ice, which made aerial identification difficult. Multiyear ice sites had a bluish tint and had a generally rolling formation due to melt ponds and hummocks. Other ice type identification (pressure ridges, thin-ice) was quite easy. The categories of sea ice observed were thick first-year ice, multiyear ice, pressure ridges, and thin ice; however, most data was collected on multiyear and thick first-year ice sites.

4.2 Data-Acquisition and Equipment Set-Up

This section outlines the methods of equipment set-up and data-acquisition that were adopted during the spring 1978 HELOSCAT experiment.
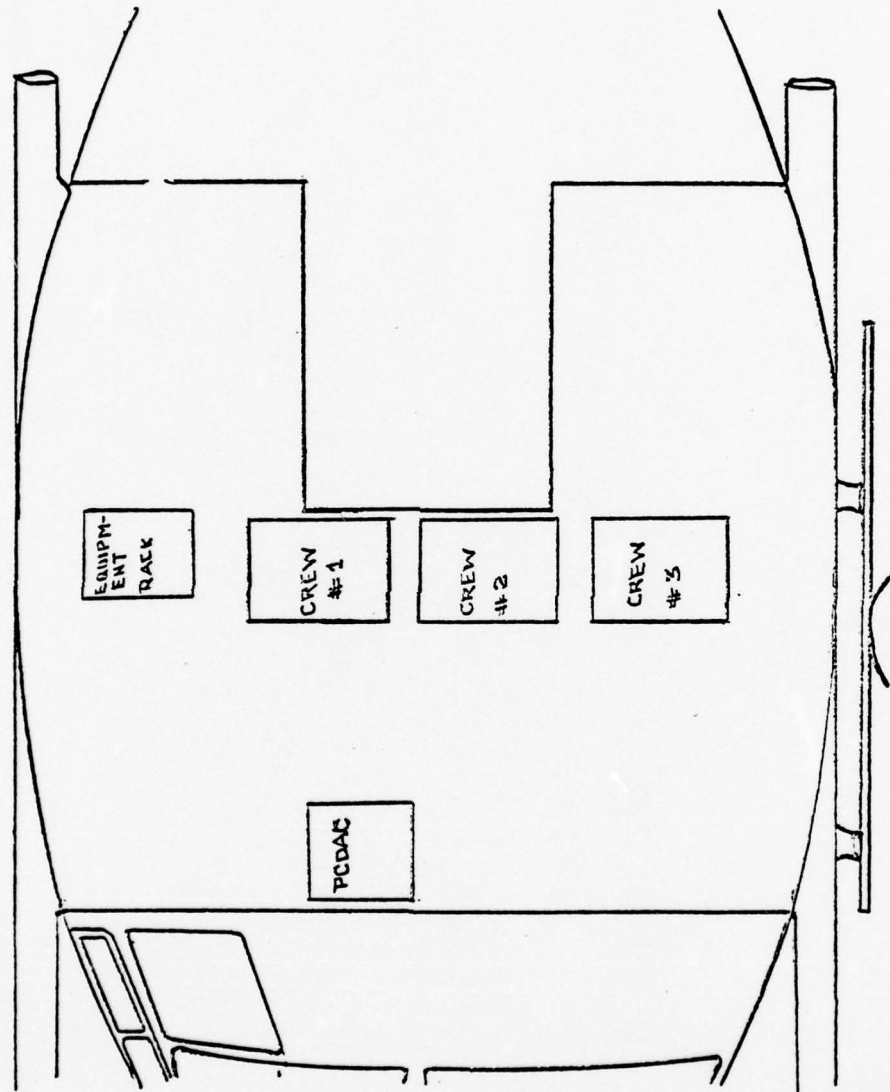
FIGURE 4.1

Internal Layout of HELOSCAT Equipment

The antennas and the TV camera were the only pieces of equipment that were mounted outside the helicopter. All the electronics gear was shock mounted, using Barry shock mounts, to boards, and these boards were strapped to the helicopter floor with nylon straps. The internal layout of the equipment and crew members is shown in Figure 4.1. During most of the data-taking period two crew members were in the helicopter. One would monitor the equipment, and the second took notes on the salient features of the site and any other relevant information; he was also responsible for communicating with the pilot via the intercom headset. The procedure adopted during a typical data set collection may be described by the following steps (refer to Table 4.1: TABLE OF TIMINGS):

(a) One of the three discrete angles (20°, 40°, 60°) available on the helicopter antenna mount structure was set and the helicopter took off. No equipment was turned on until the helicopter was five miles away from Barrow Airport control tower, to avoid interference with the helicopter navigational and communication systems.

(b) The electronics gear on the HELOSCAT system runs on 120 volts and 60 Hz. This was obtained by supplying 28 volts DC from the helicopter's battery to a 120 volt AC static inverter. The equipment was turned on and allowed to warm up. Delay line readings at L-band and Ku-X-Band were taken.

(c) After flying 20-30 miles into the pack, a site was identified from the air and backscatter measurements were made at this site with the helicopter in the hover mode at 100 feet altitude. The helicopter then landed at this site.

(d) The site was marked with dye-markers for easy identification from the air; also any other interesting sites in the vicinity were marked with dye-markers. The surface-truth equipment was unloaded, and the angle of incidence of the antennas was changed. The changing involved loosening and then tightening 8 bolts and nuts. The angle-changing procedure took about 10 minutes.

(e) One person of the three-man team stayed at the site to collect surface truth data. The helicopter took off and hovered at an altitude of 100 feet over the marked site which was displayed on the TV monitor to ensure that the same site was being observed. Several backscatter measurements were taken at this site and any other nearby marked site for that particular angle.

(f) The helicopter was then set down at the marked site and the third angle was set as described earlier. The helicopter took off and hovered again at an altitude of 100 feet, collecting backscatter data at this new incidence angle. After this, the helicopter landed and the surface truth measurements were completed. The surface truth equipment was put aboard the helicopter and a new site was selected, and the same kind of data-taking procedure was employed there.

4.3 Surface-Truth Measurements

This section describes the different kinds of surface-truth measurements made during the HELOSCAT experiment, and the procedures adopted

TABLE 4.1

APPROXIMATE TIMES FOR DATA TAKING PROCEDURE WITH HELOSCAT SYSTEM*

OPERATION	TIME IN MINUTES
Backscatter measurement at first angle	7-10
Change to second angle	10-15
Backscatter measurement at second angle	7-10
Change to final angle	10-15
Backscatter measurement at third angle	7-10
Land, complete ground truth and load ground truth equipment	15

*This is the approximate time required for investigating one site involving three persons.

to obtain them. Surface-truth data was collected at the sites wherever
it was possible. The main categories of surface-truth made are the
following:

(A) Snow Conditions

(1) Snow surface temperature - the temperature of the snow layer
over an ice site was measured using a Fastemp portable temper-
ature meter and a surface probe. If the snow layer was thick,
both air-snow surface interface and snow-ice interface temper-
atures were recorded.

(2) Snow depth - the depth of the snow cover on the ice surface
was measured with a meter rule at several points on the
site, and a mean snow depth was arrived at.

(3) Snow wetness - the snow wetness was established only in a
qualitative way; no quantitative measurements were made.

(4) Other surface-truth measurements of snow included taking snow
samples for salinity purposes and also obtaining a general
description of the texture and grain size of the snow layer.

(B) Ice Conditions

(1) Ice type - the type of ice being observed was identified by
visual inspection and usually verified when a core was
drilled at the site. Figure 4.2 shows some core photographs.

(2) Ice surface temperature - the snow layer was removed from the
ice surface and its surface temperature was taken using the
surface probe and Fastemp portable temperature meter.

(3) Ice thickness - at almost every site, depth was measured
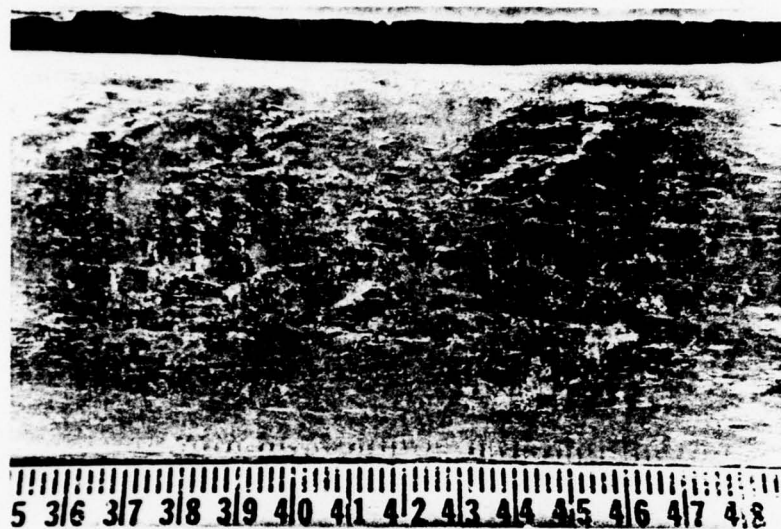using an ice auger and measuring tape.
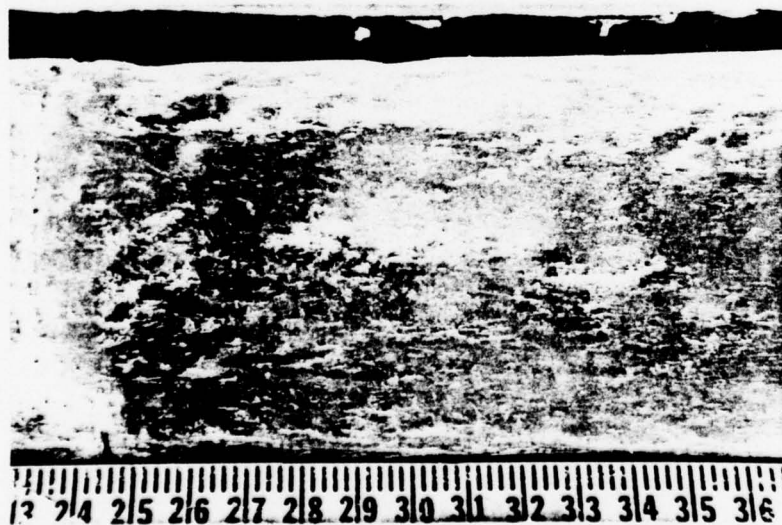
FIGURE 4.2

Photographs of Core Samples

(4) Ice-surface roughness - a small section of the ice site being observed was cleared of the snow layer and then using a straight-edge (meter rule) the undulations in the ice surface were noted. Other features like density and size of air bubbles in the ice surface were also noted.

(5) Salinity - ice cores drilled at a site were photographed in entirety first, and then cut up into 10-12 cm sections to be put into plastic containers. These core samples were taken back to the laboratory for salinity measurements. Salinity profiles for multiyear and thick first-year ice are presented in Figures 4.3(a) and 4.3(b).

(C) Weather Conditions

At each site the air temperature was recorded using the Fastemp meter and air probe. The wind speed and direction were also noted. Any other important aspects of the weather (e.g., cloudy, snowing, etc.) were also recorded.

4.4 Data Analysis Techniques

The basic equation used for the computation of σ^o is equation (10) in Section 2.2.

$$\sigma^o = W_{ot} - W_{oDt} + W_{oDL} - W_{oL} + \sigma_L - 10 \log_{10} A_{ill} + 40 \log_{10} R_t - 40 \log_{10} R_c \qquad (10)$$

The derivation of this equation was shown in Section 2.2. All the terms except A_{ill} are available directly from the data. The illuminated area A_{ill} is computed as shown in Section 2.2, using the information about incidence angle, beamwidths, and flying altitude. The exact angle of incidence was determined for each case by taking into account
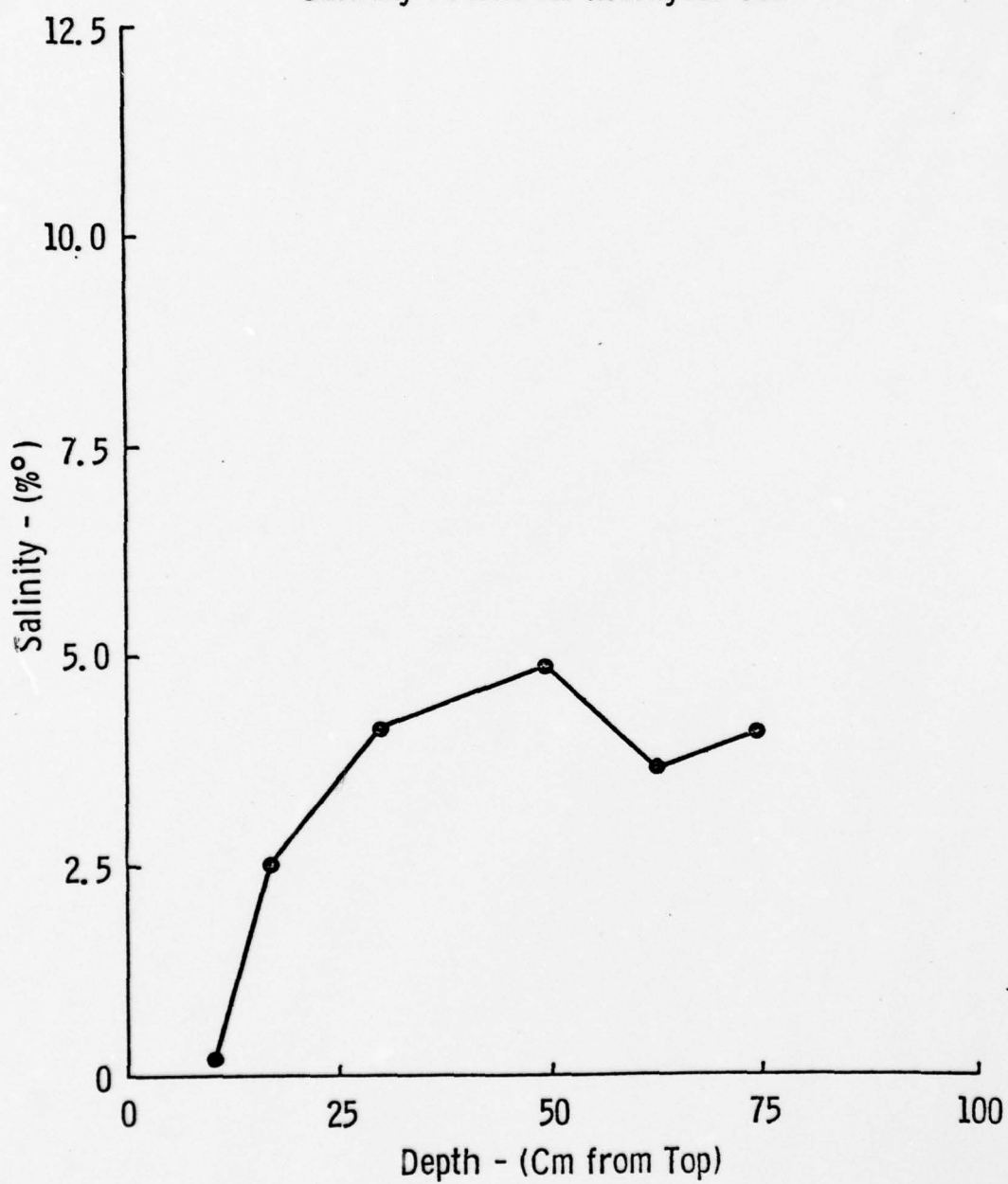
FIGURE 4.3(a)
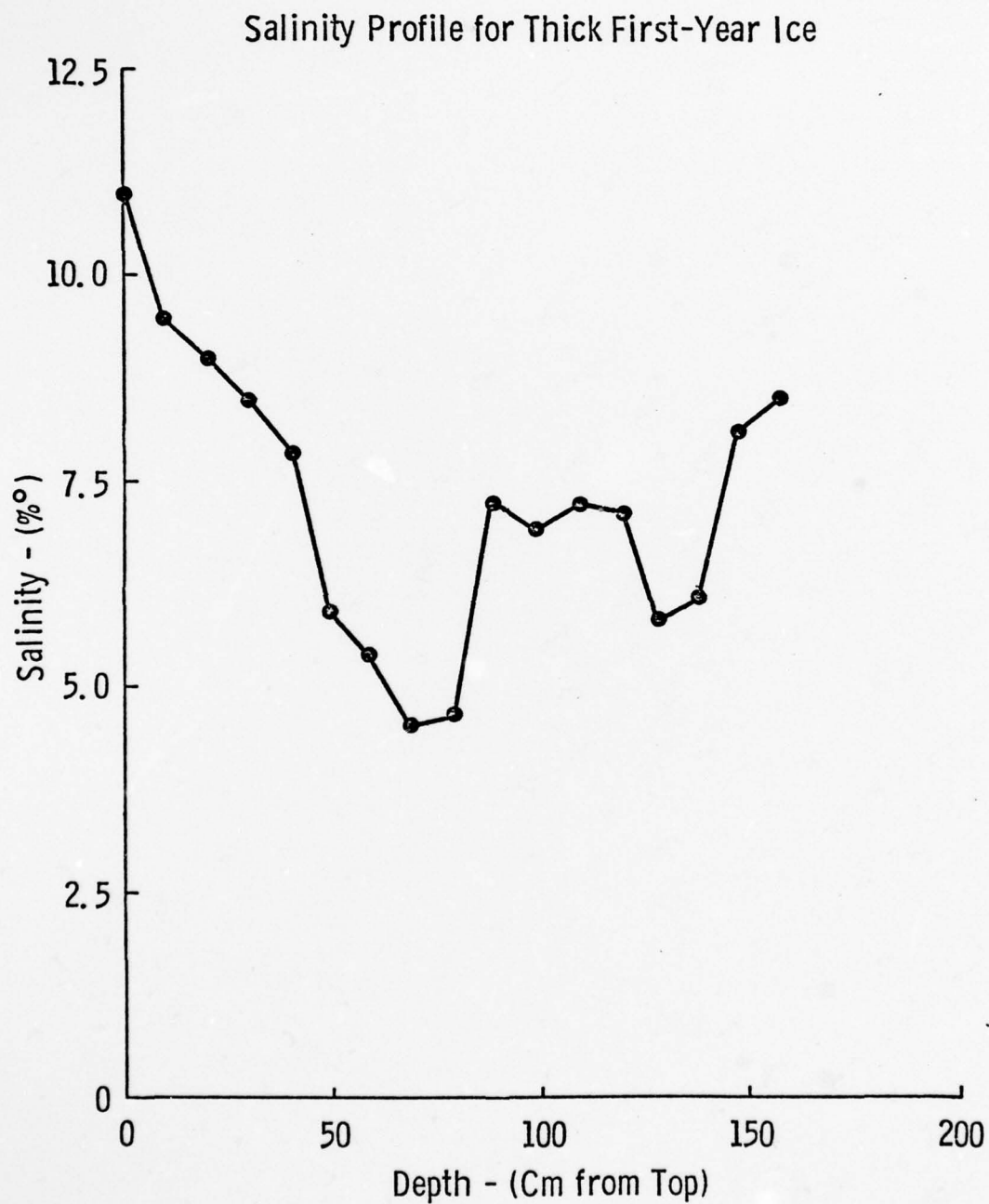
Salinity Profile for Multi-year Ice

FIGURE 4.3(b)

Salinity Profile For Thick First-Year Ice

the roll and pitch motion of the helicopter. A good estimate of this effect was obtained using a mason's level and a ruler. The actual incidence angles turned out to be 17.57°, 36.24°, and 56.12°. A listing of the main computer program generated for the computation of σ^o from the raw data is presented in Appendix C.

The range to the target, R_t, was calculated from the known incidence angle and the altitude which was assumed to be 100 feet at all times. Range to calibration, R_c, was 127.5 feet which is approximately the range to target, R_t, at the intermediate angle of incidence. The radar cross-section, σ_L, for the standard target was obtained from the manufacturers specifications and also by experimental verification (by measuring the lens backscatter and using a corner reflector for calibration).

In the calculation of the illuminated area, A_{ill}, two different sets of 3 dB beamwidths were used. One set applies to the case where the incidence angle is 60° and the other set is used for the two lower incidence angles. The reason for this is that the shift in the peaks of transmit and receive antenna patterns for the 60° incidence angle is larger than the shift for the two lower incidence angles. This was explained in detail in Section 2.4.1.

4.5 Spring 1978 'HELOSCAT' Experiment Results

In this section the results of Spring 1978 HELOSCAT experiment are presented along with a discussion. The L-band and Ku-X-Band scattering coefficient observations and discussion are presented in separate sections.

4.5.1 L-Band Scattering Coefficient Observations and Discussion. The value of the differential scattering coefficient σ^o at L-band for thick first-year ice follows the trend that one would expect. Figure 4.4

shows a curve of σ^o versus the angles of incidence for HH polarization at L-band. The values of σ^o for thick first-year ice at the various angles of incidence compare well with the corresponding values obtained for data collected with the University of Kansas Transportable Microwave Active Spectrometer (TRAMAS) during the spring of 1977 and 1978 Arctic missions. The surface-based system did not have HH polarization capability, so comparison was made with VV polarization. The σ^o-versus-incidence-angle curve for thick first-year ice with HELOSCAT system has the same trend as that with ground-based system; however, there appears to be about 3-4 dB bias, which may be due to the differences in the polarizations.

The σ^o results at L-band for multiyear ice sites do not follow a downward sloping trend as was expected. The σ^o values obtained at incidence angles of 20° and 40° are considerably lower than the 20° and 40° σ^o values obtained with the surface system. However, at the incidence angle of 60° the σ^o values obtained are comparable or only slightly lower than the 60° σ^o values obtained with the TRAMAS (see Figure 4.5). The fact that the 60° σ^o values for multiyear ice sites for the HELOSCAT data are lower than the corresponding 60° σ^o values for the ground system may be attributed to the difference in polarizations (HH and VV). The L-band σ^o values for multiyear ice sites show an upward trend when plotted against the angle of incidence; that is, the σ^o values at 40° are lower than the values at 60°, and this is contrary to what one expects from all earlier scatterometer studies. A careful review of the notes taken during the data taking procedure leads to the conclusion that the 20° and 40° multiyear-ice data are erroneous. The source of the error
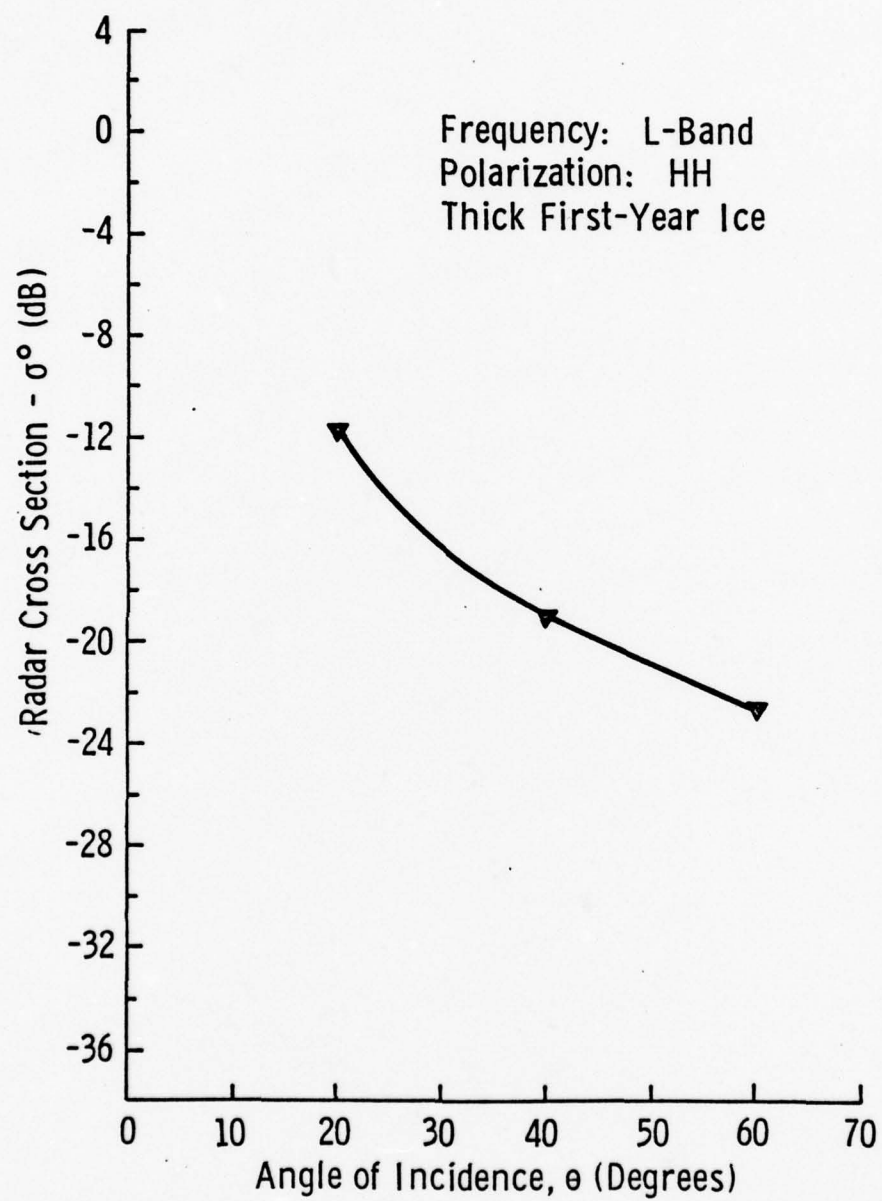
FIGURE 4.4

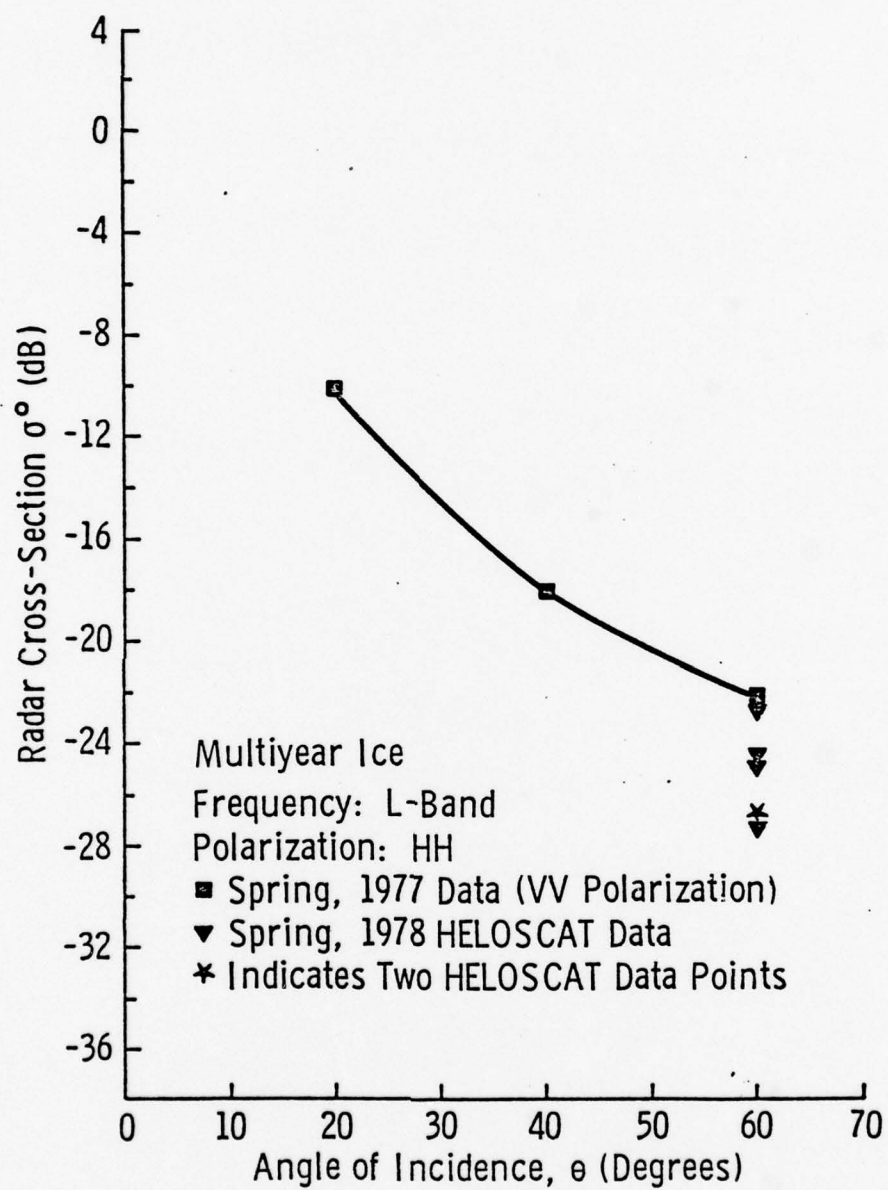Radar Cross-Section of Thick First-Year Ice at 1-2 GHz

FIGURE 4.5

Radar Cross-Section of Multiyear Ice at 1-2 GHz

is believed to have been the setting of the critical FM rate (modulating signal frequency).

As mentioned in Section 2.6, the three FM rates corresponding to the three discrete incidence angles were determined during system calibration to obtain a peak return at the corresponding range. During data taking at each discrete incidence angle, the desired FM rate is set by adjusting a potentiometer and monitoring it on a frequency counter. The FM rate is related to the range to the target by equation (13) of Section 2.3.1.

$$R = \frac{cf_{if}}{4\Delta fF_m}$$

This relationship also shows that the range R, and consequently the altitude h, must be kept reasonably constant.

Unfortunately, after a few hours of flight time the frequency counter began to malfunction. When this was realized, the FM rate was set most of the time to the 60°-incidence-angle rate and left at that; consequently, the FM rates for the 20° and 40° incidence angles were not the optimum for recording the peak returns from the targets. As a result of this, the σ^o values at 20° and 40° incidence angles are considerably lower than what one would expect. However, 60° incidence angle σ^o values appear to be in reasonable agreement with data collected by other experimenters with various radar systems.

The σ^o values for pressure-ridge ice sites also appear to have the same kind of trend as the multiyear ice sites. The values at the 20° and 40° incidence angles are unusually low; however, the 60° incidence-angle values seem to be good. The σ^o value at the incidence
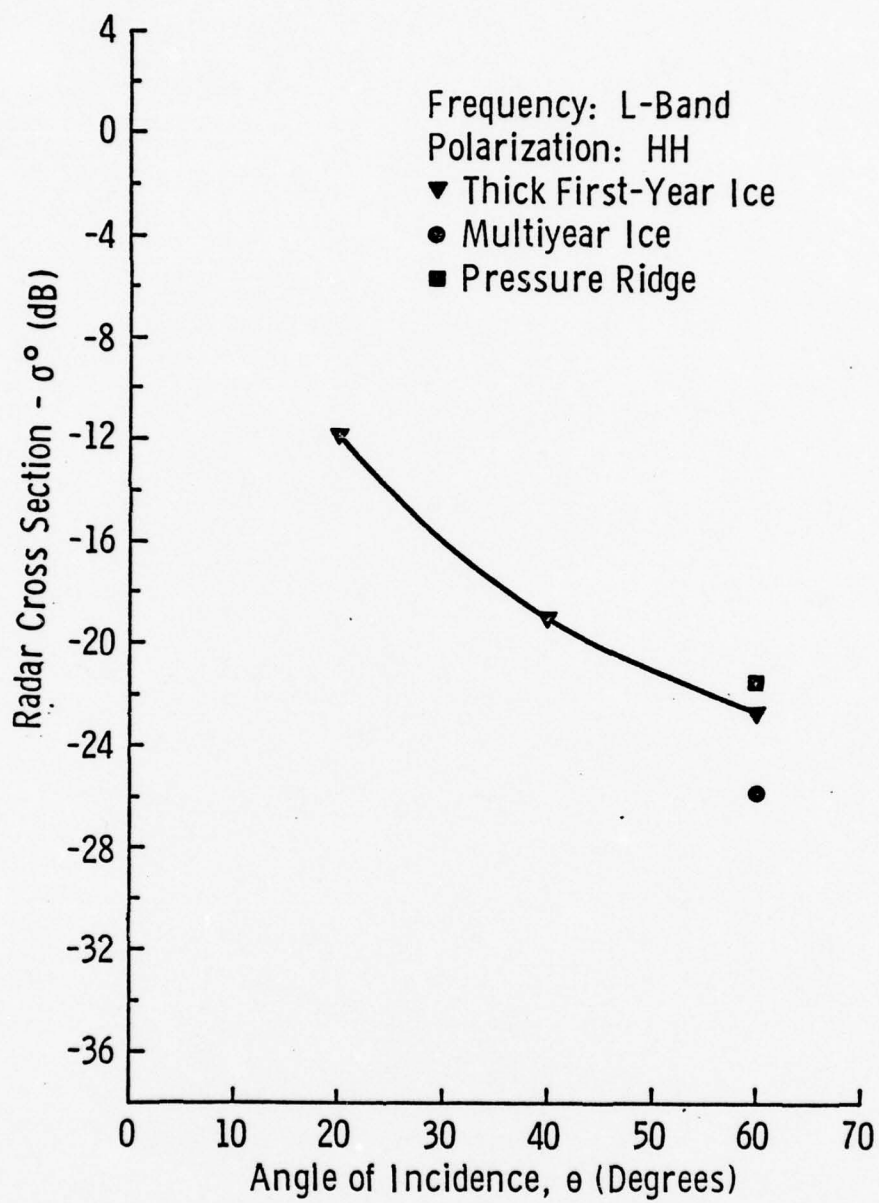
FIGURE 4.6

Radar Cross-Section of Thick First-Year Ice,
Multiyear Ice, and Pressure Ridge at 1-2 GHz

angle of 60° for pressure-ridge sites is higher than the corresponding σ^o value for multiyear ice sites.

Figure 4.6 shows the σ^o curve for thick first-year ice at L-band and the average σ^o values for the pressure-ridge sites and multiyear ice sites at the angle of incidence of 60°. It can be seen that the thick first-year ice and pressure-ridge sites have about the same σ^o value at the 60° incidence angle. The multiyear ice has about a 3 dB lower σ^o value at 60° than the thick first-year ice or pressure-ridge sites.

4.5.2 *Ku-X-Band Results and Discussion*. The scattering-coefficient-versus-incidence-angle curves for thick first-year ice at several Ku-X frequencies are presented in Figures 4.7 - 4.9. It is seen that at 9.0 GHz and 10.0 GHz the downward sloping trend exists distinctly. The curves for the higher frequencies do not behave as one would expect. There is a definite downward trend in going from the 20° incidence angle to the 40° incidence angle; however, the curves either remain constant or have a slight upward trend from 40° to 60° incidence angles. As shown earlier in Section 2.3.1, the FM rate is proportional to the altitude of the radar above the target. This means that it is critical that the range (i.e., altitude) be known accurately to ensure that the backscatter returns from the piece of ice illuminated fall within the bandpass section of the IF filter. The illuminated areas at 20° and 40° are small compared to the illuminated areas at 60° incidence angle. It is also true that the return power spectra at 20° and 40° incidence angles are narrower than the return power spectrum at the 60° incidence angle. The IF bandpass filter has a center frequency of 50 kHz and a bandwidth of 13.5 kHz. Filter response characteristics are
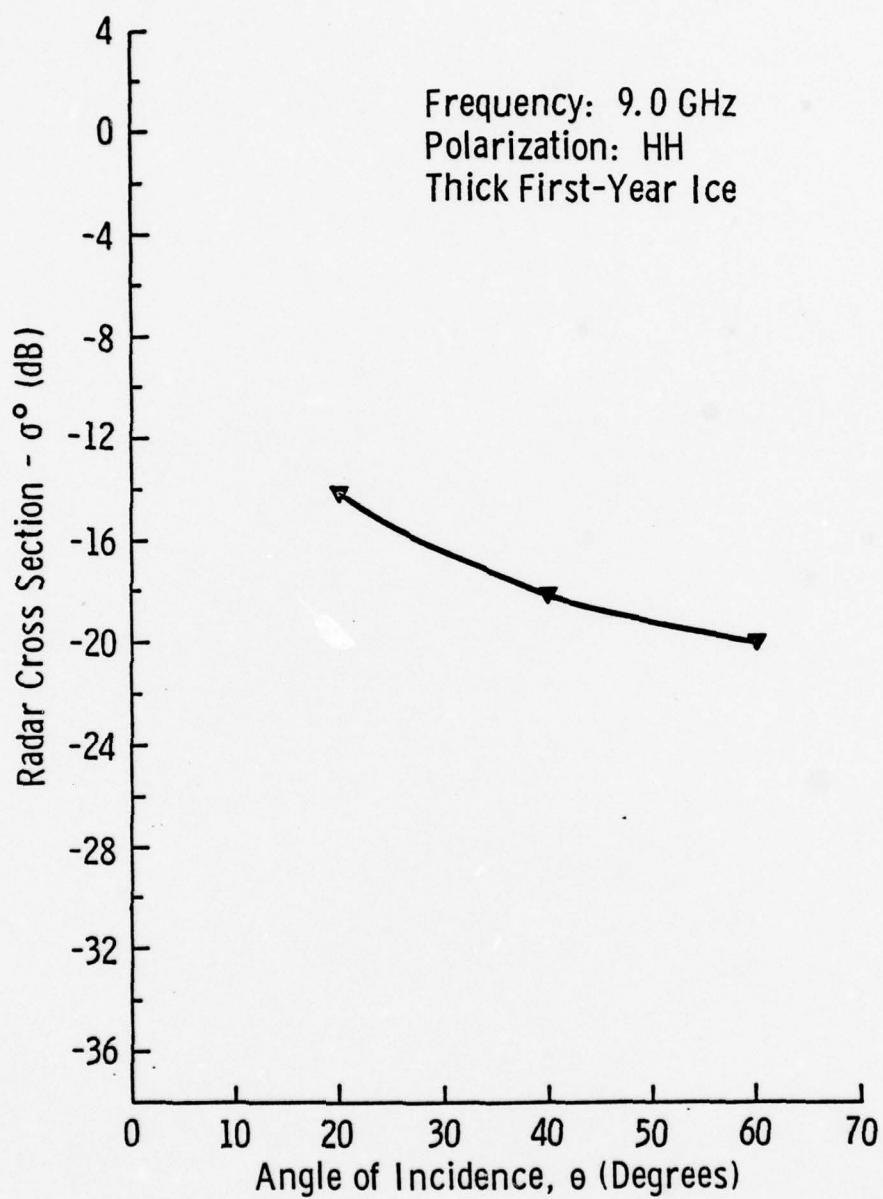
FIGURE 4.7

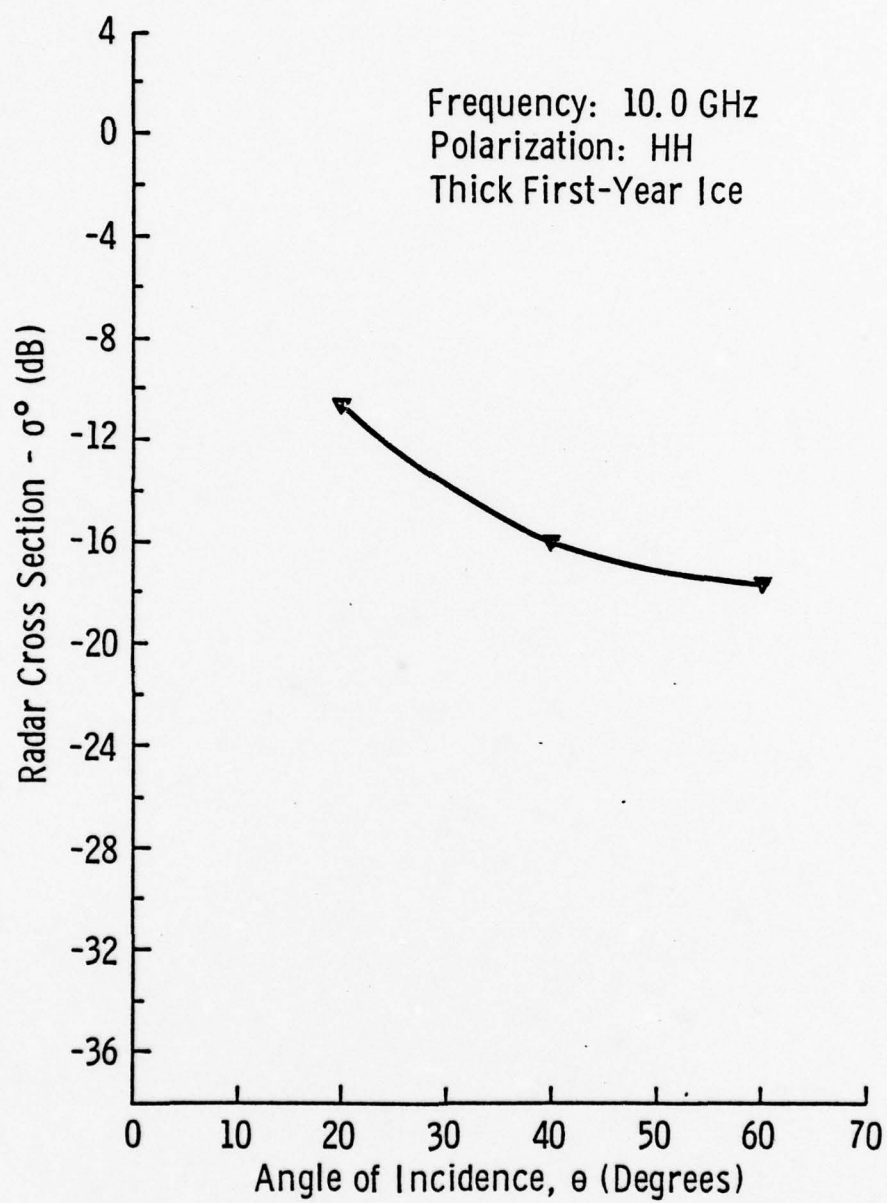Radar Cross-Section of Thick First-Year Ice at 9.0 GHz

FIGURE 4.8

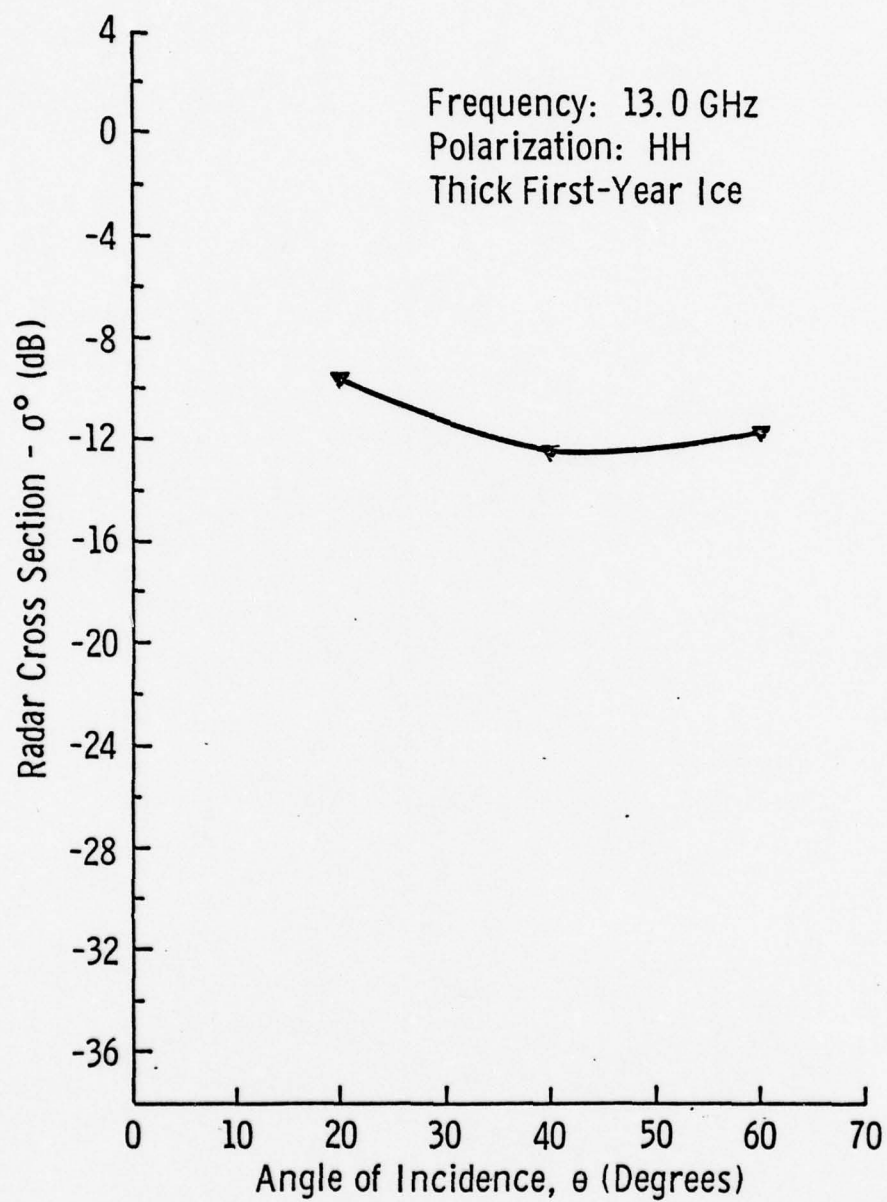Radar Cross-Section of Thick First-Year Ice at 10.0 GHz

FIGURE 4.9

Radar Cross-Section of Thick First-Year Ice at 13.0 GHz

shown in Figure 2.8. During the course of the helicopter-borne scatter-ometer experiment we had to rely upon the helicopter barometric altimeter for altitude measurements; however, it was discovered later that the accuracy of this instrument in only within 10-20 percent. Unfortunately, all the calculations of illuminated area and FM rate were based on the assumption that an altitude of 100 feet was maintained during the entire course of data taking. The uncertainty in altitude, and conse-quently range, may cause the return power spectra to fall only partially inside the passband of the IF filter, thereby not giving the correct power returned by the target. If the altitude is such that the spectrum of the returned power barely falls at the outer edge of passband of the IF filter, a more pronounced effect would occur at the 20° and 40° inci-dence angles than the 60° incidence angle. Figure 4.10(a) shows schema-tically an example of this. In this situation the 20° and 40° back-scatter return are affected more than the 60° because of the relatively wider spread of the power return at 60°, at which the area of the illum-inated cell is appreciably larger. On the other hand, if the return power spectrum is partially inside the passband of the IF filter, the error due to incorrect altitude is more significant at the higher incidence angle of 60° than the 20° and 40° incidence angles. This is shown in Figure 4.10(b). These two examples show that it is very impor-tant to maintain the proper altitude to guarantee that the return power spectra fall within the passband of the IF filter.

The Ku-X-Band data for multiyear ice sites were, unfortunately, plagued by the same problems as the L-band multiyear-ice data; namely, the malfunctioning of the frequency counter. Most measurements were

$\theta = 20^{\circ}$

$\theta = 40^{\circ}$

$\theta = 60^{\circ}$

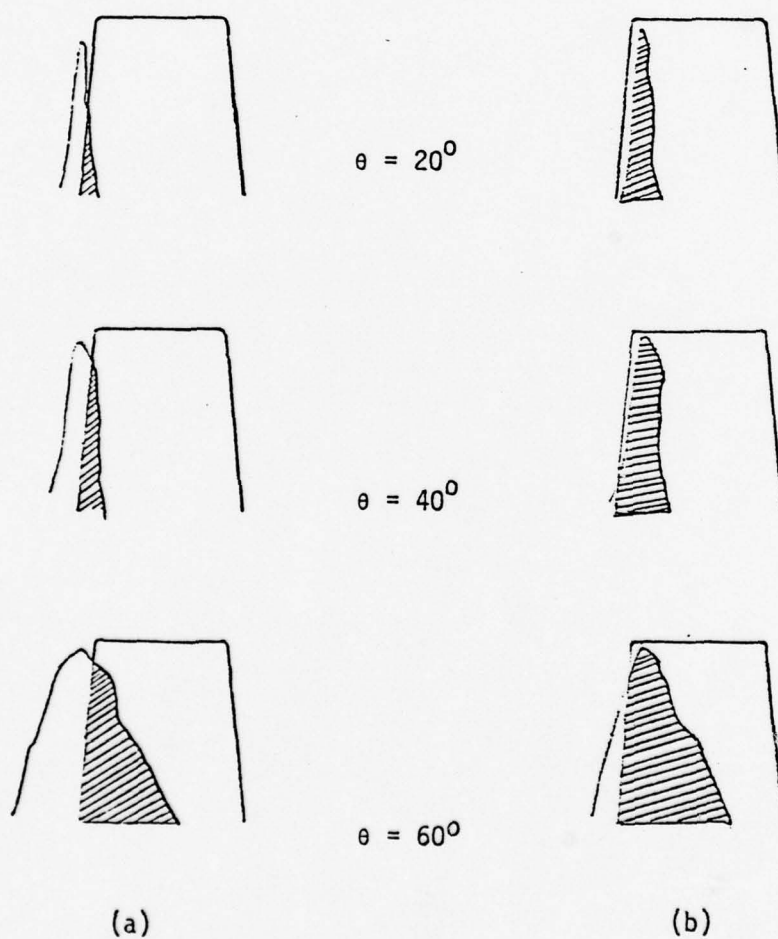(a)   (b)

Figure 4.10 Possible situations that may occur with Power Return Spectrum placement in passband of IF filter.

made at the FM rate that was determined to be optimum for the 60°
incidence angle. This apparently resulted in erroneous data for the
two lower incidence angles (20° and 40°). The σ^o values obtained at
60° agree reasonably well with previous studies shown in Figures 4.11 -
4.15. At the higher frequencies of 16 and 17 GHz, the σ^o values show
a sharp rise; however, this was traced to a sharp drop in the return
power of the lens during the calibration procedure; this is also shown
in Figure 4.16. A reason for this may be the narrower beamwidths
at the higher frequencies. The lens was originally peaked at the 9.0
GHz frequency, so at the higher frequencies the Luneberg lens is not
necessarily at the mutual center of the two beams. During future
calibrations of the HELOSCAT system the lens should be peaked at the
higher frequencies, thereby ensuring that the Luneberg lens is always
within the illuminating antenna beam.

4.5.2 Frequency Response. The scattering coefficient frequency
response curves show an almost linear and upward sloping trend, when
plotted in dB. The radar cross-section in dB of sea ice increases in a
linear fashion with increasing frequency (σ^o increases exponentially).

Figure 4.17 shows the average scattering coefficient frequency
response of multiyear and thick first-year ice. It can be seen from
the curves that the σ^o values for multiyear ice are consistently 3-4 dB
higher than the corresponding σ^o value for thick first-year ice.

From this curve it may be concluded that Ku-X-Band frequencies can
be used successfully to distinguish between different types of ice.
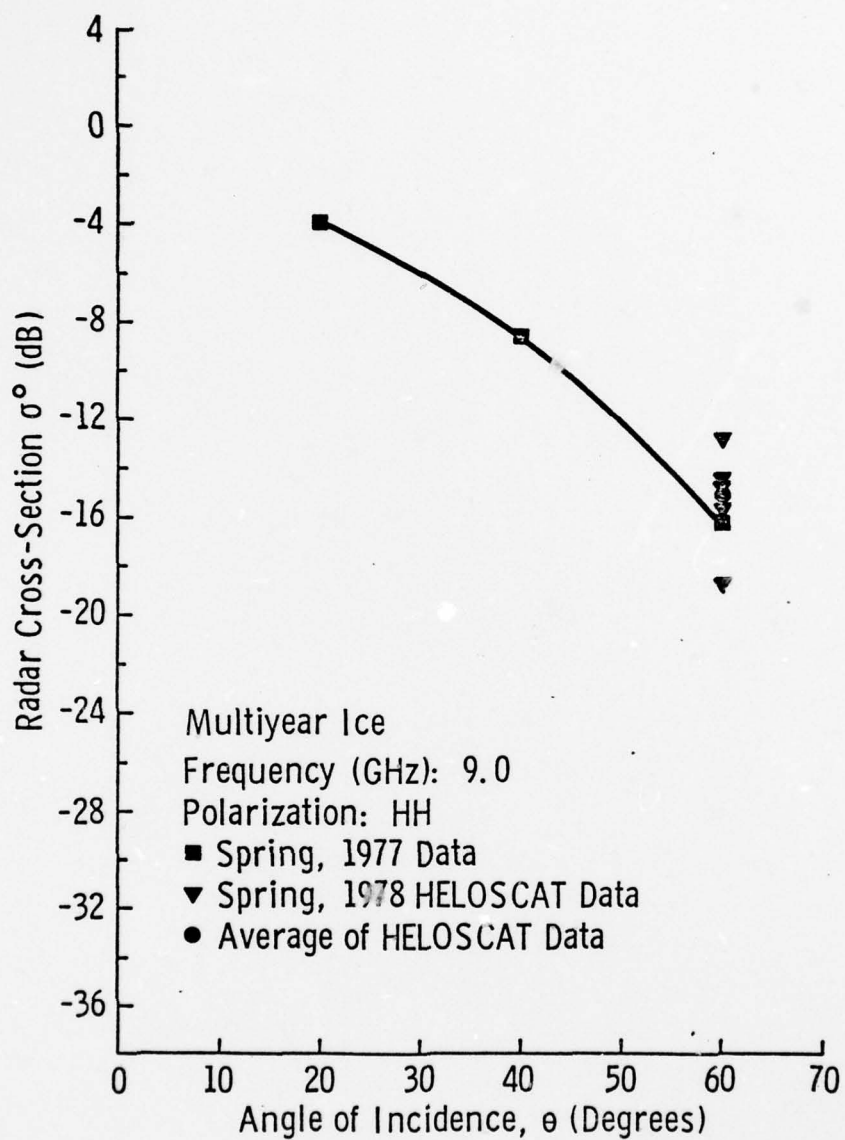
FIGURE 4.11

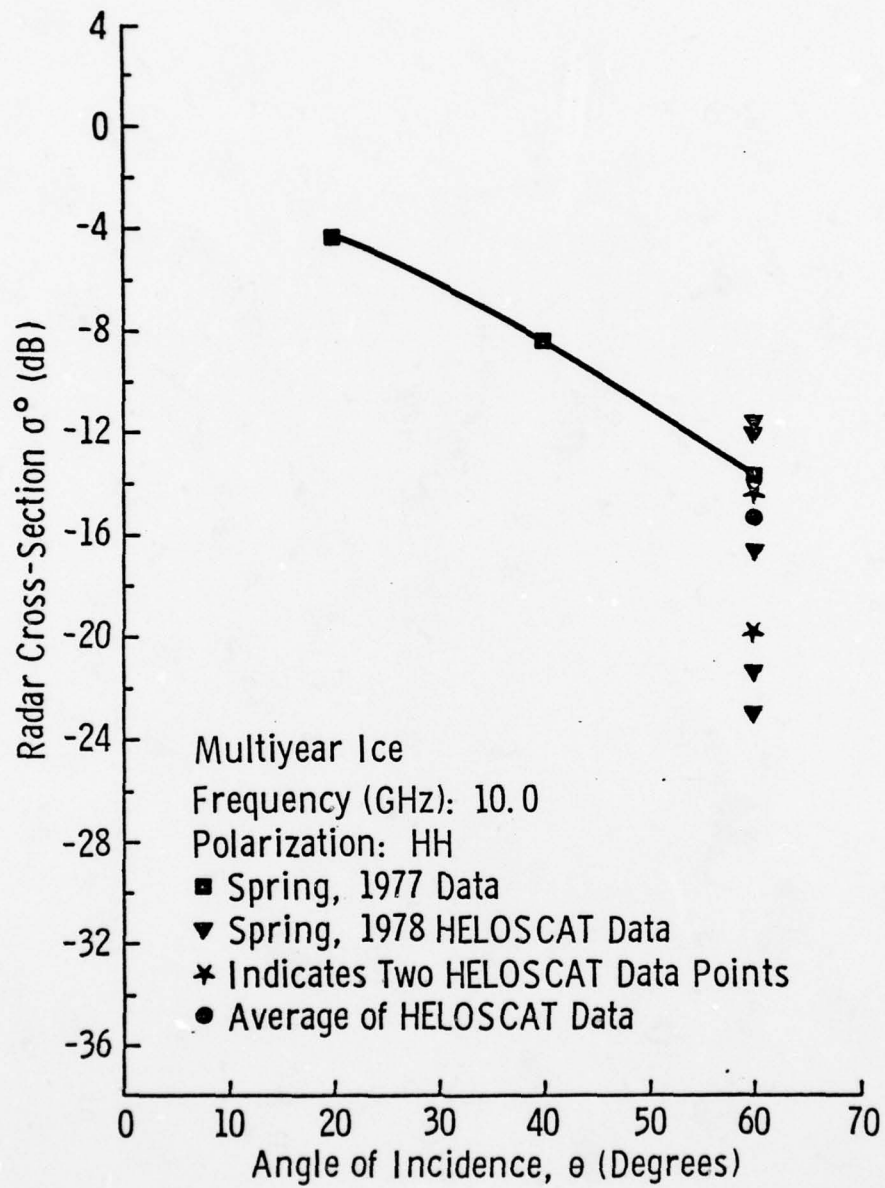Radar Cross-Section of Multiyear Ice at 9.0 GHz

FIGURE 4.12

Radar Cross-Section of Multiyear Ice at 10.0 GHz

FIGURE 4.13

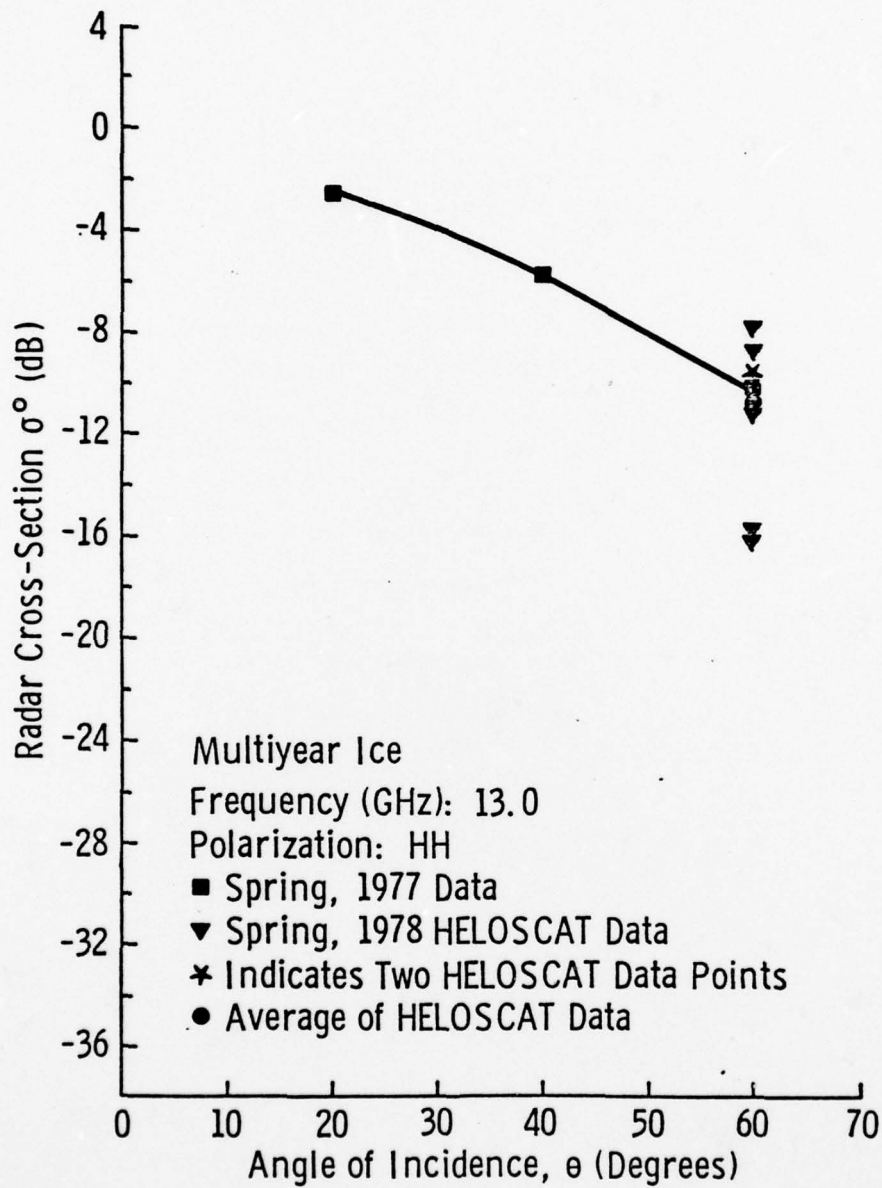Radar Cross-Section of Multiyear Ice at 11.0 GHz

FIGURE 4.14

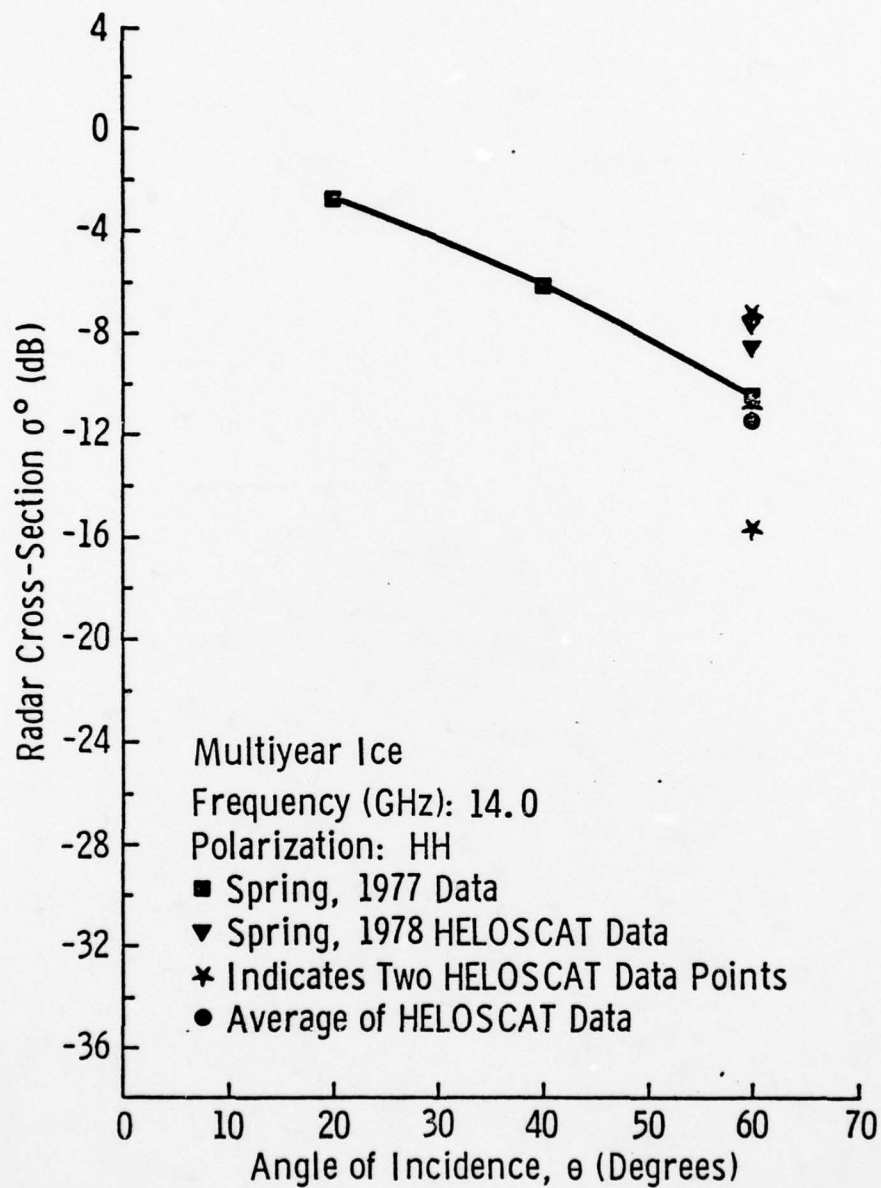Radar Cross-Section of Multiyear Ice at 13.0 GHz

FIGURE 4.15
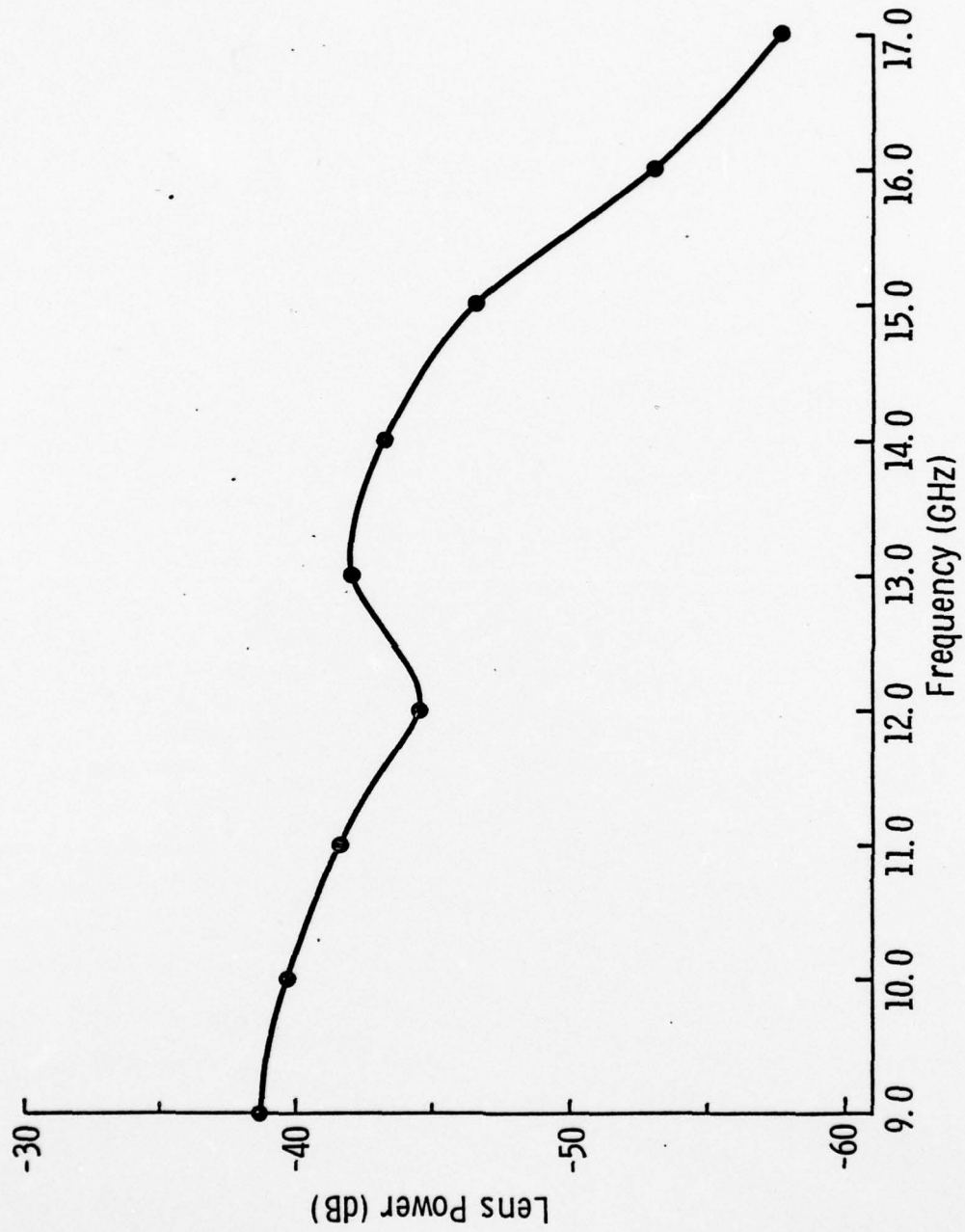
Radar Cross-Section of Multiyear Ice at 14.0 GHz

FIGURE 4.16
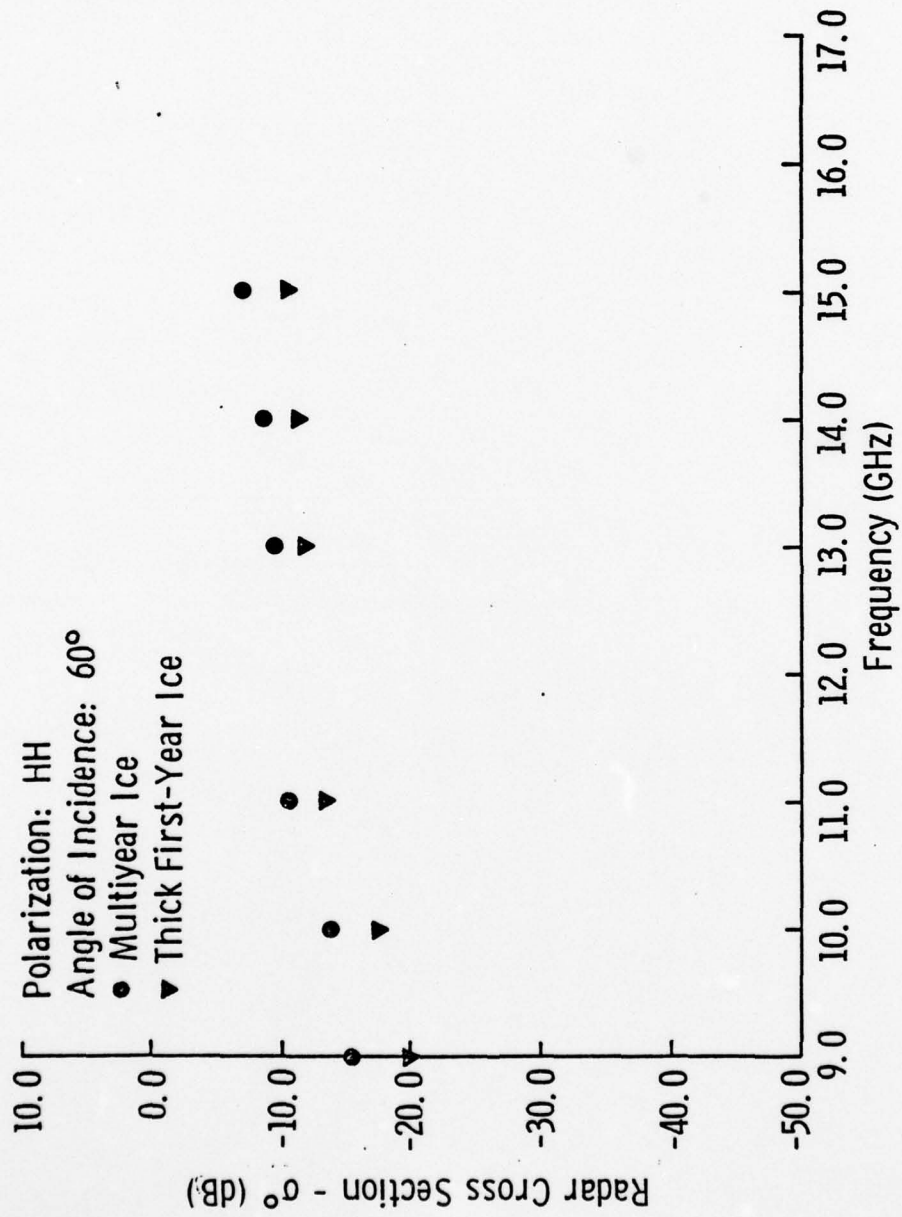
Power Returned by the Luneberg Lens versus Frequency

Polarization: HH
Angle of Incidence: 60°
● Multiyear Ice
▼ Thick First-Year Ice

Radar Cross Section - σ° (dB)

10.0
0.0
-10.0
-20.0
-30.0
-40.0
-50.0

9.0   10.0   11.0   12.0   13.0   14.0   15.0   16.0   17.0

Frequency (GHz)

FIGURE 4.17

Radar Cross-Section Frequency Response of Multiyear and Thick First-Year Ice

5.0 PRELIMINARY RESULTS OF THE SPRING 1979 HELOSCAT EXPERIMENT

In this chapter the University of Kansas spring 1979 HELOSCAT experiment is described briefly, along with the scattering coefficient observations and discussion for two thick first-year ice sites.

5.1 Brief Experiment Description

A part of the spring 1979 SURSAT [21] experiment consisted of making backscatter measurements of sea ice and lake ice using the HELOSCAT system. This experiment was conducted in the Northwest Territories of Canada from a base at Tuktoyaktuk. Backscatter data were collected with the HELOSCAT system operating over the frequency range 8-18 GHz with HH-polarization.

Unlike the spring 1978 HELOSCAT experiment, most of the back-scatter data during this experiment were obtained with the helicopter (Bell Model 205) flying at an altitude of 50 feet. It was felt that flying at an altitude of 50 feet rather than 100 feet would eliminate any sensitivity problems that may exist. During the entire course of data-taking the helicopter altitude was monitored by a radar altimeter, and recorded for data analysis. Before any backscatter data were printed on tape, the return was peaked by adjusting the FM rate. The FM rate that gave the peak return was also noted for each data set. Surface truth was also collected at a couple of sites.

5.2 Scattering Coefficient Computation

The general method adopted for the computation of σ^o from the data (spring 1979) was slightly different than the method adopted for the spring 1978 HELOSCAT experiment. Unlike the spring 1978 σ^o

computations where the altitude was always assumed 100 feet and where the backscatter returns were not peaked by adjusting the FM rates, this time the exact altitude recorded for the particular data set was used; and, furthermore, all the backscatter returns were peaked during data-taking. Adjustment of the FM rate during the data-taking process guarantees that the return power spectrum always lies within the pass-band of the IF-filter. A feedback loop is being implemented by the manual tweaking of the FM rate potentiometer. The hardware is presently being modified to include a phase-locked loop tracking circuit to ensure that the return power spectrum always lies within the pass-band of the IF-filter.

5.3 Scattering Coefficient Observations and Discussion

The incidence angle versus scattering coefficient curves for the two thick first-year-ice sites analyzed are presented in Figure 5.1 through 5.6. Curves for the average scattering coefficient versus incidence angles at 9.0 GHz, 13.0 GHz, and 17.0 GHz are shown for the two sites. All the curves have a generally downward sloping trend, as one would expect from earlier studies.

In contrast to the spring 1978 HELOSCAT experiment, the curves follow a downward trend even at the higher frequencies. The general level of the curves is 3-4 dB lower than the σ^o curve levels for the spring 1977 and 1978 Arctic experiments. This difference in levels may be attributed to the fact that the temperatures during the spring 1979 experiment were at least 25° C lower than the temperatures under which the spring 1977 and 1978 data were collected.
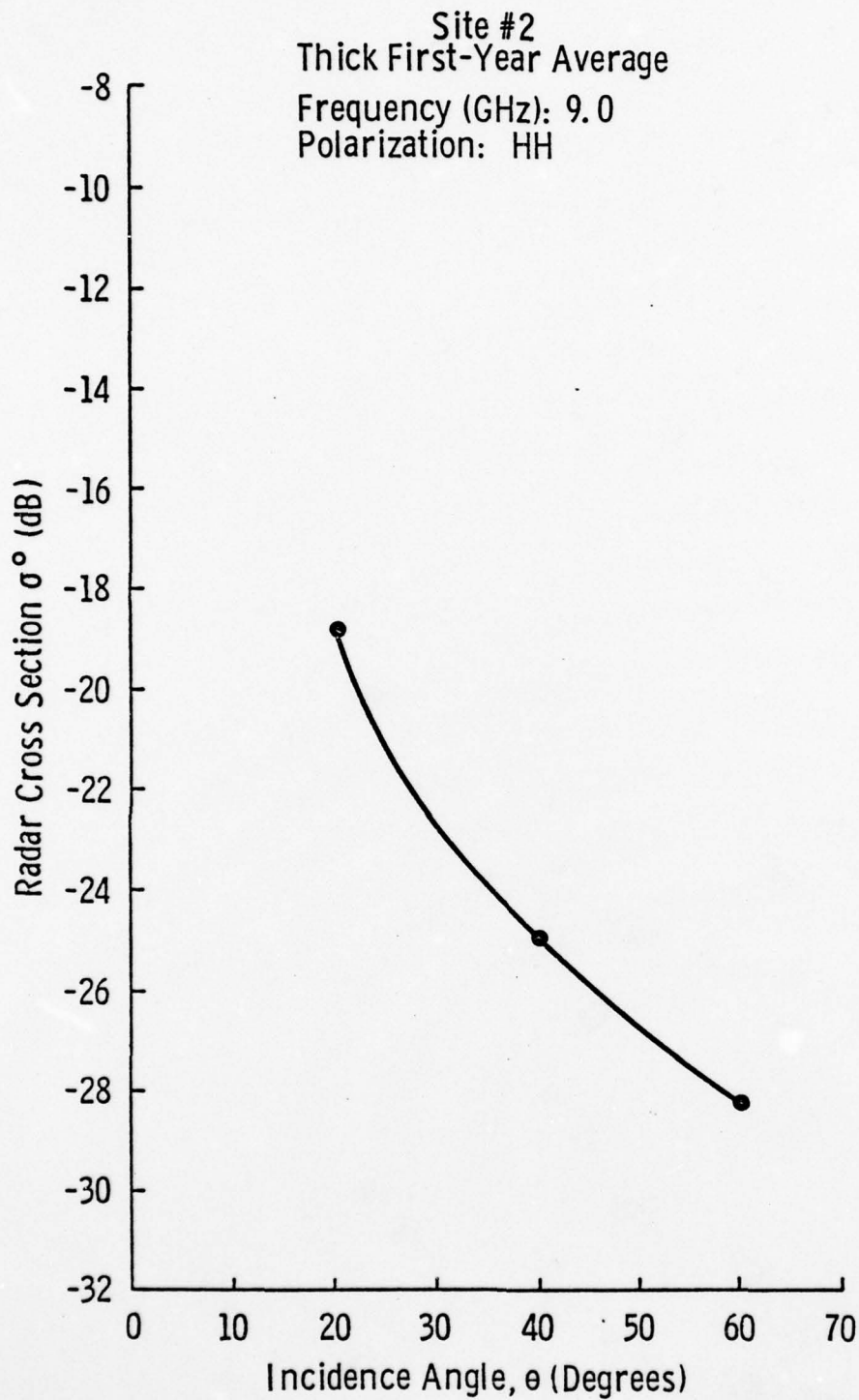
FIGURE 5.1

Radar Cross-Section of Thick First-Year Ice at 9.0 GHz
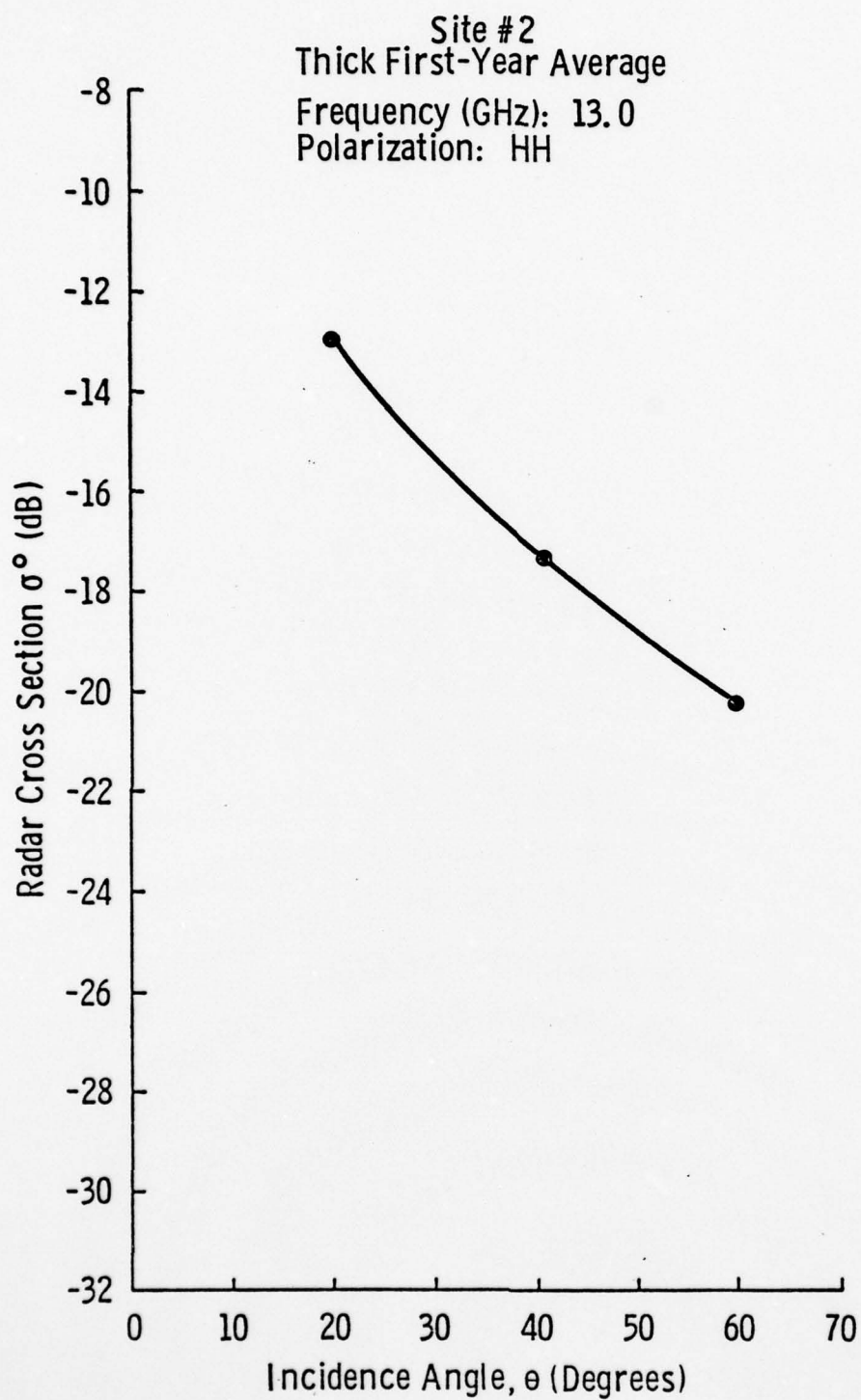
FIGURE 5.2

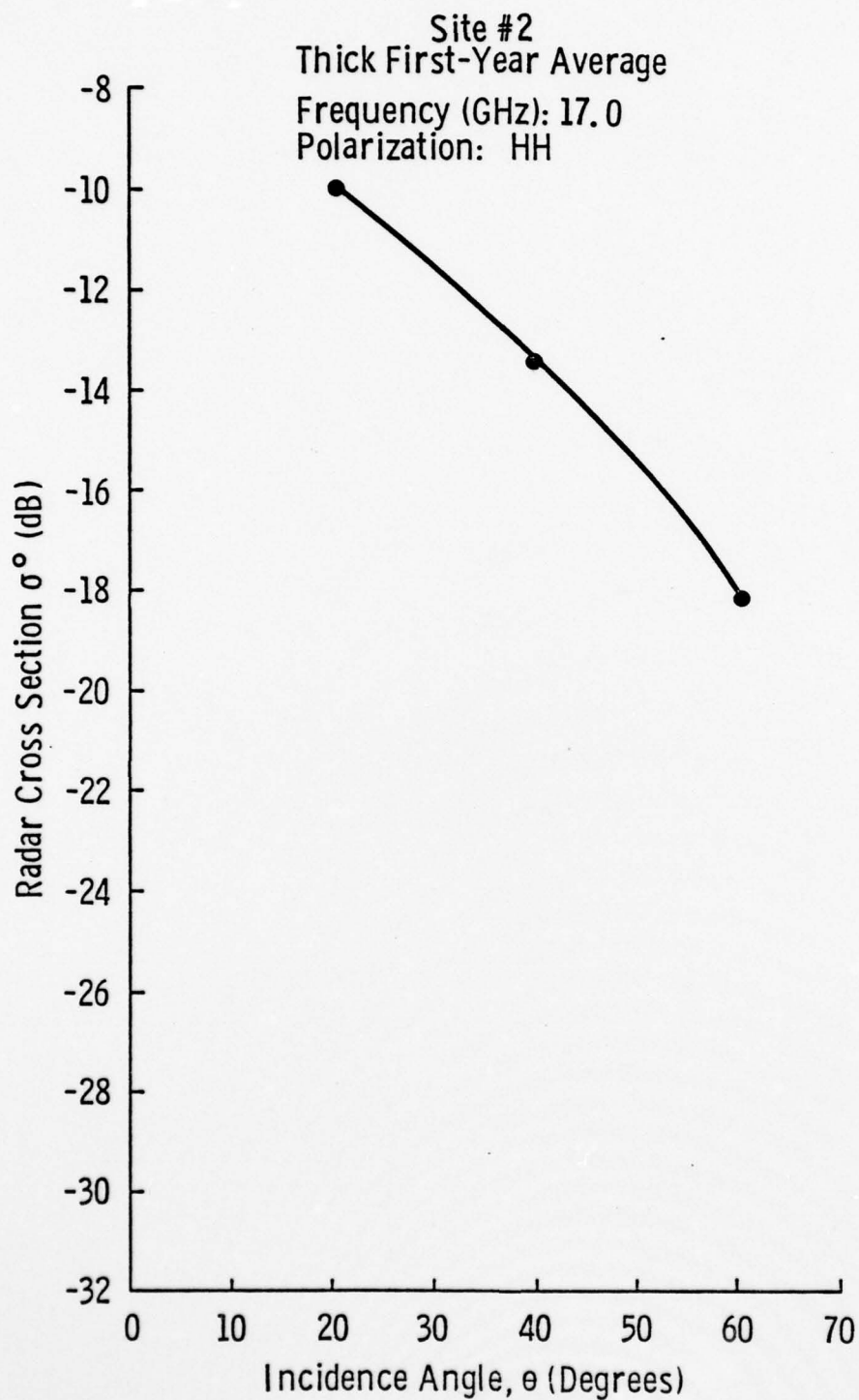Radar Cross-Section of Thick First-Year Ice at 13.0 GHz

FIGURE 5.3

Radar Cross-Section of Thick First-Year Ice at 17.0 GHz

The fact that the spring 1979 HELOSCAT experiment results agree
fairly well with previous results shows that the HELOSCAT system can be
used successfully to collect backscatter data. It also verifies that
the erroneous data in part of the spring 1978 experiment were, in fact,
due to the malfunctioning frequency counter with the result that the
backscatter returns from the ice were not peaked.

Site #3
Thick First-Year Average
Frequency (GHz): 9.0
Polarization: HH
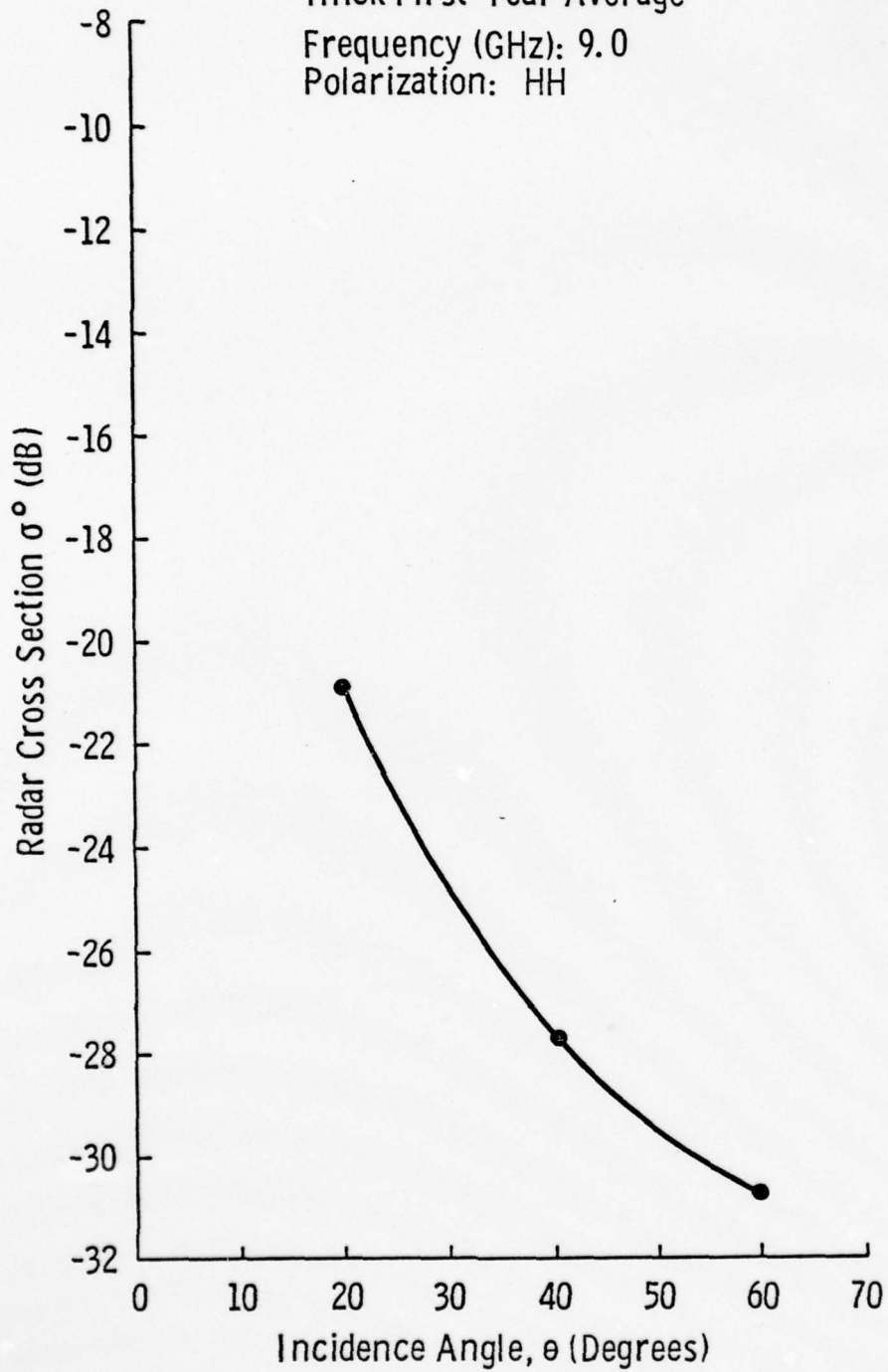
FIGURE 5.4

Radar Cross-Section of Thick First-Year Ice at 9.0 GHz
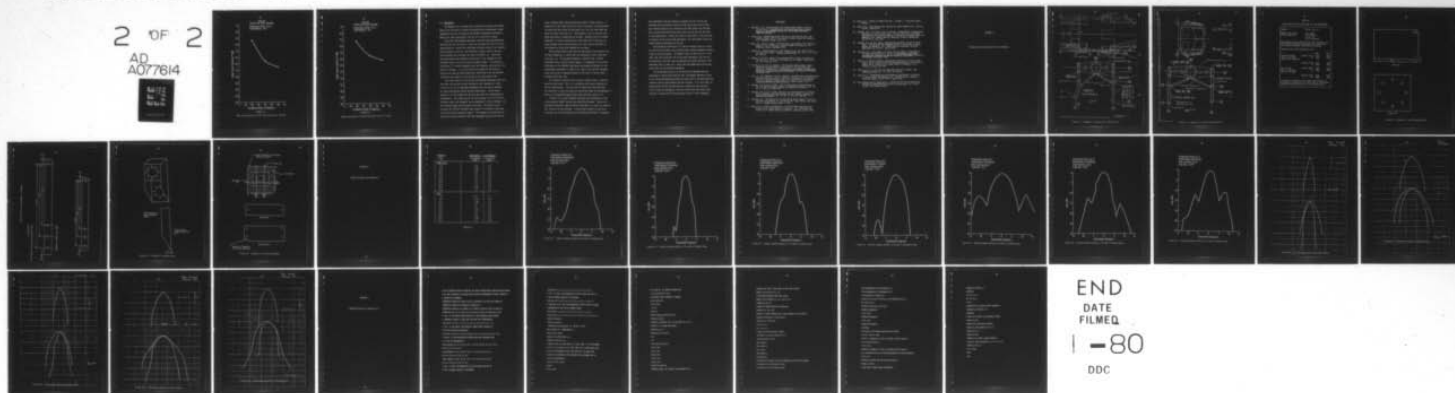
Site #3
Thick First-Year Average
Frequency (GHz): 13.0
Polarization: HH
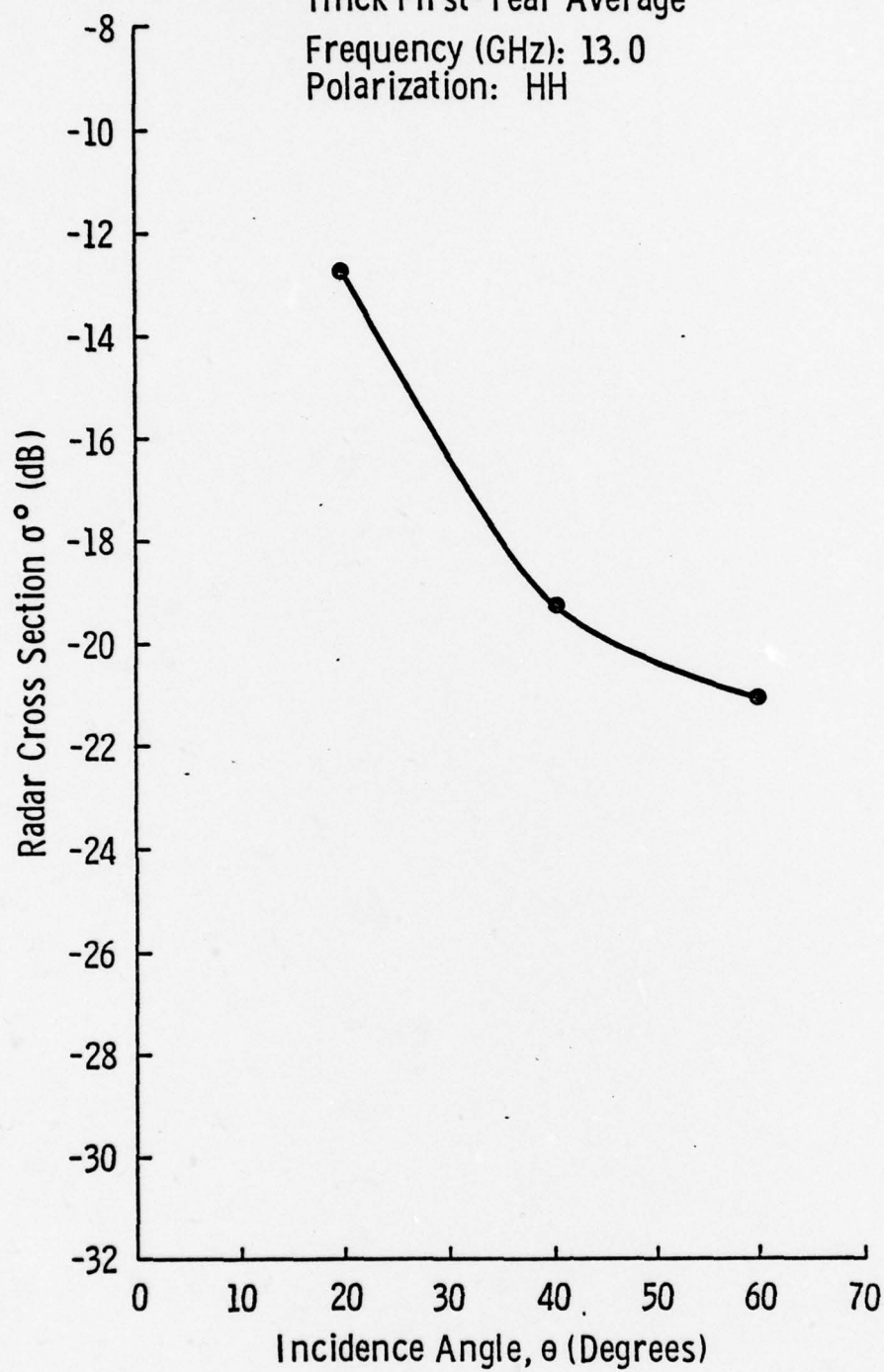
FIGURE 5.5

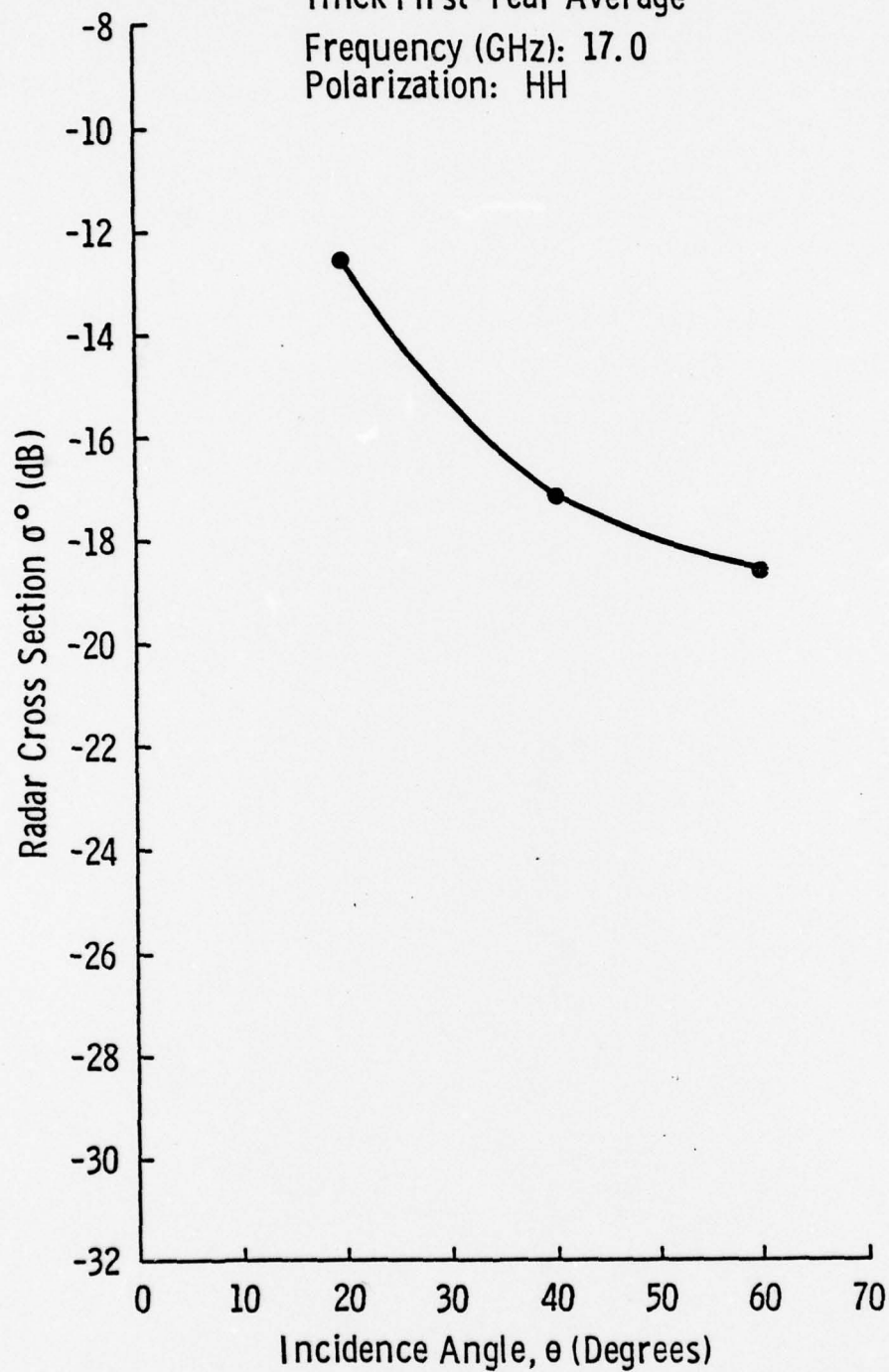Radar Cross-Section of Thick First-Year Ice at 13.0 GHz

FIGURE 5.6

Radar Cross-Section of Thick First-Year Ice at 17.0 GHz

6.0 CONCLUSION

The objective of this paper was to describe the design and development of the University of Kansas helicopter-borne scatterometer system (HELOSCAT), and also to describe the HELOSCAT experiments performed to measure the radar backscatter from sea ice in the Arctic regions.

The spring 1978 HELOSCAT experiment involved obtaining backscatter data from sea ice at L-band (1-2 GHz) and Ku-X-band (8.0-18.0 GHz) with HH-polarization. During this experiment different kinds of ice, ranging from multiyear to thin ice, were observed; however, most of the data were collected over multiyear and thick first-year ice. These data were analyzed and the scattering coefficient σ^o was computed for the different types of ice at the three incidence angles. The scattering coefficient σ^o is mainly dependent upon the frequency, polarization, and angle of incidence. It is not possible to comment on the effect of polarization upon the radar backscatter coefficient since the HELOSCAT system was only capable of taking data at one polarization (HH).

The L-band results of the spring 1978 HELOSCAT experiment show that the radar cross-section values obtained at this frequency for thick first-year ice are in reasonable agreement with the results obtained by other experimenters during previous experiments. The HH return obtained is on the average 2-3 dB lower than that for surface-based VV measurements. The L-band results for the multiyear ice at 20° and 40° incidence angles are extremely low and apparently in error; however, the 60°-incidence-angle results appear to be good. The reason for the erroneous 20° and 40° incidence angle results is believed to have been the malfunctioning frequency counter. The problem of not being able to maintain an exact altitude of 100 feet compounded the error at the two

lower incidence angles where maintaining height is more critical. A comparison of the L-band results for thick first-year ice and multiyear ice shows that the values for multiyear ice at 60° are lower than the value for thick first-year ice. Unfortunately, this is the only incidence angle where a comparison can be made. Judging from this limited comparison, it may be concluded for L-band that thick first-year ice gives stronger returns than multiyear ica; and it may be possible to discriminate on these bases between the two types.

The Ku-X-band results show that the backscatter from multiyear ice at these frequencies is higher than the backscatter return from thick first-year ice. The average difference is about 3-4 dB. Earlier experiments show a similar trend; however, in comparison to the 3-4 dB difference for the HELOSCAT experiment the average difference for the ground-based experiments is about 6 dB. Again, only the 60° incidence angle results may be compared because of the error in the two lower incidence angle data sets.

The frequency response curves follow an almost linear (in dB) and upward sloping trend. This is in conformity with results obtained by earlier experimenters. The thin-ice and rubble data collected were not sufficient to justify making any conclusions about the scatterometer's ability to distinguish between these types and other types of ice.

In March 1979 another HELOSCAT experiment was performed as a part of the Canadian SURSAT (Surveillance Satellite) program. During this experiment backscatter data from thick first-year ice, lake ice, brackish ice, and thin ice was obtained. A preliminary analysis of the thick first-year ice site was made and the scattering coefficient σ^o computed.

The experimental and data analysis procedure for this mission was different from the earlier mission in that during this mission data were collected flying at an altitude of 50 feet rather than 100 feet. Also, the altitude and FM rate were noted for each data set and used in the computations. During the course of data taking in this mission, in contrast to the spring-1978 experiments, the backscatter return was always peaked by adjusting the FM rate.

The scattering coefficient (σ^o)-versus-incidence angle (θ) curves for the thick first-year sites analyzed show a general downward sloping trend as one would expect. The general level of the curves is 3-4 dB lower than the spring-1977 and spring-1978 experiments, but this can be explained by the fact that the temperatures during the March, 1979, experiment were at least 25° C lower than the temperatures during the spring-1977 and spring-1978 experiments.

The preliminary analysis of the spring-1979 HELOSCAT data was undertaken to confirm the suspicion that the anomaly observed in part of the spring-1978-experiment data was really due to the malfunctioning frequency counter and erroneous FM rate settings. It is felt that, to guarantee the correct FM rate setting, a phase-lock loop tracking circuit should be included as this will ensure that the return power spectrum is always within the pass-band of the IF filter (bandpass).

REFERENCES

1. Anderson, V.H., "High Altitude Side-Looking Radar Images of Sea Ice in the Arctic," Proceedings of the Fourth Symposium on Remote Sensing of Environment, University of Michigan, Ann Arbor, 1966, pp. 845-857.

2. Biggs, A.W., "Volume Scattering from Sea Ice and Glacier Snow," RSL Technical Report 137-2, University of Kansas Center for Research, Inc., Lawrence, Kansas, July 1970.

3. Bush, T.F. and F.T. Ulaby, "8-18 GHz Radar Spectrometer," RSL Technical Report 177-43, University of Kansas Center for Research, Inc., Lawrence, Kansas, September 1973.

4. Dunbar, M., "Interpretation of SLAR Imagery of Sea Ice, Nares Strait, and the Arctic Ocean," Journal of Glaciology, Vol. 15, No. 73, 1975, pp. 193-213.

5. Dunbar, M. and W.F. Weeks, "The Interpretation of Young Ice Forms in the Gulf of St. Lawrence Using Radar and IR Imagery," DREO Report No. 711, 1975, pp. 1-41.

6. Glushkov, V.M. and V.B. Komarov, "Side-Looking Imaging Radar System TOROS and Its Application to the Study of Ice Conditions and Geological Explorations," Proceedings of the Seventh International Symposium on Remote Sensing of Environment, University of Michigan, Ann Arbor, 1971.

7. Gray, L., R.O. Ramseier, and W.J. Campbell, "Scatterometer and SLAR Results Obtained Over Arctic Sea Ice and Their Relevance to the Problems of Arctic Ice Reconnaissance," Paper to be presented at the Fourth Canadian Symposium on Remote Sensing, Quebec, Canada, 1977.

8. Johnson, J.D. and L.D. Farmer, "Use of Side-Looking Airborne Radar for Sea Ice Identification," Journal of Geophysical Research, Vol. 76, No. 9, 1971, pp. 2138-2155.

9. Ketchum, R.D. and S.G. Tooma, "Analysis and Interpretation of Airborne Multi-frequency Side-Looking Radar Sea Ice Imagery," Journal of Geophysical Research, Vol. 78, No. 3, 1973, pp. 520-538.

10. Ketchum, R.D., "An Evaluation of Side-Looking Radar Imagery of Sea Ice Features and Condition in the Lincoln Sea, Nares Strait, and Baffin Bay <U>," NORDA Technical Note 7, 1977.

11. Moore, R.K., "Radar Scatterometery - An Active Remote Sensing Tool," University of Kansas Center for Research, Inc., CRES Technical Report 61-11, Remote Sensing Laboratory, Lawrence, Kansas, 1966.

12. Moore, R.K., "Manual of Remote Sensing" - Chapter 9 - Microwave Remote Sensors.

13. Moore, R.K., 1970, Ground Echo; Chapter 25, Radar Handbook (M.I. Skolnik, editor), McGraw-Hill.

14. Onstott, R.G., J.S. Patel, and C.V. Delker, "Investigation of Backscatter Properties of Sea Ice with Radar - Spring 1978 Arctic Experiment Description and Preliminary Results," University of Kansas Center for Research, Inc., Remote Sensing Laboratory Technical Memorandum, RSL TM 331-3, July 1978.

15. Onstott, R.G. and W.F. Weeks, "Backscatter Properties of Sea Ice with Radar - Ground-Based Scatterometer Results," University of Kansas Center for Research, Inc., Remote Sensing Laboratory Technical Memorandum RSL TM 331-2, August 1978.

16. Parashar, S.K., A.W. Biggs, A.K. Fung, and R.K. Moore, "Investigation of Radar Discrimination of Sea Ice," Proceedings of the Ninth International Symposium on Remote Sensing of Environment, University of Michigan, Ann Arbor, 1974.

17. Patel, J.S. and R.G. Onstott, "Backscatter Properties of Sea Ice with Radar: Spring 1978 Heli-borne Scatterometer Results," RSL Technical Report 331-9, University of Kansas Center for Research, Inc., Lawrence, Kansas, May 1979.

18. Rouse, J.W. (Jr.), "Arctic Ice Type Identification by Radar," Proceedings of IEEE, Vol. 57, 1969, pp. 605-614.

19. Waite, W.P., "Broad-Spectrum Electromagnetic Backscatter," University of Kansas Center for Research, Inc., Remote Sensing Laboratory Technical Report, RSL-TR 133-17, August 1970.

20. World Meteorological Organization - Commission for Marine Meteorology Workshop on Remote Sensing of Sea Ice, Washington, D.C., 16-20 October 1978, Summary Report.

APPENDIX A

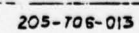Antenna Mount Structure Details and Drawings
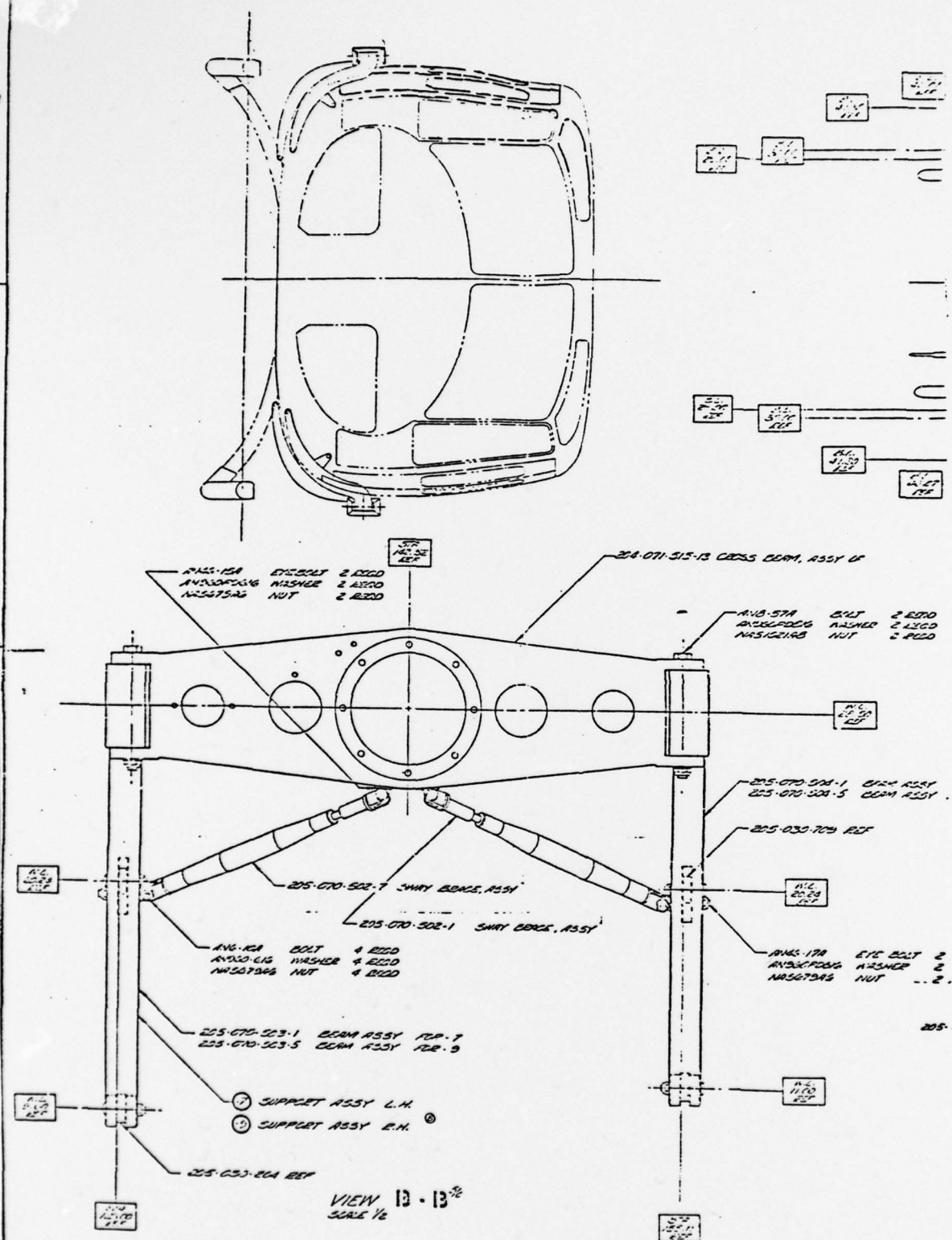
Figure A-1. Schematic of forward Bell auxiliary kit.

Figure A-2. Schematic of aft Bell auxiliary kit.

TABLE A-1

LOAD LIMITS FOR BELL AUXILIARY KITS AND HARDPOINTS

Support   750 lb. max. wt.

Design limit loads   4 G's down
Acting separately   4 G's forward
                                  2.0 G's up
                                  1.5 G's outboard

The hardpoint mounts have various load allowables and the following information provides the forward and aft fitting structural definition by location.

Hardpoint Limit Load Allowables (lbs.)

			Upper	Lower
Forward Fittings (set of 4 on each side of the fuselage)	Station 63	PZ	3400	1900
		PY	3800	1800
	Station 84	PZ	2700	1200
		PY	3400	800
Aft Fittings (set of 4 on each side of fuselage)	Station 129	PZ	2700	1200
		PY	2400	1100
	Station 155	PZ	3100	1600
		PY	2900	1400

In addition to the PZ and PY loads, each fitting is designed to a forward or aft limit load of 1700 pounds applied along the centerline of the mounting hole.
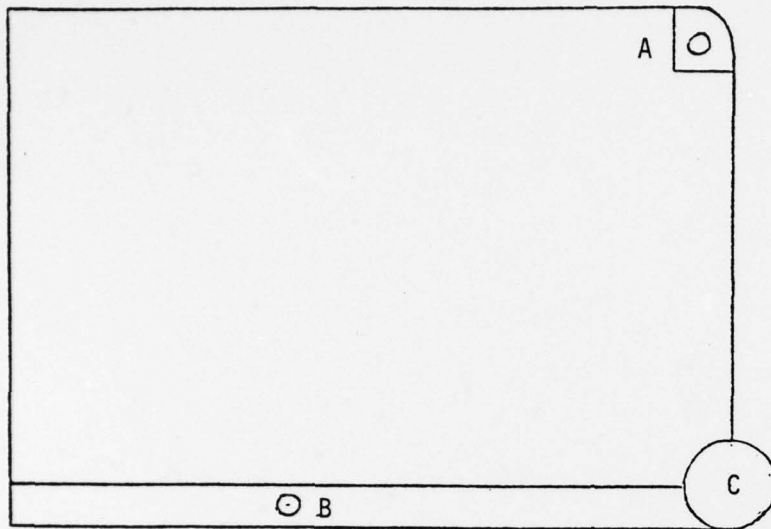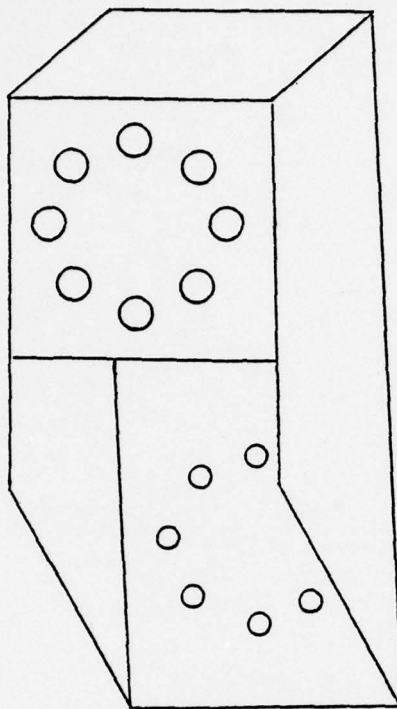
Side view
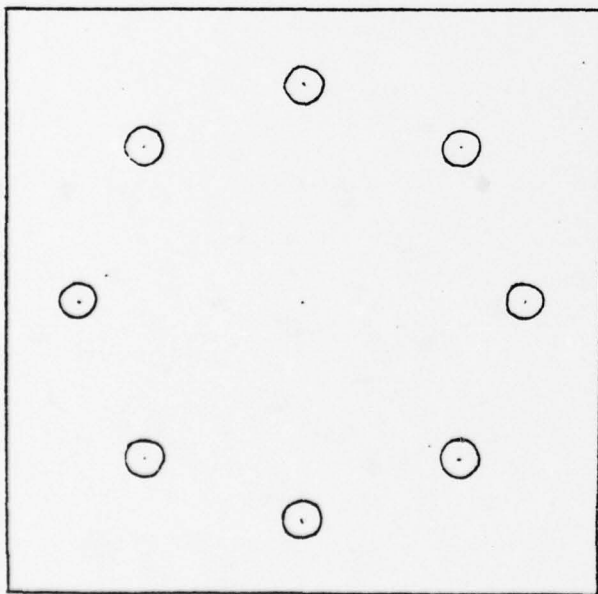
Back view
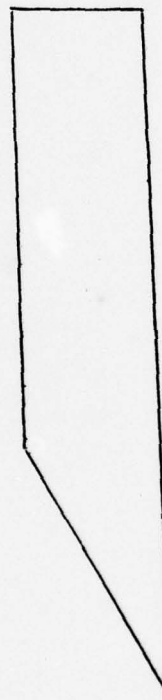
Figure A-3. Schematic of angle changing block.
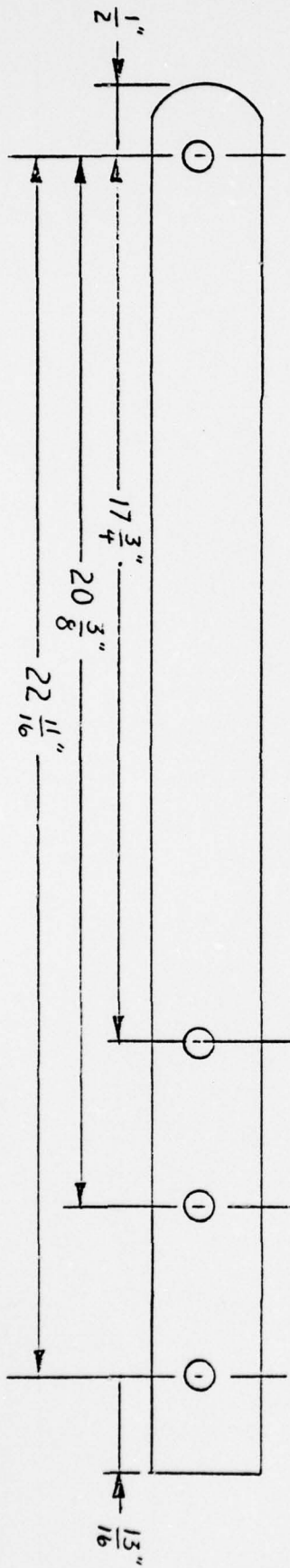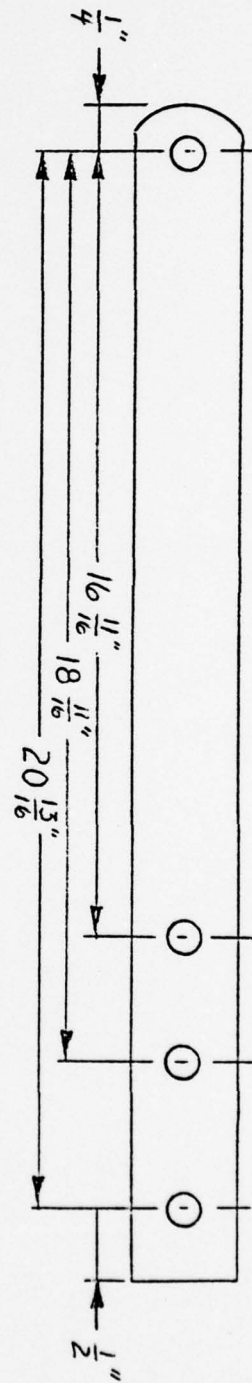
Figure A-4. Schematic of structure braces.

Side attached to
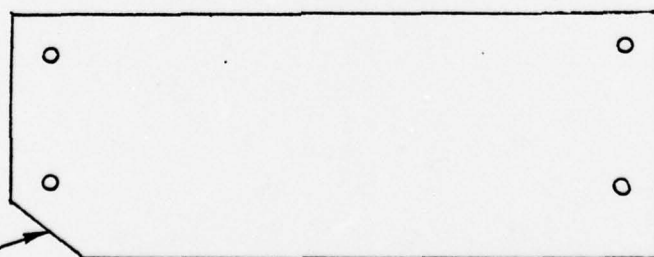angle-changing
block

Side attached
to Bell auxiliary
kit

Side view

Figure A-5.   Schematic of adapter block.

99

Frame attached to structure
tubing by U-bolts

7" bolts (4)

Styrofoam

5½" bolts
(2)
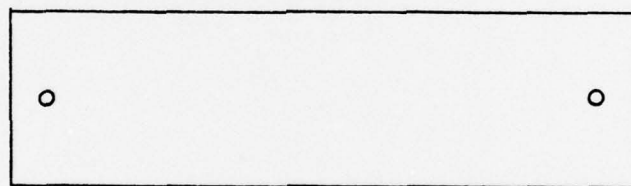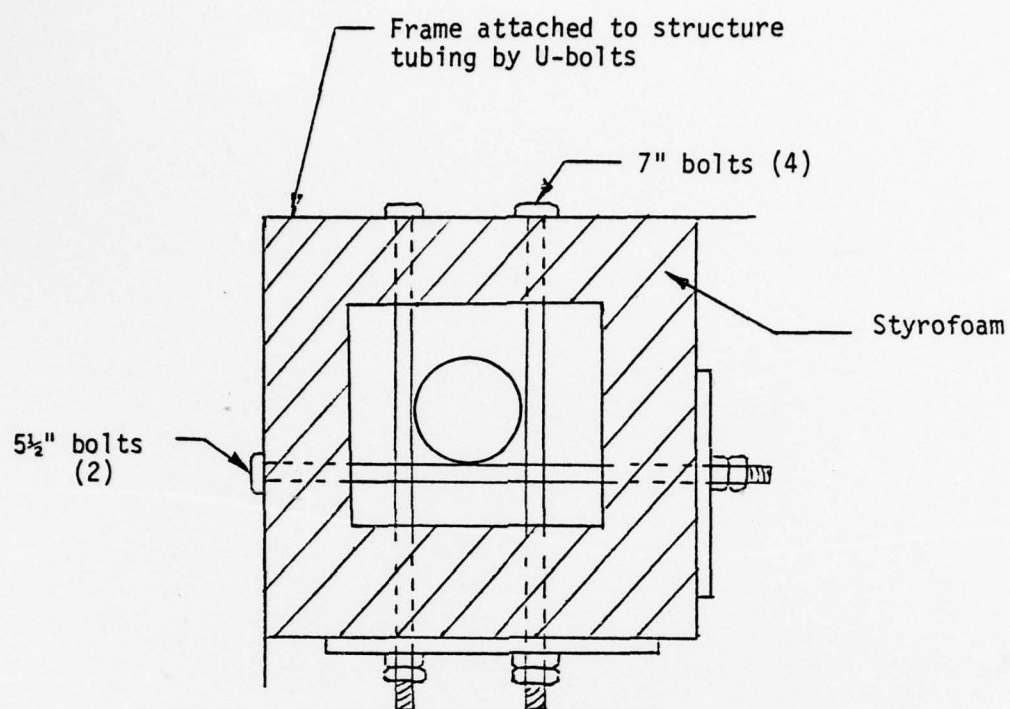
Side plate

Bottom plate

Bevel for clearance
of antenna reflector

Figure A-6. Schematic of TV camera mounting.

APPENDIX B

Antenna Patterns and Beamwidths

100

FREQUENCY (GHz)	GAIN-PRODUCT β Elevation (deg.)	3-dB BEAMWIDTH β Horizontal (deg.)
θ=20° & 40°		
1.5	9.4	8.7
9.0	4.05	3.6
10.0	3.8	3.4
11.0	3.6	3.2
12.0	3.3	2.6
13.0	3.1	2.5
14.0	2.9	2.7
15.0	2.9	2.8
16.0	2.45	2.3
17.0	2.1	2.4
θ=60°		
1.5	10.1	9.1
9.0	4.16	3.8
10.0	3.92	3.6
11.0	3.7	3.3
12.0	3.5	2.7
13.0	3.23	2.6
14.0	3.0	2.8
15.0	2.8	2.9
16.0	2.55	2.4
17.0	2.3	2.5

Table B-1

Frequency (GHz): 8. 0
Polarization: Horizontal
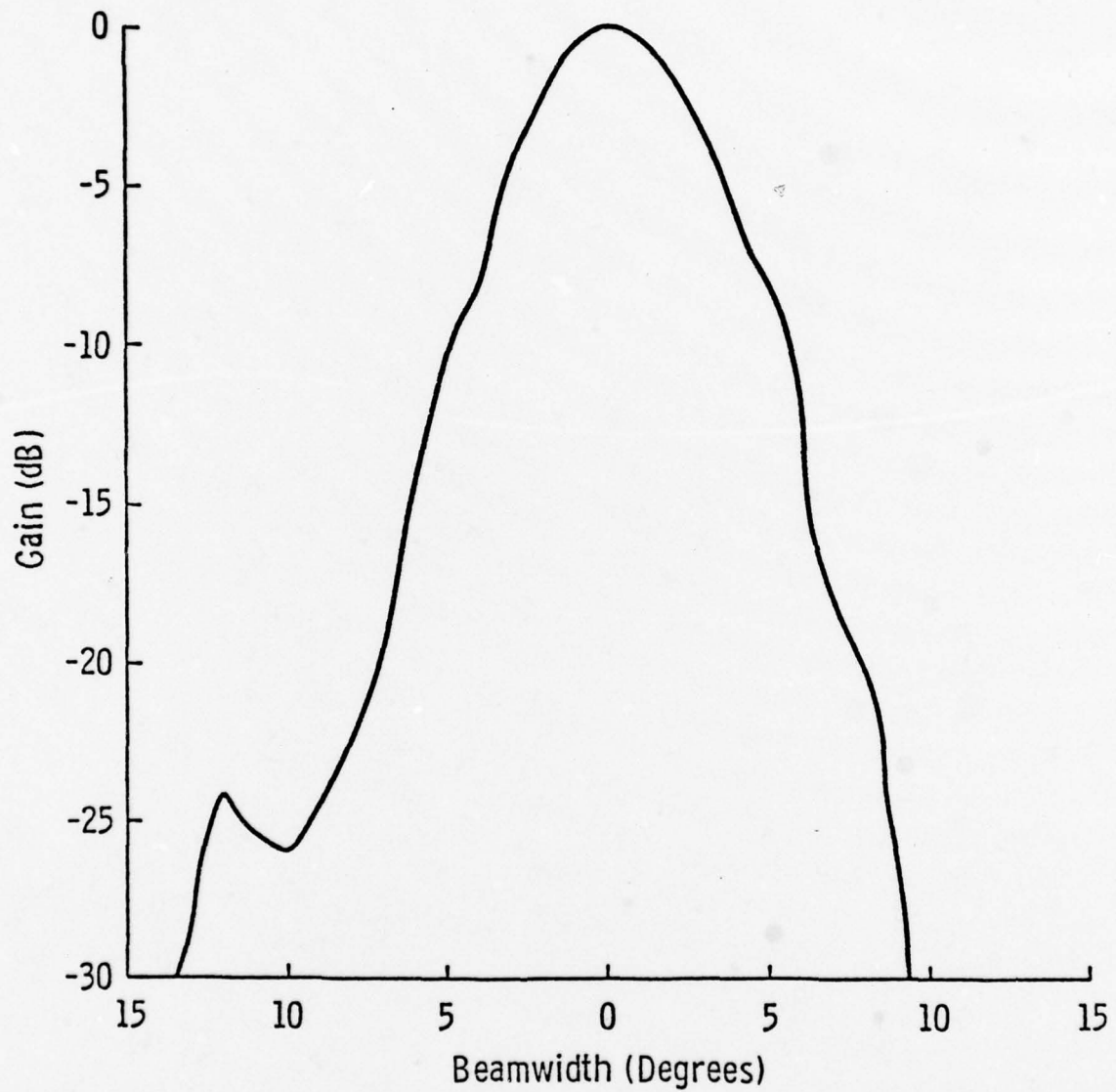Dish (inches): 18. 0
3 dB BW = 5. 1°

Figure B-1.   Transmit antenna pattern at 8.0 GHz in azimuth plane.

Frequency (GHz): 12. 0
Polarization: Horizontal
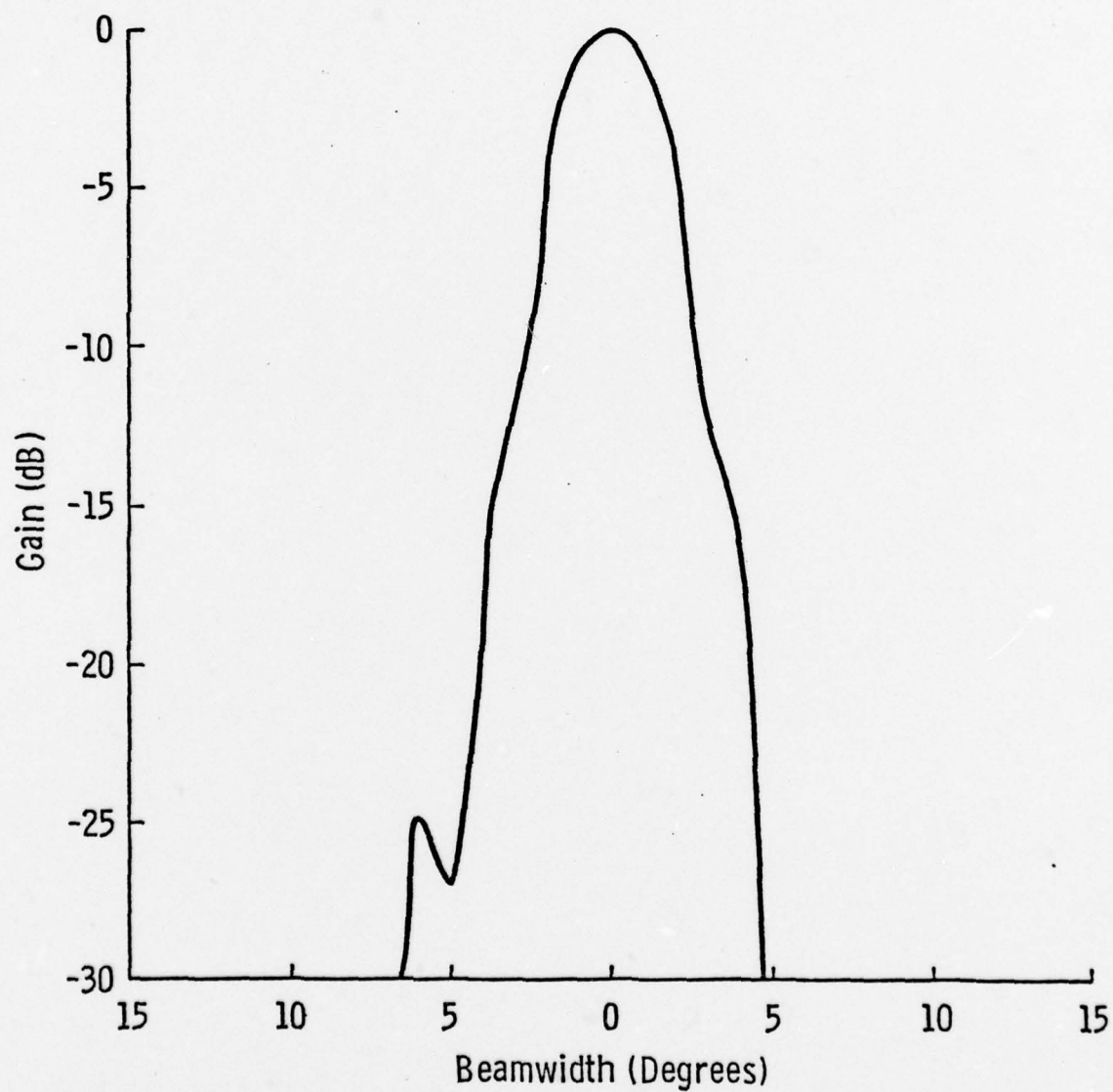Dish (inches): 18. 0
3 dB BW = 3. 6°

Figure B-2.   Transmit antenna pattern at 12.0 GHz in azimuth plane.

Frequency (GHz): 17. 8
Polarization: Horizontal
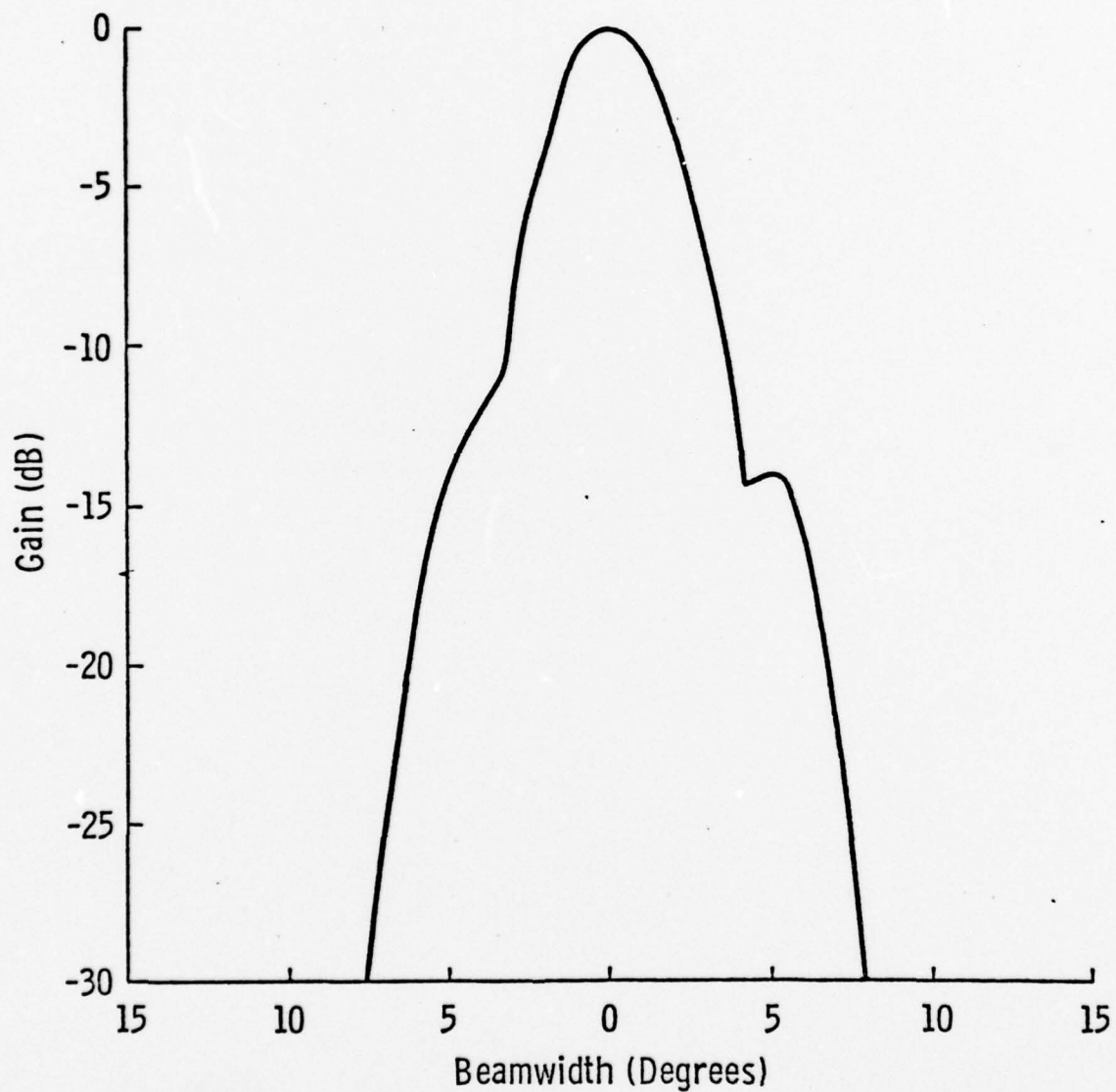Dish (inches): 18. 0
3 dB BW = 5. 1°

Figure B-3.   Transmit antenna pattern at 17.8 GHz in azimuth plane.

Frequency (GHz): 8. 0
Polarization: Vertical
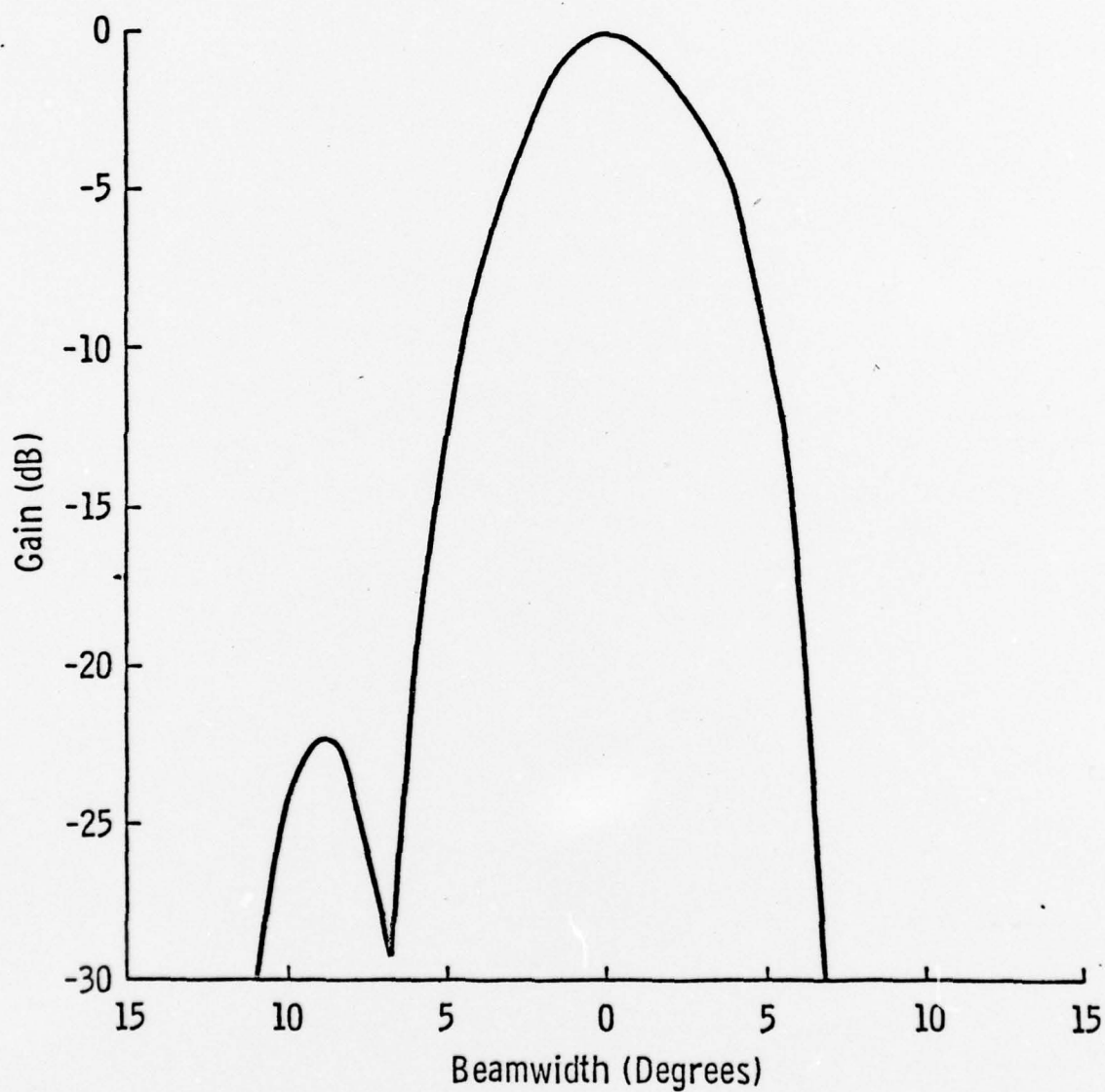Dish (inches): 18. 0
3 dB BW = 5. 3°

Figure B-4.   Transmit antenna pattern at 8.0 GHz in elevation plane.

Frequency (GHz): 8. 0
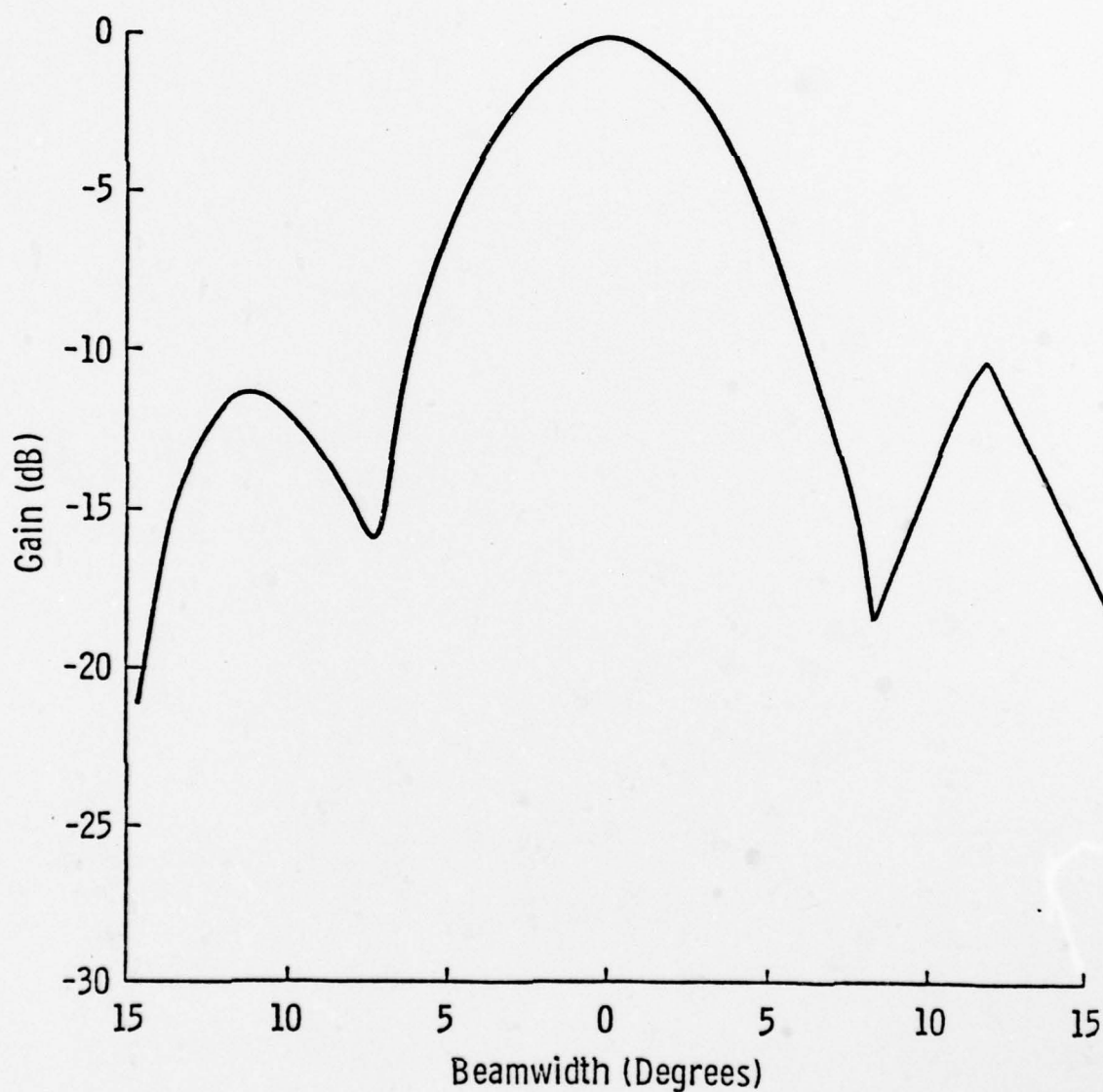Polarization: Horizontal
Dish (inches): 12. 0
3 dB BW = 7. 1°

Figure B-5.   Receive antenna pattern at 8.0 GHz in azimuth plane.

Frequency (GHz): 12. 0
Polarization: Horizontal
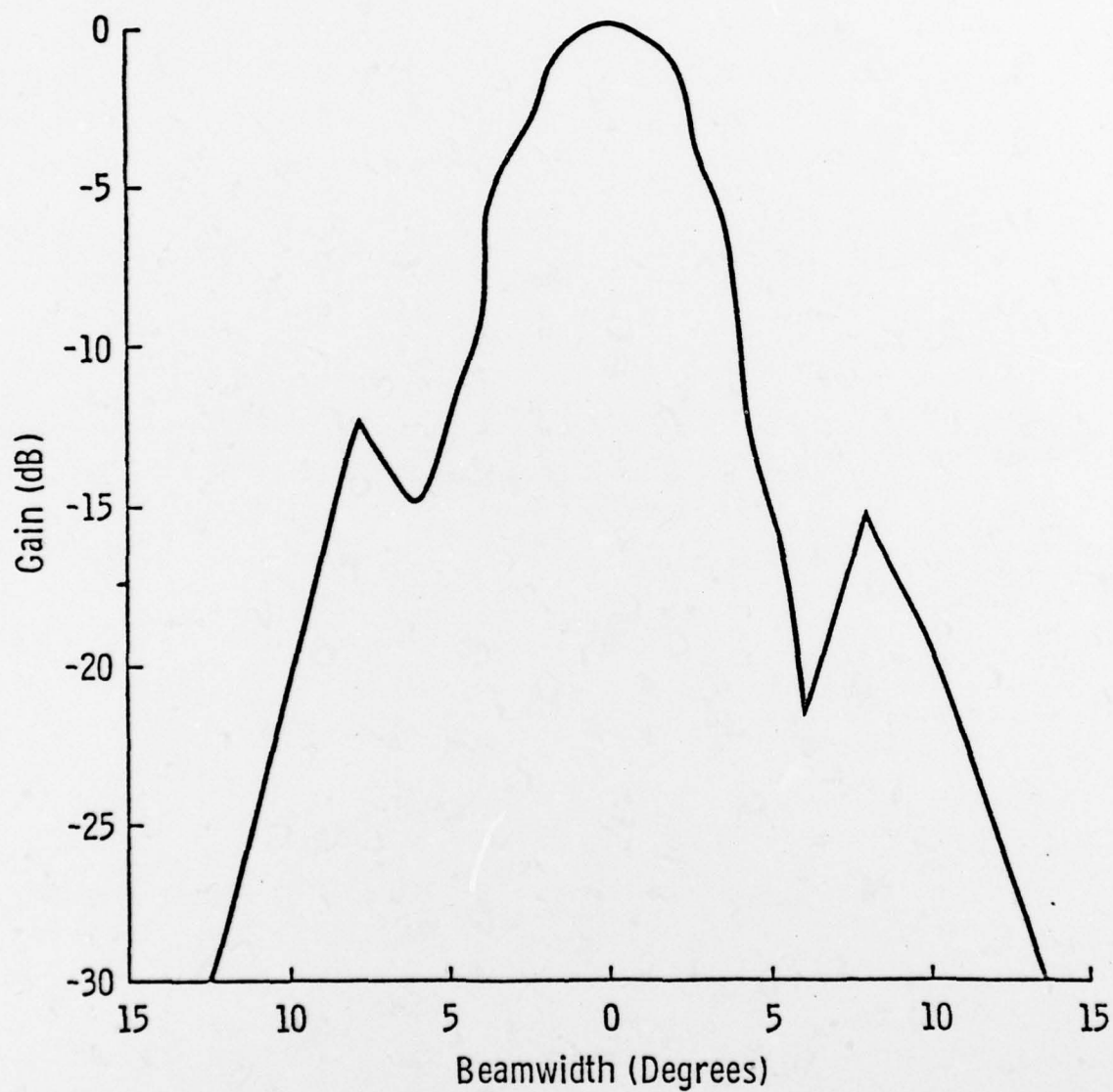Dish (inches): 12. 0
3 dB BW = 4. 8°

Figure B-6. Receive antenna pattern at 12.0 GHz in azimuth plane.

Frequency (GHz): 17.7
Polarization: Horizontal
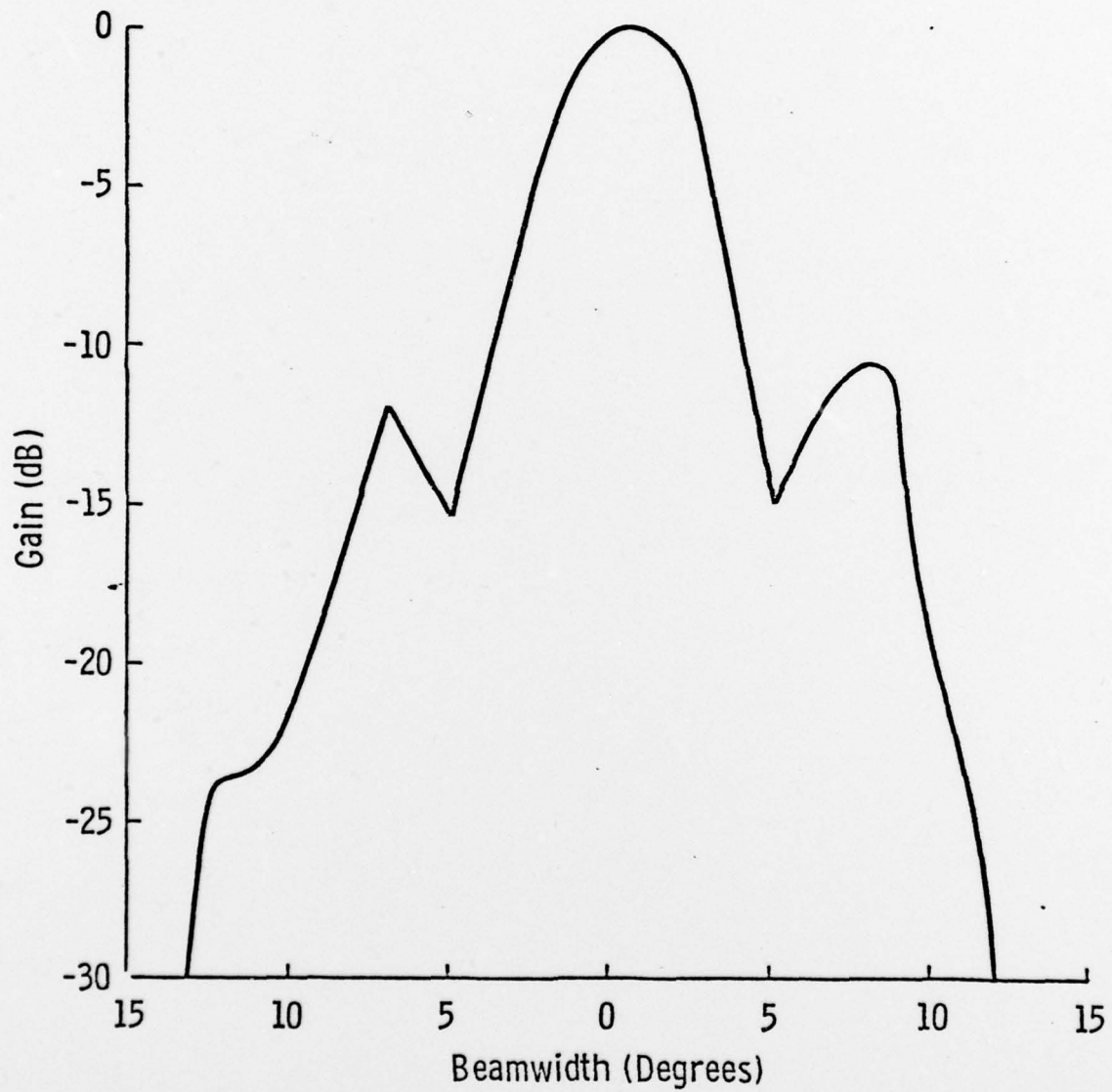Dish (inches): 12.0
3 dB BW = 4.2°

Figure B-7. Receive antenna pattern at 17.7 GHz in azimuth plane.
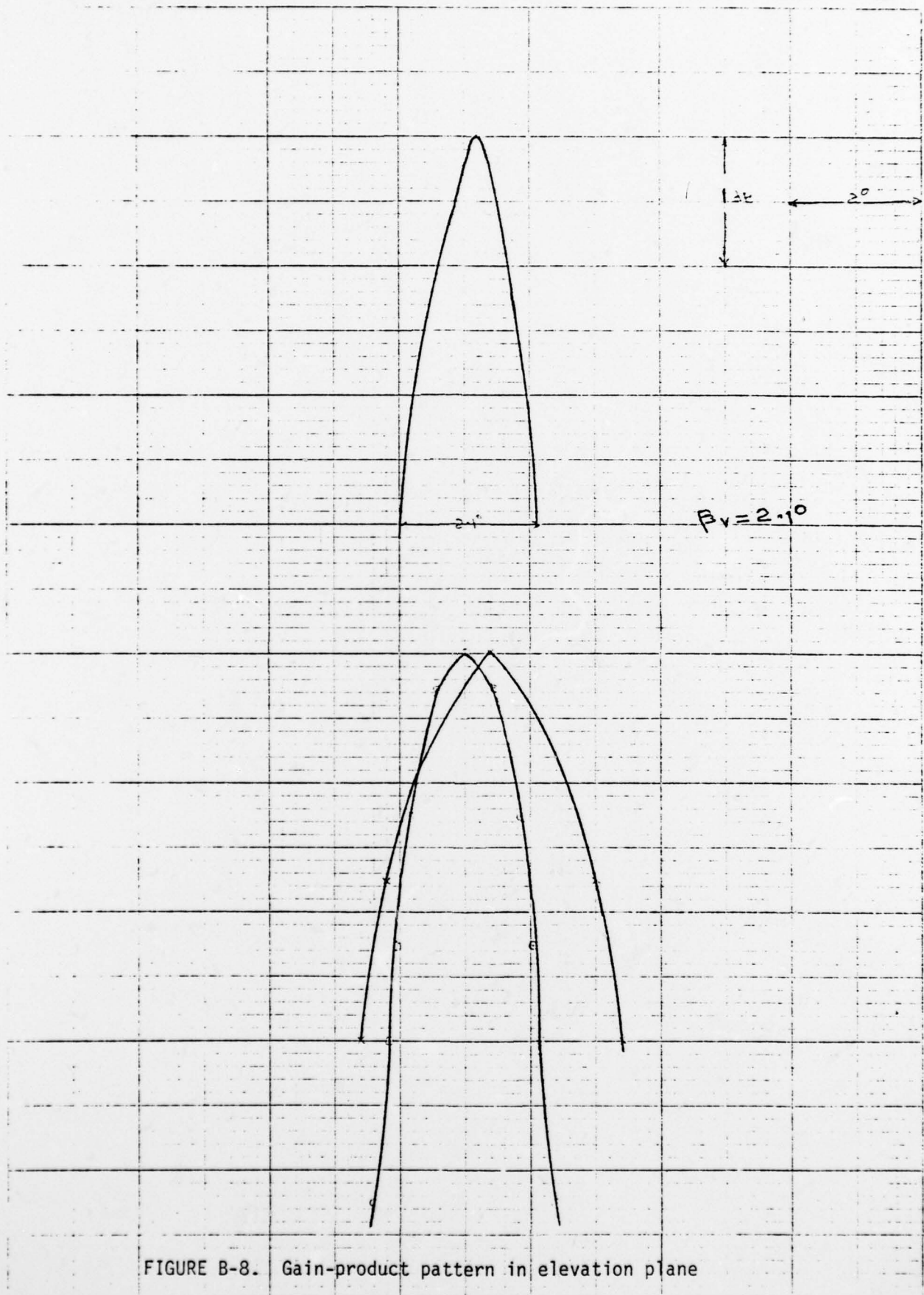
FREQ. 17·8 GHz
VERTICAL POL.

$\beta_V = 2.1°$

FIGURE B-8. Gain-product pattern in elevation plane
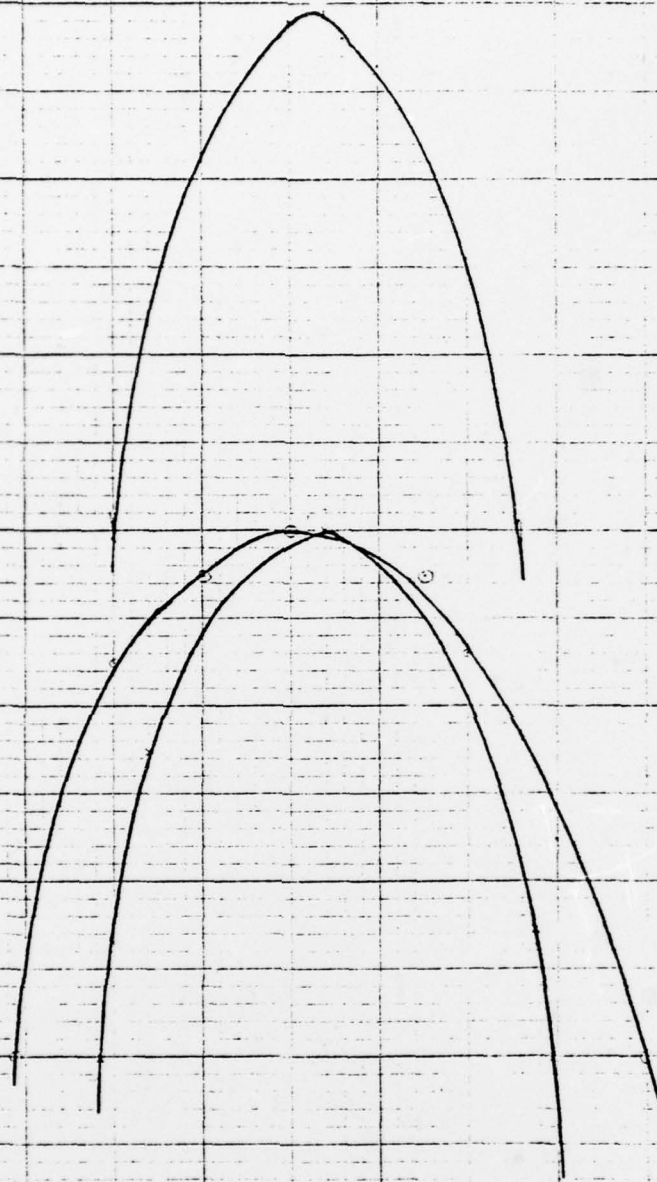
8.0GHz
HORIZONTAL

$\beta_H = 4.56°$

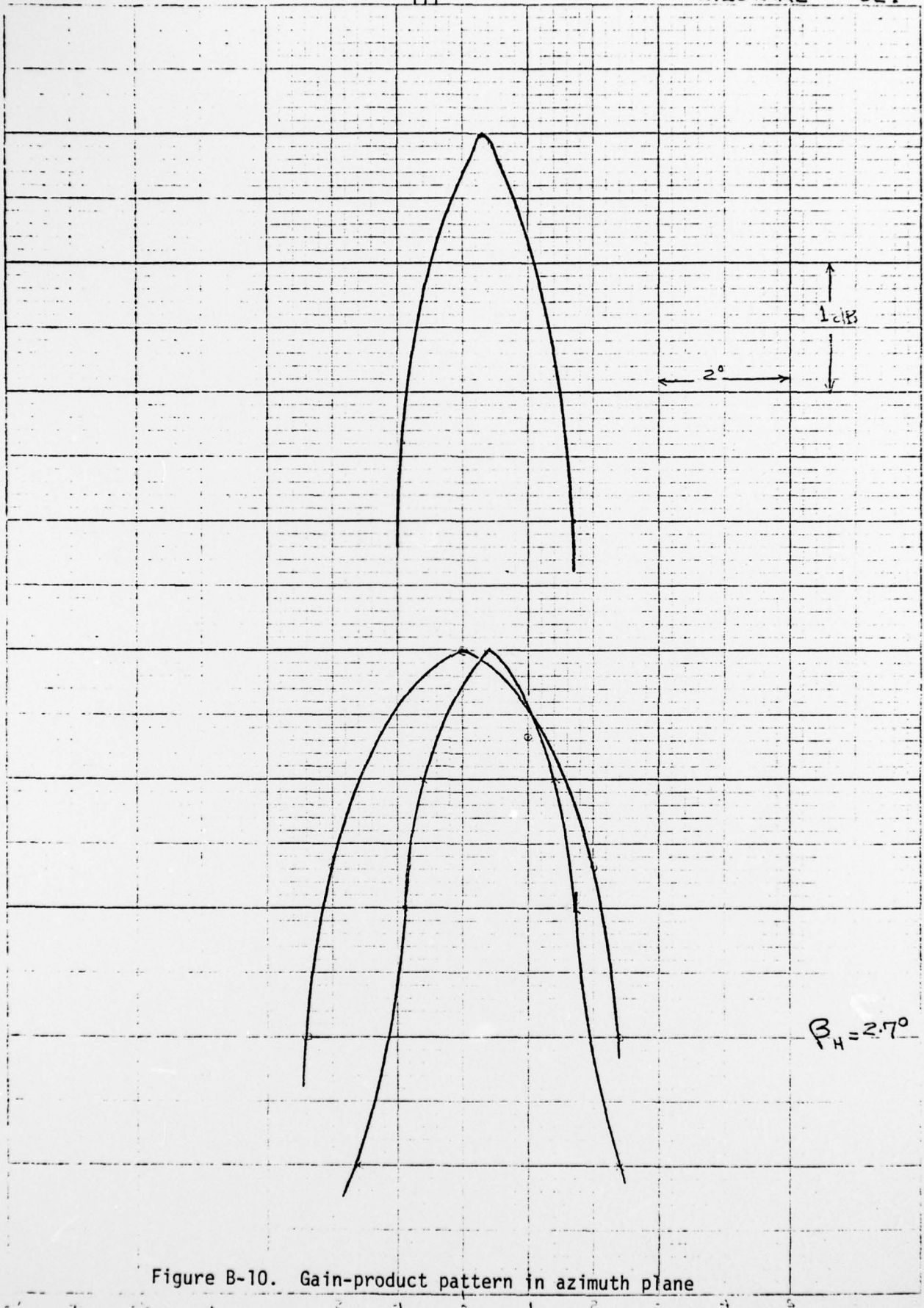Figure B-9. Gain-product pattern in azimuth plane

Figure B-10. Gain-product pattern in azimuth plane

FREQ. 8.0 GHz
VERTICAL POL.
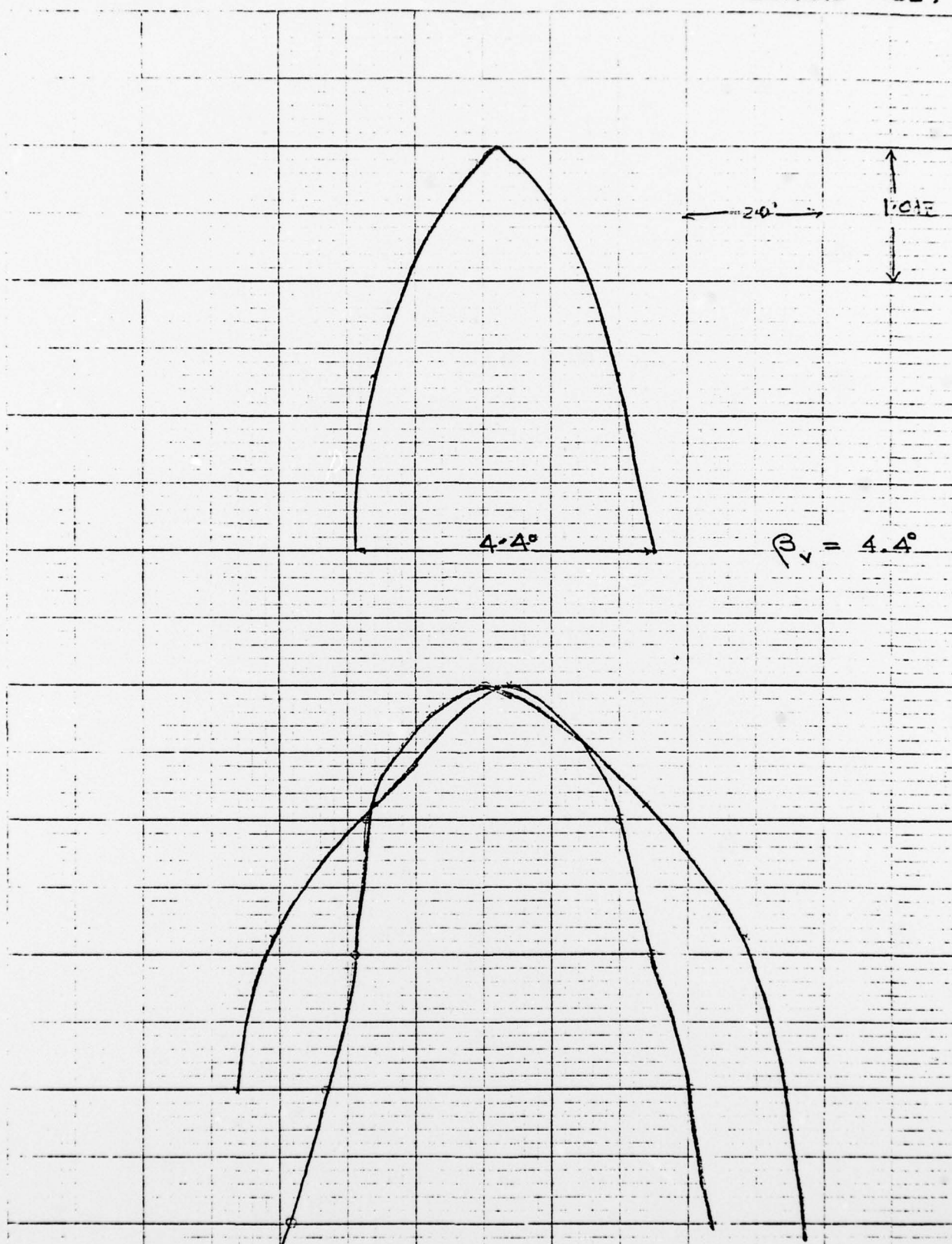

$\beta_v = 4.4°$
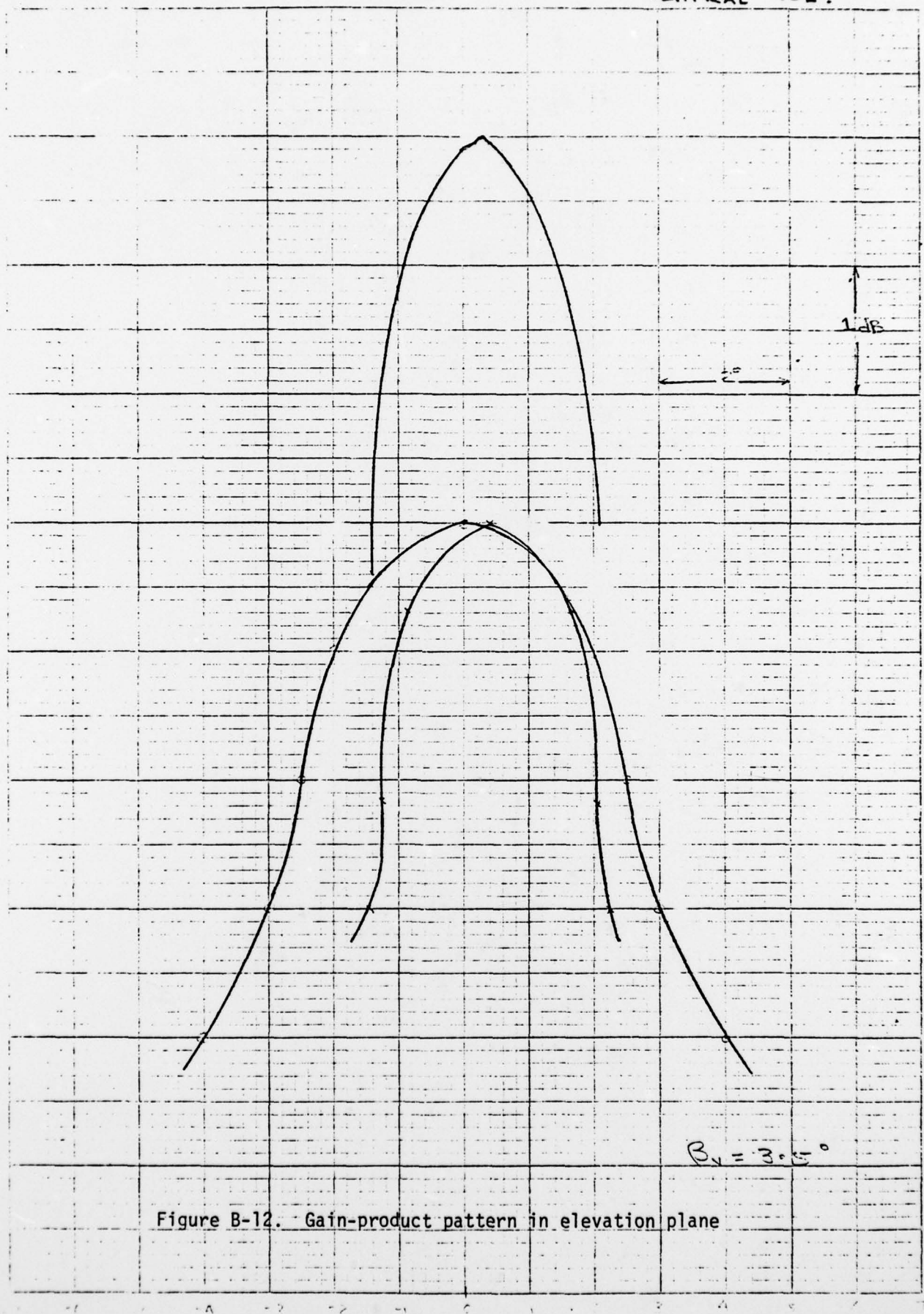
Figure B-11. Gain-product pattern in elevation plane

FREQ. 12.0GHz
VERTICAL POL.

1 dB

$B_v = 3.5°$

Figure B-12. Gain-product pattern in elevation plane

APPENDIX C

Computer Routine for Computing σ^0

```
C THIS COMPUTER ROUTINE COMPUTES THE RADAR BACKSCATTER CROSS-SECTION,SIGMAO,
C FOR THE UNIVERSITY OF KANSAS HELI-BORNE SCATTEROMETER SYSTEM, HELOSCAT.
C DIMENSION STATEMENTS
  DIMENSION SIGMAL(10),BH(10),BV(10),SIGMAX(10,10),BV2(10),PLENS(10)
  DIMENSION PLENS1(10),PLENS2(10),PLENS3(10)
  DIMENSION SIGMA(10,10),PORET(7,10),SRT(10),BH1(10),BV1(10),BH2(10)
  DIMENSION B(10),C(10),D(10),E(10),AILL(10),DLI(10),DLL(10),A1(10)
C 'SRT' IS THE RADAR CROSS-SECTION OF THE STANDARD RADAR TARGET
C (LUNEBERG LENS)AT L-BAND AND THE NINE KU-X FREQUENCIES.
  DATA SRT/-1.0,10.7,11.1,11.4,11.2,11.5,10.6,9.7,9.3,7.3/
C 'DLL' IS THE DELAY LINE READING TAKEN WHILE LOOKING AT
C THE LENS DURING CALIBRATION.
  DATA DLL/16.58,14.41,13.03,10.88,7.44,7.11,8.04,7.90,5.15,1.55/
C 'PLENS' IS THE BACKSCATTER RETURN FROM THE LUNEBERG LENS
C AT THE TEN FREQUENCIES.
  DATA PLENS3/-46.24,-38.75,-39.77,-41.58,-44.55,-42.03,-43.34,
 &-46.50,-53.09,-57.79/
  DATA PLENS1/-37.15,-38.75,-39.77,-41.58,-44.55,-42.03,
 &-43.34,-46.50,-53.09,-57.79/
  DATA PLENS2/-39.85,-38.75,-39.77,-41.58,-44.55,-42.03,
 &-43.34,-46.50,-53.09,-57.79/
C 'BH1' IS THE 3-DB BEAMWIDTH IN THE H-PLANE FOR THE 20
C AND 40 DEGREE ANGLES OF INCIDENCE.
```

```
      DATA BH1/8.7,3.6,3.4,3.2,2.6,2.5,2.7,2.8,2.3,2.4/
C 'BV1' IS THE 3-DB BEAMWIDTH IN THE E-PLANE FOR THE 20
C AND 40 DEGREE ANGLES OF INCIDENCE.
      DATA BV1/9.4,4.05,3.8,3.6,3.3,3.1,2.9,2.7,2.45,2.1/
C 'BH2'AND 'BV2' ARE THE BEAMWIDTHS IN THE H AND E PLANES
C RESPECTIVELY FOR THE 60 DEGREE ANGLE.
      DATA BH2/9.1,3.8,3.6,3.3,2.7,2.6,2.8,2.9,2.4,2.5/
      DATA BV2/10.13,4.16,3.92,3.7,3.5,3.23,3.0,2.8,2.55,2.3/
C OUTPUT HEADING.
      WRITE(16,10000)
      FORMAT(20X,25H RESULTS  OF  SPRING  1978/
     &29X,19HSEA-ICE  EXPERIMENT///)
C READ DATA CARDS.
      READ(15,10,END=5500)K,L,M
      FORMAT(5X,2I3,6X,I2)
C CHECK TO SEE IF CARD READ IS A DATA CARD .GO TO STATEMENT
C 600 IF IT IS,AND IF IT IS NOT THEN ITS A LOOK-ANGLE CARD
C SO GO TO STATEMENT 50000 AND WRITE NO. OF LOOKS AND
C ANGLE OF INCIDENCE AFTER CORRECTING FOR ERRORS DUE TO
C ROLL OF HELICOPTER.
      IF(K.LE.5)GO TO 600
      N=K/10
      GO TO 7000
```

```
C IF SITE NO. 00 THEN ALTITUDE=75FT.

 IF(L.EQ.00)GO TO 1000

C ALTITUDE 100FT CONVERT TO METRES.

 H=100.00/3.281

 GO TO 2000

 .PL 60

 H=22.86

C WRITE THE DATE AND SITE NO.

 WRITE(16,20)K,L

 FORMAT(///10HDATE: MAY I3,5X,9HSITE NO. I3//)

C READ NO. OF LOOKS AND ANGLE.

 READ(15,11)I,J

 FORMAT(5X,I2,10X,I2)

 N=I

 M=J

 IF(M-40)532,534,536

 AM=17.5641

 GO TO 700

 AM=36.2430

 GO TO 700

 AM=56.1186

 WRITE(16,40)N,AM

 FORMAT(/13HNO. OF LOOKS=I3,5X,6HANGLE=F7.4/)
```

```
C READING OF DELAY LINE WHILE FLYING OVER TARGET.

  READ(15,50)(DLI(J),J=1,10)

C THE POWER RETURNED FROM THE TARGET.

  READ(15,50)((PORET(I,J),J=1,10),I=1,N)

  FORMAT(5X,10F7.2)

C RANGE TO TARGET DURING CALIBRATION.

  RANCAL=(131.0/3.281)

C RANGE TO TARGET DURING DATA TAKING WHERE R=H/COS(THETA).

  RANTAR=(H/COS(AM*(3.14159/180)))

  RANG=AM*(3.14159/180)

  DO 100 I=1,N

  DO 100 J=1,10

C CHECK FOR MISSING DATA POINTS.

  IF(PORET(I,J).EQ.99.99)GO TO 110

  IF(M.EQ.60)GO TO 400

  BH(J)=BH1(J)

  BV(J)=BV1(J)

  GO TO 500

  BH(J)=BH2(J)

  BV(J)=BV2(J)

C CALCULATE THE AREA OF THE ILLUMINATED CELL ON THE GROUND.

  B(J)=BV(J)*(3.14159/360)/0.9345

  C(J)=BH(J)*3.14159/(360*0.9345)
```

```
      D(J)=SIN(RANG+B(J))/COS(RANG+B(J))

      E(J)=SIN(RANG-B(J))/COS(RANG-B(J))

      A1(J)=SIN(C(J))/COS(C(J))

      AILL(J)=(3.14159/2.)*H*(D(J)-E(J))*RANTAR*(A1(J))

      DO 1004 K=1,10

      IF(AM-36.2430)1001,1002,1003

      PLENS(K)=PLENS1(K)

      GO TO 1004

      PLENS(K)=PLENS2(K)

      GO TO 1004

      PLENS(K)=PLENS3(K)

      CONTINUE

C CALCULATE THE RADAR CROSS-SECTION SIGMAO.

      IF(J.GT.1)GO TO 1006

      SIGMA(I,J)=PORET(I,J)-DLI(J)-PLENS(J)+DLL(J)+SRT(J)

     &-10.*ALOG10(AILL(J))

      GO TO 1008

      SIGMA(I,J)=PORET(I,J)-DLI(J)-PLENS(J)+DLL(J)+SRT(J)

     &-10.*ALOG10(AILL(J))+40.*ALOG10(RANTAR)-40.*ALOG10(RANCAL)

      GO TO 100

C DENOTING SIGMAO FOR THE MISSING POINTS.

      SIGMA(I,J)=99.0

C COMPILING L-BAND SIGMAO SEPARATELY.
```

```
      SIGMAL(I)=SIGMA(I,1)

      CONTINUE

      DO 130 I=1,N

      DO 130 J=1,9

      J1=J+1

C COMPILING KU-X-BAND SIGMAO SEPRATELY.

      SIGMAX(I,J)=SIGMA(I,J1)

      CONTINUE

C WRITE OUT SIGMAO IN DESIRABLE FORMAT.

      WRITE(16,200)

      FORMAT(10X,14HL-BAND SIGMAOS/)

      WRITE(16,250)(SIGMAL(I),I=1,N)

      FORMAT(5X,F7.2)

      WRITE(16,300)

      FORMAT(/10X,17HKU-X BAND SIGMAOS/)

      WRITE(16,350)((SIGMAX(I,J),J=1,9),I=1,N)

      FORMAT(5X,9F7.2)

      GO TO 5000

      STOP

      END
```